



# **Group III-V Quantum Dot Solar Cells**

**Shun Chan**

A thesis submitted to UCL for the degree of  
*Doctor of Philosophy (PhD)*

Department of Electronic & Electrical Engineering  
University College London

**Jan 2022**



## **Statement of originality**

I, Shun Chan, confirm that the work presented in this thesis is my own. Where information has been derived from other sources, I confirm that this has been indicated in the thesis.

**Signed:**

---

**Date:**

---



*To my wife, Na*



## Abstract

Since the global warming, clean and renewable energy resources are under intense demand. In particular, the photovoltaic research field has attracted increasing amount of attention whether from business investment or public funding. “Intermediate band solar cell (IBSC)” is a novel concept introduced by Luque and Marti in 1997. It has the potential to overcome the conventional solar cell efficiency limit (33.1%) by two-fold.

This thesis aims to use quantum dot solar cells (QDSC) to realise the IBSC and, hence, achieve the 63.2% ultra-high power conversion efficiency. The approach is to epitaxially grow the QDSC using the most advanced epitaxial growth technique—molecular beam epitaxy (MBE). The nature of quantum dots (QDs) exhibits 3-dimensional (3D) carrier confinement and have discrete energy levels, a perfect candidate to implement the intermediate energy levels required for IBSCs. In this thesis, the practical implementations, physical limitations and technical difficulties are addressed and reviewed in detail.

The possibility of background doping effects on the QDs is investigated in the first project by growing the dots within the n-type base region. Two samples with QDs embedded into the base region are compared to a reference sample with QDs in the intrinsic region. The current density-voltage (*JV*) characterisation results have shown a 23% marginal increase in voltage and a 29% marginal increase in the overall conversion efficiency.

The origin of current loss in Si-doped QDs is studied in the second project and a method was proposed to recover the lost currents. Three samples with additional 100 nm intrinsic thickness were grown to compare with the regular Si doped QDSC. The *JV* characterisation results have shown 14% current enhancement without any voltage compensation.

The aim of the third project is to achieve the optimal IBSC bandgap configuration by deploying AlGaAs as a host material. Six AlGaAs samples were grown at different temperatures in order to investigate the optimum growth temperature. The results have shown that the minimum temperature required for high material quality is 600°C, and higher temperatures lead to higher Al compositions.

## Impact statement

Global energy consumption has been increasing over the past century but traditional energy sources such as coal and fossil fuel are running out of supply. World's leading nations are urged to seek for alternative energy sources to fuel their economies. Solar energy has emerged as a renewable, clean and environmentally-friendly source of energy. Thus, devices such as solar cells or solar panels that can harness this type of energy are under intense study.

The state-of-the-art intermediate band solar cell (IBSC) and multi-junction solar cell (MJSC) are the third-generation solar cells that have the potential to overcome the Shockley-Queisser limit of 33.1%. The first-generation pn-junction solar cells and second-generation thin-film solar cells are near market saturation, thus, realising the IBSC and the MJSC would open up a whole new market for investment opportunities. The MJSC with three junctions has an inferior theoretical maximum efficiency of 45% compared to the 63.2% maximum efficiency of IBSC, which renders the IBSC a more promising candidate to dominate the new market.

Researching in the QDSCs, which are used to implement the IBSCs, also has an important strategic benefit to the military and space sector. Due to the small physical size of QDs, QDSCs have high efficiency, low volume and light weight; hence, are portable to carry out military tasks. Furthermore, due to 3D quantum confinement and bandgap tunability of QDs, QDSCs also exhibit temperature independence and adjustable absorption band which are imperative for space application.

The findings in this thesis present many solutions to the major problems during the implementation of the IBSC, and pave a path to realising the ultra-high efficiency predicted by the IBSC model.

## Acknowledgements

First and foremost, I would like to thank my supervisor, Professor Huiyun Liu, for his guidance and support during my PhD study. Second, I would like to thank my second supervisors, Dr Jiang Wu and Dr Siming Chen, for helping me in understanding the physics and fabrication of solar cells. Third, I would like to express my deepest gratitude to Dr Dongyoung Kim who has also been a great mentor to me.

I would like to acknowledge all current and former members of the Molecular Beam Epitaxy Research Group: Dr Arthur Onno, Dr Yunyan Zhang, Dr Pameple Jurcazk, Dr Hao Xu, Dr Mingchu Tang, Dr Jae-Seong Park, Dr Xuezhe Yu, Dr Mengya Liao, Dr Daqian Guo, Mr Zizhuo Liu, Ms Ying Lu, Ms Xiao Li, Mr Kai Shen and Mr Haotian Zeng. It has been a pleasure working and learning with you all.

Finally, I would like to thank my family and friends for their continued support throughout this research project. I thank my grandparents for their patience and trust in me. I thank my parents for their wealth in providing the financial support needed to complete my education. I thank my friends for their pleasant company and will remember all the good times together. I thank my wife, Na Zhao, for caring and believing in me. Without her help and understanding, my research life would not be so bright and cheerful.

# Table of Contents

Abstract .....	7
Impact statement .....	8
Acknowledgements .....	9
List of Publications and conference presentations .....	17
Chapter 1 Quantum dot solar cells .....	19
1.1 Quantum dot intermediate band solar cell.....	20
1.1.1 Intermediate band solar cell .....	20
1.1.2 Quantum dot solar cell .....	22
1.1.3 Quantum dot intermediate band solar cell .....	23
1.1.4 Review of the challenges and progress.....	24
1.2 Thesis structure .....	33
1.3 References .....	34
Chapter 2 Introduction to solar energy and solar cells .....	42
2.1 Solar resource.....	43
2.2 Semiconductors for solar cells .....	45
2.2.1 Optical properties.....	45
2.2.2 Doping and impurities.....	50
2.2.3 Carrier transport .....	52
2.2.4 PN junction .....	55
2.3 Solar cell operation.....	59
2.3.1 PN junction solar cell operation.....	59
2.3.2 Ideal solar cell conditions .....	60
2.3.3 Practical limitations .....	61
2.3.4 Shockley Queisser limit .....	62
2.4 References .....	63
Chapter 3 Experimental methods .....	64
3.1 Sample growth.....	65
3.1.1 Molecular beam epitaxial growth .....	65
3.1.2 MBE growth modes .....	67
3.1.3 Self-assembled quantum dots .....	68

3.2	Device fabrication .....	69
3.2.1	General process .....	70
3.2.2	Sample preparation .....	74
3.2.3	Oxide removal.....	74
3.2.4	Photolithography.....	74
3.2.5	Metal contact deposition.....	77
3.2.6	Lift-off.....	78
3.2.7	Wet etching.....	79
3.2.8	Thermal annealing .....	79
3.3	Solar cell characterisation .....	80
3.3.1	Atomic force microscopy (AFM) .....	80
3.3.2	Scanning electron microscopy (SEM) .....	81
3.3.3	Photoluminescence (PL).....	82
3.3.4	External quantum efficiency (EQE).....	83
3.3.5	Current density-voltage ( <i>J-V</i> ) characterisation .....	85
3.4	References .....	90
Chapter 4	InAs/GaAs quantum dot solar cell with QDs in base region .....	92
4.1	Introduction .....	93
4.2	Experimental work.....	94
4.2.1	Growth .....	94
4.2.2	Fabrication .....	96
4.2.3	Characterisation .....	96
4.3	Results and Discussion.....	97
4.3.1	AFM.....	97
4.3.2	TEM .....	98
4.3.3	PL.....	99
4.3.4	EQE.....	101
4.3.5	<i>J-V</i> .....	103
4.4	Discussion .....	104
4.5	Conclusion.....	107
4.6	References .....	108

Chapter 5	Investigation into current loss in InAs/GaAs quantum dot solar cells with Si-doped QDs.....	111
5.1	Introduction .....	112
5.2	Experimental work.....	114
5.2.1	Growth .....	114
5.2.2	Fabrication .....	117
5.2.3	Characterisation .....	117
5.3	Results and Discussion.....	118
5.3.1	SEM .....	118
5.3.2	<i>J-V</i> .....	119
5.3.3	PL.....	121
5.3.4	EQE.....	123
5.3.5	<i>C-V</i> .....	125
5.4	Discussions.....	127
5.5	Conclusion.....	129
5.6	References .....	130
Chapter 6	1.7 eV Al <sub>0.22</sub> Ga <sub>0.78</sub> As solar cell on GaAs substrate.....	132
6.1	Introduction .....	133
6.2	Experimental work.....	135
6.2.1	Growth .....	135
6.2.2	Fabrication .....	136
6.2.3	Characterisation .....	137
6.3	Results and discussion.....	138
6.3.1	PL mapping.....	138
6.3.2	EQE.....	141
6.3.3	<i>J-V</i> .....	142
6.4	Conclusion.....	144
6.5	References .....	146
Chapter 7	Conclusion and future work.....	149
7.1	Conclusion.....	150
7.2	Ongoing work.....	152

7.3	Future work .....	156
7.4	References .....	159
	Appendix.....	161
	UCL 305 Temperature-dependent photoluminescence .....	161
	UCL 305 Power-dependent photoluminescence.....	162
	UCL249 Temperature-dependent photoluminescence .....	163
	UCL249 Power-dependent photoluminescence.....	164

## Table of Figures

Figure 1.1	Concept of the intermediate band solar cell absorbing three ranges of photon energy.....	20
Figure 1.2	Schematics of DOS versus bulk, quantum well, quantum wire and quantum dot .....	22
Figure 1.3	Structure of a QD-IBSC prototype with the corresponding band diagram .....	23
Figure 1.4	Group III-V material lattice constant vs gap energy and wavelength.....	26
Figure 1.5	Band configuration of InAs QD/GaAs QDSC including the effect of WL.....	29
Figure 1.6	Band configuration of InAs QD/GaAs QDSC with AlGaAs barrier layer .....	30
Figure 1.7	Band configuration of InAs QD/GaAs QDSC with Si-doped QDs .....	31
Figure 1.8	Diagram of type-I and type-II bandgap.....	32
Figure 2.1	Schematic of (a) air mass and (b) ASTM Reference Spectra at AM1.5G, AM1.5D and AM0 .....	44
Figure 2.2	Simple schematic of a bandgap including CB and VB .....	45
Figure 2.3	Direct and indirect bandgaps depicted using Ge, GaAs and Si.....	46
Figure 2.4	ASTM Spectra with GaAs absorption range .....	47
Figure 2.6	Absorption coefficients of semiconductor materials with direct and indirect bandgaps [2].....	48
Figure 2.5	Schematic of photon absorption, no absorption and absorption with extra thermal energy .....	48
Figure 2.7	Three types of recombinations: radiative, SRH and Auger recombination.....	50

Figure 2.8 Effect of p- and n-type doping on the $E_F$ .....	51
Figure 2.9 Schematic of a PN junction illustrating carrier diffusion and depletion region .....	55
Figure 2.10 PN junction at equilibrium with balanced drift and diffusion.....	56
Figure 2.11 PN junction under (a) forward bias mode and (b) reverse bias mode.....	57
Figure 2.12 Schematic of a PN junction solar cell including all operating mechanisms:	59
Figure 3.1 Schematic diagram of an MBE growth chamber .....	65
Figure 3.2 Three MBE growth modes: (a) VW mode, (b) FM mode and (c) SK mode...	67
Figure 3.3 TEM image of InAs QDs grown under SK mode .....	68
Figure 3.4 Photos of fabricated QDSCs with top-bottom contact on the left and top-top contact on the right.....	69
Figure 3.5 Cross-sectional diagrams of QDSC structure before and after top-bottom contact with shadow-masks .....	70
Figure 3.6 Cross-sectional diagrams of QDSC structure before and after top-bottom contact with photo-masks .....	71
Figure 3.7 Cross-sectional diagrams of QDSC structure before and after top-top contact with photo-masks .....	73
Figure 3.8 Sample wafer cleaved into quarter-wafers .....	74
Figure 3.9 Spin-coated sample with S1818 and LOR 10B photoresists.....	75
Figure 3.10 Sample under UV exposure.....	76
Figure 3.11 Developed sample .....	77
Figure 3.12 Metallised sample.....	78
Figure 3.13 Sample with desired contact pattern.....	78
Figure 3.14 Wet-etched sample .....	79
Figure 3.15 AFM operation mechanism.....	80
Figure 3.16 (a) 2D and (b) 3D AFM image of QDs .....	81
Figure 3.17 SEM image of QDSC .....	82
Figure 3.18 PL graph of QDSC .....	83
Figure 3.19 EQE spectrum of QDSC.....	84

Figure 3.20 <i>J-V</i> curve of QDSC.....	85
Figure 3.21 detailed <i>J-V</i> curve .....	87
Figure 3.22 NREL solar cell efficiencies Apr 2020 .....	89
Figure 4.1 QDSC sample structures with QDs in (a) intrinsic region (b) shallow base region (c) deep base region.....	95
Figure 4.2 AFM image of the uncapped QDSC .....	97
Figure 4.3 Cross sectional TEM images of (a) shallow and (b) deep base QDSCs .....	98
Figure 4.4 PL graphs of QDSCs at (a) 10 K and (b) 300 K.....	99
Figure 4.5 EQE spectra of QDSC with log-scaled sub-bandgap inset .....	101
Figure 4.6 <i>J-V</i> characteristic of QDSCs.....	103
Figure 4.7 A simplified schematic diagram of the energy band of (a) Ref QD, (b) shallow QD and (c) deep QD under operation: including the electric field, QD region (red dotted box), electron movements and gold contact .....	105
Figure 5.1 Schematic of diode—capacitor equivalency .....	113
Figure 5.2 Schematics of the p-i-n solar cells.....	116
Figure 5.3 Cross-sectional SEM images of (a) Si-doped QDSC and (b) Si-doped QDSC + 100 nm Emitter .....	118
Figure 5.4 <i>J-V</i> characteristics of GaAs SC and QDSCs .....	119
Figure 5.5 PL spectra of QDSCs at (a) 10 K and (b) 300 K.....	122
Figure 5.6 EQE spectra of GaAs SC and QDSCs.....	123
Figure 5.7 Depletion width of the GaAs SC and QDSCs .....	125
Figure 5.8 A Simplified schematic diagram of the energy band of (a) Si-doped, (b) Thick spacer, (c) Thick emitter and (d) Thick base QDSCs .....	127
Figure 6.1 SC structure of $\text{Al}_{0.22}\text{Ga}_{0.78}\text{As}$ (with no QDs) and the corresponding energy band diagram.....	135
Figure 6.2 PL mapping of AlGaAs samples .....	139
Figure 6.3 EQE spectrum of AlGaAs SCs.....	141
Figure 6.4 <i>JV</i> graphs of AlGaAs SCs .....	142
Figure 7.1 Schematics of the GaAsSb SCs.....	153

Figure 7.2 JV graphs of GaAsSb SCs before and after irradiation: (a)-(c) with no QDs,  
(d)-(f) with QDs and (g)-(i) QDs with GaAs interlayers ..... 154

Figure 7.3 QDSC structures with (a)&(b) alternating QD layers and (c) alternating QDs  
..... 157

## List of Publications and conference presentations

### Journal publications:

- [1] S. Chan, D. Kim, A. Sanchez, Y. Zhang, M. Tang, J. Wu, and H. Liu, "InAs/GaAs quantum dot solar cells with quantum dots in the base region," *IET Optoelectron.*, vol. 13, no. 5, pp. 215–217, Oct. 2019.

Impact factor: 1.636 Cited by: 2

- [2] S. Chan, D. Kim, M. Tang, X. Li, and H. Liu, "Investigation into the current loss in InAs/GaAs quantum dot solar cells with Si-doped quantum dots," *J. Phys. D. Appl. Phys.*, vol. 52, no. 50, pp. 505108, 2019.

Impact factor: 3.207 Cited by: 0

- [3] D. Kim, S. Chan, M. Tang, J. Wu, and H. Liu, "The influence of direct, delta, and modulation QD Si doping on InAs/GaAs quantum dot solar cells," in *2018 IEEE 7th World Conference on Photovoltaic Energy Conversion, WCPEC 2018 - A Joint Conference of 45th IEEE PVSC, 28th PVSEC and 34th EU PVSEC*, 2018, Waikoloa HI USA, pp. 2759–2762.

Impact factor: 0.64 Cited by: 1

- [4] H. Afshari, B. K. Durant, T. Thrasher, L. Abshire, V. R. Whiteside, S. Chan, D. Kim, S. Hatch, M. Tang, J. S. McNatt, H. Liu, M. R. McCartney, D. J. Smith, and I. R. Sellers., "Radiation tolerance of GaAs<sub>1-x</sub>Sb<sub>x</sub> solar cells," *Sol. Energy Mater. Sol. Cells*, vol. 233, p. 111352, 2021

Impact factor: 7.267 Cited by: 0

### Conference presentations:

- [1] S. Chan, D. Kim, J. Wu, H. Liu, "InAs/GaAs quantum dot solar cells with quantum dots in the base region," *Semiconductor and Integrated Optoelectronics*, Cardiff, UK, 2018.

- [2] S.Chan, D. Kim, J.Wu, H. Liu, “State-filling effects in Si-doped quantum dot solar cell with AlAs cap layers”, *UK Semiconductors*, Sheffield, UK, 2017

## Chapter 1 Quantum dot solar cells

*This chapter first introduces the concept of intermediate band solar cell, followed by the realisation and implementation of the concept using the quantum dot solar cells. The progress and challenges are reviewed and discussed at the end of the chapter.*

## 1.1 Quantum dot intermediate band solar cell

Intermediate band solar cell (IBSC) is a concept proposed by Luque and Marti to challenge the 33.1% maximum efficiency calculated by Shockley and Queisser. Quantum dot solar cell (QDSC) is the main focus of this research, and it is a conventional solar cell incorporated with nano-structured QD materials. QDSC can be used to realise the IBSC concept, and QDSC devices that are used to implement the IBSC are named QD-IBSC. Furthermore, QDSC also have a great potential for space SCs. This thesis studies in both fields but has devoted more effort to implementing the QD-IBSC.

### 1.1.1 Intermediate band solar cell

In 1997, Luque and Marti proposed a novel SC structure aiming to exceed the Shockley Queisser Limit (SQL) [1]. The approach is to utilise the sub-bandgap photons by introducing an intermediate band (IB) between the conduction band (CB) and the valence band (VB), hence the name intermediate band solar cell (IBSC).

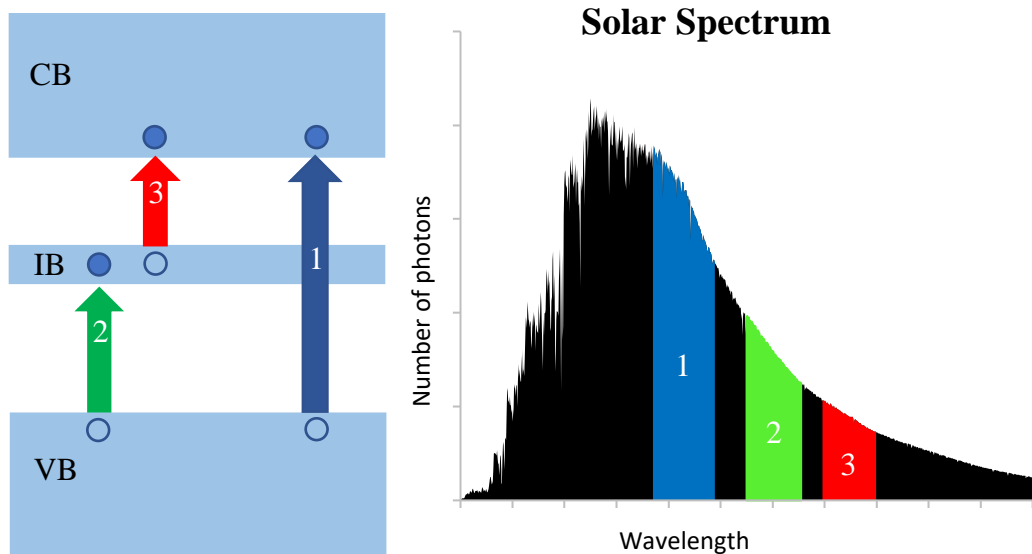


Figure 1.1 Concept of the intermediate band solar cell absorbing three ranges of photon energy

Figure 1.1 illustrates an extra IB in between the CB and VB; it can absorb the high energy photons (1) while absorbing the lower energy photons (2) and (3). The energy of the

absorbed photons corresponds to different regions of the solar spectrum, and thus sub-bandgap absorption is achieved by the IB. Intuitively, the IB can be regarded as a stepping-stone: photon with energy (2) slightly less than the bandgap (1) could use this platform to gain an extra photon (3) and leap into CB [2]. As more photons are absorbed, more carriers are generated to boost the current output. The potential efficiency of IBSC outperforms the SQL by two-fold, reaching 63.1%.

In the proposal, 7 ideal conditions (IC) have been established to manufacture an IBSC. The first and second ICs forbid non-radiative recombination between any two of the three bands and grant the carrier infinite mobilities. IC3 prohibits carrier extraction from the IB. IC4 and IC5 demand for full absorption through device thickness and front area illumination. IC6 ensures high efficiency by assuming only one of the three absorption lengths is important for every range of energies. IC 7 requires isotropic cell illumination i.e. 63.2% maximum efficiency is achieved under concentrated sunlight (46000 suns). In the SQL model, maximum efficiency would be 40.7% under the same concentrated illumination [3].

To implement the ICs, a IBSC requires a material system with a bandgap configuration of 1.95 eV between CB—VB , 1.24 eV between VB—IB and 0.71 eV between IB—CB (VB—IB and IB—CB transition can be interchanged) [4]. The IB can be obtained by means of lone pair bands, impurities or low dimensionality superlattices [1]. In addition, the IB needs to be partially-filled with electrons so that the electron-filled states promote IB—CB transition without the precondition of VB—IB transition, yet, the IB should reserve enough valence states to assure VB—IB transition. Doping techniques can be adopted to manipulate the pre-existing electron density and in turn control the electron states within the IB [5].

Before introducing the next topic, it is worth discussing about the IC3. The restriction IC3 imposed on carrier extraction from CB to IB and IB to VB is a direct violation to the SQ model. During the practical implementations, almost all devices suffer from voltage loss which is caused by the carrier escapes at the IB [6]–[9]. In Shockley and Queisser’s 1961

publication, it explicitly states that the inclusion of impurities in attempt to absorb longer wavelength radiation appears to shunt the cell and result in lower device performance [10].

### 1.1.2 Quantum dot solar cell

Quantum dot solar cell (QDSC) is the main focus of this thesis, it can be used to implement the IBSCs as well as to develop its own branch of research such as space application [4], [11], [12].

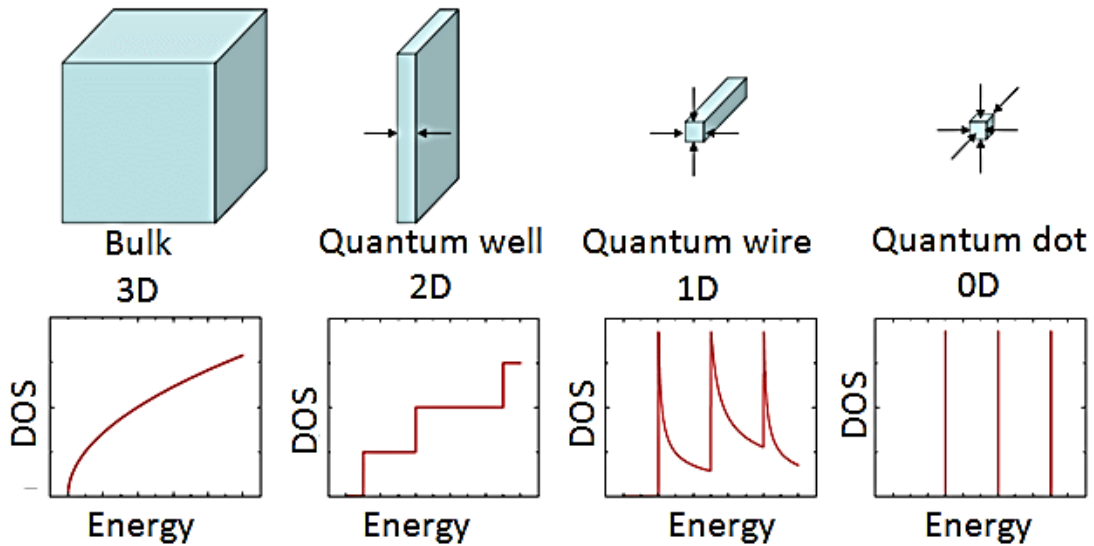


Figure 1.2 Schematics of DOS versus bulk, quantum well, quantum wire and quantum dot [13]

Quantum dots (QDs) are materials with zero-dimensional (0D) physical size, as illustrated in Figure 1.2. Unlike bulk (3D), quantum well (2D) or quantum wire (1D) structures, QDs with 0D have the least amount of energy states, i.e. lowest density of states (DOS). The scarcity of energy levels reduces the probability of electron transition and increases the transition energy. Hence, QDs have discrete energy levels, which confine electron movement and temperature independence. To implement the IBSC, the role of the IB can be performed by the discrete energy levels of QDs. Moreover, the size of the bandgap can be tuned by controlling the size of the QDs.

Furthermore, due to the small physical size, QDs have radiation tolerance. Under space environment, constant cosmic radiations have deteriorating impacts on the bulk SC performance. QDSCs, on the other hand, are more immune to the alpha-particle bombardments due to its smaller operational size [14]. Thus, QDSCs have the potential for space application.

### 1.1.3 Quantum dot intermediate band solar cell

In 2002, Luque and Marti displayed a detailed design of IBSC that employs QDs as the IB material [14]. To achieve the optimal bandgap configuration (1.95 eV, 1.24 eV, 0.71 eV), AlGaAs material with a bandgap tunability between 1.42 to 2.12 eV is chosen as the host material at Al composition of 0.4. InGaAs QDs with a radius of 3.9 nm has a bandgap of 1.24 eV that can implement the IB material. Furthermore, dot spacing between individual QDs should not exceed 10 nm apart to ensure a high absorption coefficient and dot regularity should not disperse greater than 10%, i.e. the sizes of QDs should be as uniform as possible, to maintain a narrow bandwidth of the IB. In terms of doping, n-type dopants with concentration between  $10^{16}$  and  $4 \times 10^{18} \text{ cm}^{-3}$  are suitable for QDs spaced between 10 nm to 90 nm to gain one impurity per dot.

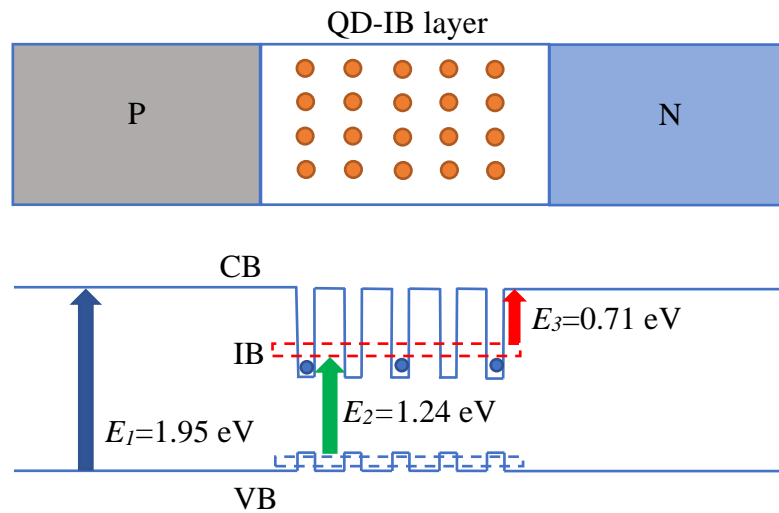


Figure 1.3 Structure of a QD-IBSC prototype with the corresponding band diagram

Figure 1.3 illustrates the prototype of QD-IBSC with band structure. Five layers of InGaAs QDs are incorporated between the AlGaAs host materials. The alternating AlGaAs and InGaAs QD layers at the intrinsic region form a pseudo IB energy level (red dotted box). The blue dotted box shows the effective energy level of the VB. The IB is partially filled with electrons by doping the QDs with n-type dopants. Photons with  $E_1$  can be absorbed by AlGaAs material, photons with  $E_2$  can be absorbed by the InGaAs QDs and with an additional absorption of photon with  $E_3$ . Due to partial filling, photon absorption at  $E_3$  is possible without the necessity of  $E_2$  absorption. Thus, the function of IBSC is realised.

#### 1.1.4 Review of the challenges and progress

In effort to implement the IBSC using QDs, many challenges must be addressed. Besides theoretical limitations such as partial filling and carrier escape, practical issues such as lattice mismatch and bandgap tunability also need to be resolved. In this section, a variety of methods for addressing these issues, as well as current progresses in QD-IBSC, are discussed.

In the early-stage of research, the growth of high quality QDs was the main challenge. Methods such as deploying strain-balancing layers, Sb-mediated layers were adopted to achieve stacking of multiple QD layers, high population density of QDs per layer and uniform shape of each QDs. One side effect of non-uniformity originated from Sb-mediated growth was discovered and addressed.

Post high quality QD growth, a reasonable QD sample can be fabricated into QDSC devices and, hence, IBSC mechanisms can be investigated. However, the two-step photon detection of QDSC was not satisfactory to demonstrate the operational IBSC mechanism.

It was recently discovered that the photon detection was hindered by a phenomenon called carrier escape, which remains one of the major challenges needing to overcome. Many methods were proposed to tackle this problem however there is, currently, no effective approaches to eliminate it; only mitigation of it. The first investigation of this thesis has also made its attempt to tackle this problem using a novel approach, discussed in Chapter 4.

Partial filling has always been a requirement to implement the IBSC and it has been addressed by doping the QDs with n-type Si-dopants. However, there are some minor side effects, such as current loss, require further refinements in the doping techniques. The second investigation of this thesis aim to identify the cause of the side effects and propose a method to negate the side effects, more details in Chapter 5.

Other (miscellaneous) techniques aiming to improve the device performance of the QDSC (such as adopting Type-II bandgap materials) are also included. The third investigation of this thesis (Chapter 6) utilises AlGaAs as a host material to improve the overall efficiency of the QDSC.

#### *1.1.4.1 Strain-balancing layers*

Growing nano-particles like QDs require extreme machine precision. The most advanced technique is to use molecular beam epitaxy (MBE) under Stranski-Krastanow (S-K) growth mode. However, during the growth process, 0.9 % lattice mismatch between  $\text{In}_{0.58}\text{Ga}_{0.42}\text{As}$  (5.7 Å) and  $\text{Al}_{0.4}\text{Ga}_{0.6}\text{As}$  (5.6 Å) materials inevitably accumulate strain at the layer interface [4]. When strained layers stack on top of each other, threading dislocations are formed which cause non-uniform QDs i.e. QDs grown at the bottom appear to have a smaller size than QDs at the top layers. Therefore, it is crucial to deploy strain-balancing layers. Figure 1.4 illustrates a plot of III-V materials with their lattice constant against bandgap energy. Type of bandgap and visible light region are also indicated.

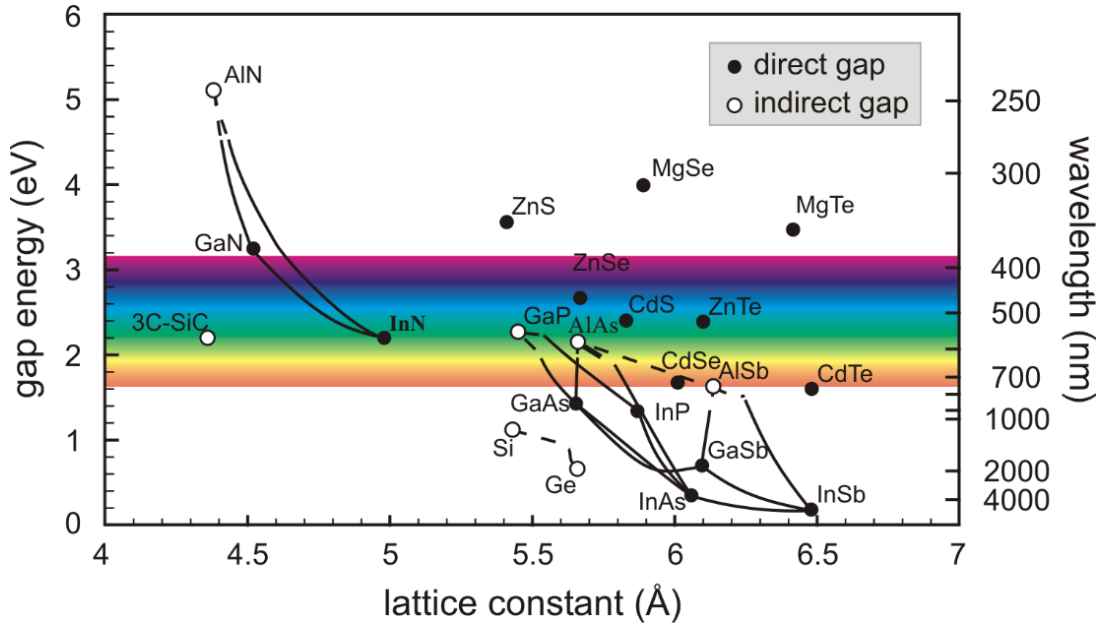


Figure 1.4 Group III-V material lattice constant vs gap energy and wavelength [15]

Okada *et al.* and Sugaya *et al.* have made remarkable progress on this topic [16]–[22]. Okada *et al.* have accomplished the growth of 100 layers of QDs without threading dislocations using GaNAs material as strain-compensating layers. Hence, an enhancement in current output due to increased photocurrent production has been reported [23], [24]. Sugaya *et al.* have reached a record of 400 layers of QDs without deploying any strain balancing techniques and observed no crystal quality degradation, no dislocations or crystal defects. Strain balancing layers can also be implemented using GaP materials which have led to the performance enhancements in devices with up to 50 QD layers [25]–[27].

#### 1.1.4.2 High density quantum dot arrays

To ensure the SC devices have a very large sub-bandgap absorption, the population of QDs must be dense. This can be achieved by means of increasing the number of QD layers or the density of QDs per single layer [28].

Two methods have been discovered by Faleev *et al.* and Tutu *et al.* to increase the QD density: to optimise the QD growth condition and to include Antimony (Sb) material to the

wetting layer (WL) which is situated underneath the QDs [29]–[31]. In method one, Tutu *et al.* have grown two QDSC samples at 510 °C and 580 °C, respectively. Although the AFM images illustrated the same QD density ( $\sim 5.5 \times 10^{10} \text{ cm}^{-2}$ ) for both samples, the TEM images revealed a large amount of threading dislocations for the sample grown at 510 °C, hence, significant reduction in the current density (19.53 to 3.75 mA/cm<sup>2</sup>). In method two, Faleev *et al.* reported an increase in QD density from  $2.5 \times 10^{10}$  to  $9.5 \times 10^{10} \text{ cm}^{-2}$  with Sb composition increased from 8 % to 17 %. Tutu *et al.* reported a  $1 \times 10^{11} \text{ cm}^{-2}$  QD density with Sb-mediated growth but a  $4.8 \times 10^{10} \text{ cm}^{-2}$  QD density without. The inclusion of Sb reduces the size and increases the density of the QDs, as a result, high spectral response in the sub-bandgap region is observed.

#### 1.1.4.3 Non-uniformity

Non-uniformity refers to the irregular sizes of QDs. Similar to non-periodic distribution of QD arrays, non-uniformity causes weak absorption coefficient between IB and CB [3]. The bandwidth of the IB becomes wider, and hence, reduces the effective bandgap energy between IB and CB. As a result, voltage output is shunted lower.

The introduction of Sb material to the WL reduces the physical size of the QDs and increases the density of QDs. However, it has a side effect of bimodal QD sizes i.e. two irregular sizes of QDs. Without Sb materials in the WL, QDs are uniform with an average height of 5 nm; with the insertion of Sb, the height distribution of QDs are clustered into 3 nm or 7 nm height [29]. This phenomenon can be visualised in 3D-AFM (atomic force microscopy) images [32]. Simultaneously, PL measurements can confirm this appearance by showing a broad peak i.e. a high FWHM (full width at half maximum) of QDs. The voltage output of bimodal QDs decreases from 0.78 to 0.60 V with an increasing amount of Sb composition from 0 % to 21% [33].

#### 1.1.4.4 Two-step photon absorption

Two-step photon absorption describes a desired phenomenon of an electron simultaneously absorbing two photons with sub-bandgap energy  $E_2$  and  $E_3$  in **Error! Reference source not found.** and leap from the VB into the CB [34]. It is the fundamental operation principle of an ideal IBSC therefore the detection of this phenomenon is crucial for QDSCs in determining its potential to implement the IBSC. Due to thermal carrier escape, which removes the need for second photon absorption, the observation of electron transition between IB—CB has been elusive [35].

Great efforts have been dedicated to detecting the two-step photon absorption [36]–[38]. In particular, Nozawa *et al.* have demonstrated direct observation of two-step photon absorption in a single InAs QD. The measurements were carried out by illuminating the QD with two lasers at wavelengths equal to VB—IB and IB—CB transition energies. Photocurrent data confirmed an increase in current output when both lasers are active and the increase in current output is proportional to the power of the secondary laser. Thus, the finding has proven that QD is the rightful candidate to implement the IBSC.

### 1.1.4.5 Carrier escape

Carrier escape describes an undesired phenomenon of an electron being pumped from IB into the CB through tunnelling or thermalisation without the absorption of a second photon [7], [8], [39]. Due to the characteristics of S-K growth mode which relies on forming self-assembled QDs via WLs, carrier escape becomes inevitable.

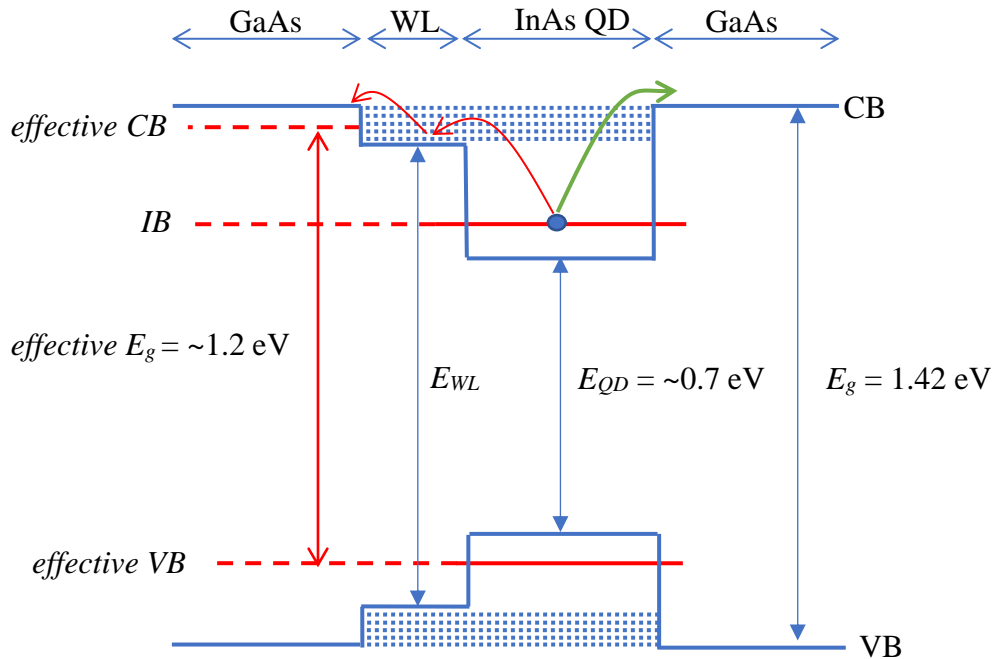


Figure 1.5 Band configuration of InAs QD/GaAs QDSC including the effect of WL

Figure 1.5 illustrates a band configuration of InAs QD/GaAs QDSC. The nature of the WL is a 2D quantum well (QW) which has continuous energy bands instead of discrete energy levels. The combination of QDs above QW, also known as dot-in-well (DWELL), results in a hybrid QW-QD characteristic at their interface [40]. Therefore, under strict theory, DWELL configuration is not the desired QD configuration. Electrons within the IB can leap into the CB via WL following the red arrows instead of the green, indicated in the figure. As a result, the *effective* bandgap which should be between CB and VB ( $E_g = 1.42$  eV) is reduced to  $\sim 1.2$  eV, and thus lead to an increase in current density but a drastic decrease in voltage; overall the conversion efficiency is diminished.



An alternative approach to limit carrier escape has been demonstrated by Lam *et al.* through QD charging via Si-dopants [44].

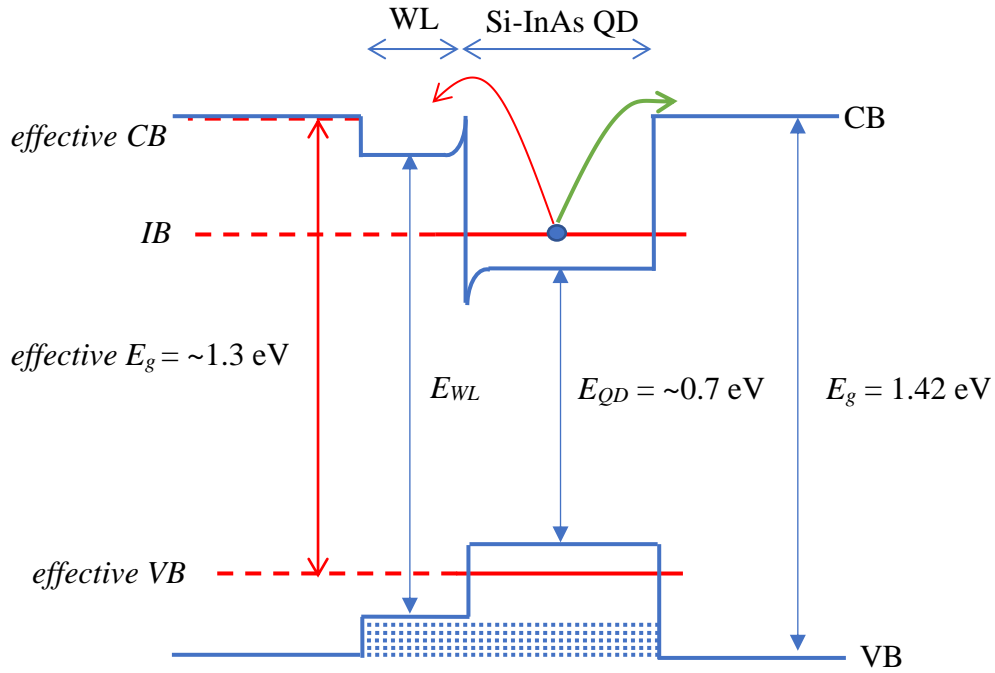


Figure 1.7 Band configuration of InAs QD/GaAs QDSC with Si-doped QDs

Figure 1.7 updates Figure 1.5 with Si-doped InAs QDs. This differs from Figure 1.6 which illustrates the barrier at the QD/GaAs interface, Si-doped QDs have a (delta-shaped) charged barrier at the QD/WL interface. This has a direct impact on limiting the transition between IB and CB, indicated by a larger size of red arrow. Hence, thermal activation energy is raised along with *effective* bandgap and voltage output. More so, the size of the barrier is adjustable through controlling the Si-dopant level. Voltage output increased from 0.77 to 0.88 V with Si-dopants increased from 0 electron per dot to 18 electron per dot.

#### 1.1.4.6 Partial filling

Partial filling of the IB describes the occupancy of energy states by electrons within the IB [5]. It is another fundamental operation principle that ensures high sub-bandgap absorption. A partially filled IB has valence states to allow electrons to be excited from the VB while

having occupied states to pump electrons to the CB. It is achieved by introducing n-type dopants which injects electrons to the IB. In QDSC applications, InAs QDs are doped with Si dopants. Moreover, the level of filling, partial or half, can be controlled by adjusting the Si dopant density [45].

Much progress has been made on the topic of doping, comprehensive investigations into the type of dopants, density of dopants, position of dopants and techniques of doping were conducted [44], [46]–[53]. Sablon *et al.* have reported a ground-breaking 50 % enhancement in overall efficiency by doping the interdot spacer layer with Si. Yang *et al.*, Lam *et al.* and Kim *et al.* have achieved improvements in open-circuit voltage by directly doping the InAs QDs with Si. Zhou *et al.* and Driscoll *et al.* discovered the possibility of background doping by locating QDs into the base (n-type) region of the QDSC.

#### 1.1.4.7 Type-II bandgap QD

Unlike type I conventional InAs QDs, type II QDs have a staggered band configuration as shown in Figure 1.8. This configuration leads to a different VB—IB transition which is potentially desirable to achieve the partial filling of IBSC [54], [56]. Type II QDs do not have hole bound states, and, hence, they acquire electrons from the host material to be

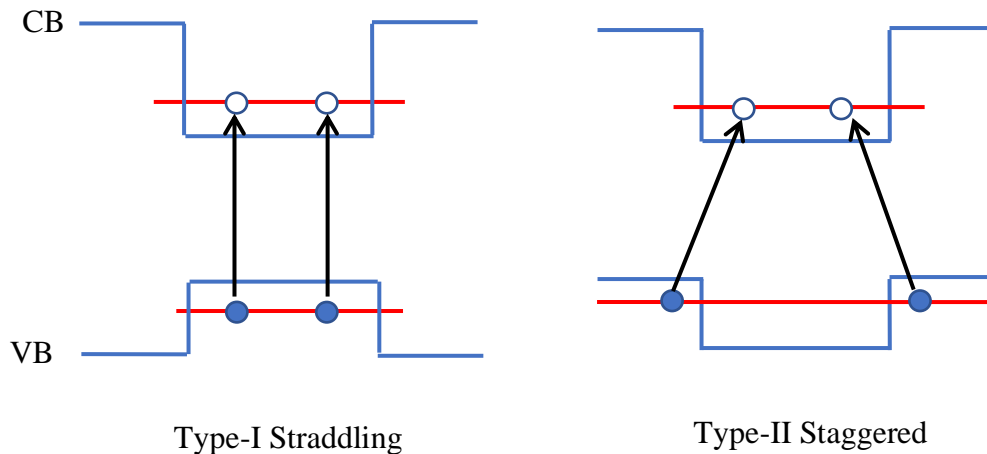


Figure 1.8 Diagram of type-I and type-II bandgap

excited into the CB. A repetition of this band configuration results in a pseudo IB with inherent partial filling.

Sb material is used to achieve a type II bandgap, which is deployed in the forms of QD capping layers or direct impurities to the dots [57]–[62]. He *et al.* have succeeded in the growth of InSb/GaAs QDSC, and reported a clear increase in the carrier lifetime through the time-resolved photoluminescence (TRPL). The TRPL data have also confirmed that an increase in the Sb composition has led to longer carrier lifetimes, and thus, proving the band alignment transforms from type I to type II.

## 1.2 Thesis structure

This thesis comprises 7 chapters to describe the development of QD-IBSCs.

Chapter 1 introduces the QDSC with the concept of IBSC and gives an overview of the challenges and progress made in the implementation of the QD-IBSCs.

Chapter 2 explains the fundamental mechanisms behind conventional solar cells and demonstrates how they can be integrated onto the IBSC concept.

Chapter 3 details the experimental procedures required to grow, fabricate and characterise the QDSCs.

Chapter 4 to 6 are the three investigations (mentioned in the review section) carried out during the course of PhD research: Chapter 4 presents the investigation on background Si doping by embedding QDs into the n-type base region of the SC. Chapter 5 investigates the origin of current loss caused by Si doping, and proposes a method to recover the lost current without compromising any voltage output. Chapter 6 aims to achieve the optimum bandgap configuration for IBSC by deploying AlGaAs as a host material.

Chapter 7 concludes the thesis by highlighting all the findings of the PhD study. Ongoing investigations and future research recommendations are also indicated.

### 1.3 References

- [1] A. Luque and A. Martí, “Increasing the Efficiency of Ideal Solar Cells by Photon Induced Transitions at Intermediate Levels,” *Phys. Rev. Lett.*, vol.78, no.26, pp. 5014-5017, Jun. 1997.
- [2] A. Luque, A. Martí, and C. Stanley, “Understanding intermediate-band solar cells,” *Nat. Photonics*, vol. 6, no. 3, pp. 146–152, 2012.
- [3] A. Martí, N. Lopez, E. Antolin, E. Canovas, C. Stanley, C. Farmer, L. Cuadra, and A. Luque, “Novel semiconductor solar cell structures: The quantum dot intermediate band solar cell,” *Thin Solid Films*, vol. 511–512, pp. 638–644, 2006.
- [4] A. Marti, L. Cuadra, and A. Luque, “Quantum dot intermediate band solar cell,” *Conf. Rec. IEEE Photovolt. Spec. Conf.*, Anchorage AK USA, vol. 2000-Jan, pp. 940–943, 2000.
- [5] A. Martí, L. Cuadra, and A. Luque, “Partial filling of a quantum dot intermediate band for solar cells,” *IEEE Trans. Electron Devices*, vol. 48, no. 10, pp. 2394–2399, 2001.
- [6] P. Frigeri and S. Franchi, “Carrier thermal escape and retrapping in self-assembled quantum dots,” *Phys. Rev. B - Condens. Matter Mater. Phys.*, vol. 60, no. 11, pp. 8276–8283, Sep. 1999.
- [7] E. Antolín, A. Marti, C. Farmer, P. Linares, E. Hernandez, A. Sanchez, T. Ben, S. Molina, C. Stanley, and A. Luque, “Reducing carrier escape in the InAs/GaAs quantum dot intermediate band solar cell,” *J. Appl. Phys.*, vol. 108, no. 6, p. 064513, Sep. 2010.
- [8] D. G. Sellers, S. Polly, S. M. Hubbard, and M. F. Doty, “Analyzing carrier escape mechanisms in InAs/GaAs quantum dot p-i-n junction photovoltaic cells,” *Appl. Phys. Lett.*, vol. 104, no. 22, p. 223903, 2014.
- [9] Y. Dai, C. G. Bailey, C. Kerestes, D. V. Forbes, and S. M. Hubbard, “Investigation

- of carrier escape mechanism in InAs/GaAs quantum dot solar cells,” *Conf. Rec. IEEE Photovolt. Spec. Conf.*, Austin TX USA, pp. 39–44, 2012.
- [10] W. Shockley and H. J. Queisser, “Detailed balance limit of efficiency of p-n junction solar cells,” *J. Appl. Phys.*, vol. 32, no. 3, pp. 510–519, Mar. 1961
- [11] S. M. Hubbard, “Nanostructured photovoltaics for space power,” *J. Nanophotonics*, vol. 3, no. 1, p. 031880, 2009.
- [12] S. Sinharoy, C. W. King, S. G. Bailey, and R. P. Raffaele, “InAs quantum dot development for enhanced InGaAs space solar cells,” *Conf. Rec. IEEE Photovolt. Spec. Conf.*, Lake Buena Vista FL USA pp. 94–97, 2005.
- [13] M. Jayawardhana and K. Wijewardena Gamalath, “Electronic structures of CdSe quantum dots embedded in ZnSe,” *World Sci. News*, vol. 86, no. 3, pp. 205–225, 2017.
- [14] C. D. Cress, S. M. Hubbard, B. J. Landi, R. P. Raffaele, and D. M. Wilt, “Quantum dot solar cell tolerance to alpha-particle irradiation,” *Appl. Phys. Lett.*, vol. 91, no. 18, pp. 10–13, 2007.
- [15] H. Ibach and H. Lueth. *Solid-State Physics*. Springer Verlag, 2003.
- [16] A. Martí, L. Cuadra, and A. Luque, “Design constraints of the quantum-dot intermediate band solar cell,” *Phys. E Low-Dimensional Syst. Nanostructures*, vol. 14, no. 1–2, pp. 150–157, 2002.
- [17] R. Oshima, T. Hashimoto, H. Shigekawa, and Y. Okada, “Multiple stacking of self-assembled InAs quantum dots embedded by GaNAs strain compensating layers,” *J. Appl. Phys.*, vol. 100, no. 8, pp. 1–4, 2006.
- [18] R. Oshima, A. Takata, and Y. Okada, “Strain-compensated InAs/GaNAs quantum dots for use in high-efficiency solar cells,” *Appl. Phys. Lett.*, vol. 93, no. 8, p. 083111, Aug. 2008.

- [19] T. Morioka, R. Oshima, A. Takata, Y. Shoji, T. Inoue, T. Kita, and Y. Okada, “Multi-stacked InAs/GaNAs quantum dots with direct Si doping for use in intermediate band solar cell,” *Conf. Rec. IEEE Photovolt. Spec. Conf.*, pp. 1834–1837, 2010.
- [20] T. Sugaya, S. Furue, H. Komaki, T. Amano, M. Mori, K. Komori, S. Niki, O. Numakami, and Y. Okano “Highly stacked and well-aligned In<sub>0.4</sub>Ga<sub>0.6</sub>As quantum dot solar cells with In<sub>0.2</sub>Ga<sub>0.8</sub>As cap layer,” *Appl. Phys. Lett.*, vol. 97, no. 18, pp. 5–7, 2010.
- [21] A. Takata, R. Oshima, Y. Shoji, K. Akahane, and Y. Okada, “Fabrication of 100 layer-stacked InAs/GaNAs strain-compensated quantum dots on GaAs (001) for application to intermediate band solar cell,” *Conf. Rec. IEEE Photovolt. Spec. Conf.*, Honolulu HI USA, no. 001, pp. 1877–1880, 2010.
- [22] R. Oshima, Y. Okada, A. Takata, S. Yagi, K. Akahane, R. Tamaki, and K. Miyano, “High-density quantum dot superlattice for application to high-efficiency solar cells,” *Phys. Status Solidi Curr. Top. Solid State Phys.*, vol. 8, no. 2, pp. 619–621, 2011.
- [23] T. Sugaya, O. Numakami, R. Oshima, S. Furue, H. Komaki, T. Amano, K. Matsubara, Y. Okano, and S. Niki, “Ultra-high stacks of InGaAs/GaAs quantum dots for high efficiency solar cells,” *Energy Environ. Sci.*, vol. 5, no. 3, pp. 6233–6237, 2012.
- [24] T. Morioka, Y. Shoji, and Y. Okada, “Current enhancement in direct-doped InAs/GaNAs strain-compensated quantum dot solar cell,” *Conf. Rec. IEEE Photovolt. Spec. Conf.*, Seattle WA USA, pp. 003499–003502, 2011.
- [25] Y. Okada, T. Morioka, K. Yoshida, R. Oshima, Y. Shoji, T. Inoue, and T. Kita “Increase in photocurrent by optical transitions via intermediate quantum states in direct-doped InAs/GaNAs strain-compensated quantum dot solar cell,” *J. Appl. Phys.*, vol. 109, no. 2, p. 024301, 2011.
- [26] R. B. Laghumavarapu, M. El-Emawy, N. Nuntawong, A. Moscho, L. F. Lester, and

- D. L. Huffaker, "Improved device performance of InAsGaAs quantum dot solar cells with GaP strain compensation layers," *Appl. Phys. Lett.*, vol. 91, no. 24, pp. 2007–2009, 2007.
- [27] D. Alonso-Álvarez, A. Taboada, J. Ripalda, B. Aln, Y. Gonzalez, L. Gonazalez, J. Garcia, F. Briones, A. Marti, A. Luque, A. Sanchez, and S. Molina, "Carrier recombination effects in strain compensated quantum dot stacks embedded in solar cells," *Appl. Phys. Lett.*, vol. 93, no. 12, pp. 2008–2010, 2008.
- [28] S. M. Hubbard, C. D. Cress, C. G. Bailey, R. P. Raffaele, S. G. Bailey, and D. M. Wilt, "Effect of strain compensation on quantum dot enhanced GaAs solar cells," *Appl. Phys. Lett.*, vol. 92, no. 12, pp. 2008–2010, 2008.
- [29] A. Mellor, A. Luque, I. Tobías, and A. Martí, "The influence of quantum dot size on the sub-bandgap intraband photocurrent in intermediate band solar cells," *Appl. Phys. Lett.*, vol. 101, no. 13, p. 133909, 2012.
- [30] N. Faleev, K. Y. Ban, S. Bremner, D. J. Smith, and C. Honsberg, "Investigation of the main correlations between structural and physical properties of InAs quantum dots, embedded between strain-relief GaAsSb layers," *Conf. Rec. IEEE Photovolt. Spec. Conf.*, Seattle WA USA, pp. 000474–000479, 2011.
- [31] F. K. Tutu, I. Sellers, M. Peinado, C. Pastore, S. Willis, A. Watt, T. Wang, and H. Liu, "Improved performance of multilayer InAs/GaAs quantum-dot solar cells using a high-growth-temperature GaAs spacer layer," *J. Appl. Phys.*, vol. 111, no. 4, p. 046101, Feb. 2012.
- [32] F. K. Tutu, J. Wu, P. Lam, M. Tang, N. Miyashita, Y. Okada, J. Wilson, R. Allison, and H. Liu, "Antimony mediated growth of high-density InAs quantum dots for photovoltaic cells," *Appl. Phys. Lett.*, vol. 103, no. 4, p. 043901, 2013.
- [33] D. Kim, S. Hatch, J. Wu, K. Sablon, P. Lam, P. Jurczak, M. Tang, W. Gillin, and H. Liu, "Type-II InAs/GaAsSb Quantum Dot Solar Cells with GaAs Interlayer," *IEEE J. Photovoltaics*, vol. 8, no. 3, pp. 741–745, 2018.

- [34] S. Hatch, J. Wu, K. Sablon, P. Lam, M. Tang, Q. Jiang, and H. Liu, “InAs/GaAsSb quantum dot solar cells,” *Opt. Express*, vol. 22, no. S3, p. A679–A685, 2014.
- [35] A. Martí, E. Antonlin, C. Stanley, C. Farmer, N. Lopez, P. Diaz, E. Canovas, P. Linares, A. Luque, “Production of photocurrent due to intermediate-to-conduction-band transitions: A demonstration of a key operating principle of the intermediate-band solar cell,” *Phys. Rev. Lett.*, vol. 97, no. 24, pp. 1–4, 2006.
- [36] A. Luque, A. Marti, E. Antolin, and P. Garcia-Linares, “Intraband absorption for normal illumination in quantum dot intermediate band solar cells,” *Sol. Energy Mater. Sol. Cells*, vol. 94, no. 12, pp. 2032–2035, 2010..
- [37] M. Sugiyama, Y. Wang, K. Watanabe, T. Morioka, Y. Okada, and Y. Nakano, “Photocurrent generation by two-step photon absorption with Quantum-well superlattice cell,” *IEEE J. Photovoltaics*, vol. 2, no. 3, pp. 298–302, 2012.
- [38] R. Tamaki, Y. Shoji, Y. Okada, and K. Miyano, “Spectrally resolved intraband transitions on two-step photon absorption in InGaAs/GaAs quantum dot solar cell,” *Appl. Phys. Lett.*, vol. 105, no. 7, pp. 1–5, 2014.
- [39] T. Nozawa, H. Takagi, K. Watanabe, and Y. Arakawa, “Direct Observation of Two-Step Photon Absorption in an InAs/GaAs Single Quantum Dot for the Operation of Intermediate-Band Solar Cells,” *Nano Lett.*, vol. 15, no. 7, pp. 4483–4487, 2015.
- [40] A. Luque and A. Martí, “The intermediate band solar cell: Progress toward the realization of an attractive concept,” *Adv. Mater.*, vol. 22, no. 2, pp. 160–174, Jan. 2010.
- [41] S. Huang, A. V. Semichaevsky, L. Webster, H. T. Johnson, and R. S. Goldman, “Influence of wetting layers and quantum dot size distribution on intermediate band formation in InAs/GaAs superlattices,” *J. Appl. Phys.*, vol. 110, no. 7, p. 073105, 2011.
- [42] F. K. Tutu, P. Lam, J. Wu, N. Miyashita, Y. Okada, K. Lee, N. Ekins-Daukes, J.

- Wilson, and H. Liu, "InAs/GaAs quantum dot solar cell with an AlAs cap layer," *Appl. Phys. Lett.*, vol. 102, no. 16, p. 163907, 2013.
- [43] G. Wei and S. R. Forrest, "Intermediate-band solar cells employing quantum dots embedded in an energy fence barrier," *Nano Lett.*, vol. 7, no. 1, pp. 218–222, 2007.
- [44] S. Asahi, H. Teranishi, N. Kasamatsu, T. Kada, T. Kaizu, and T. Kita, "Suppression of thermal carrier escape and efficient photo-carrier generation by two-step photon absorption in InAs quantum dot intermediate-band solar cells using a dot-in-well structure," *J. Appl. Phys.*, vol. 116, no. 6, p. 063510, 2014.
- [45] P. Lam, S. Hatch, J. Wu, M. Tang, V. Dorogan, Y. Mazur, G. Salamo, I. Ramiro, A. Seeds, and H. Liu, "Voltage recovery in charged InAs/GaAs quantum dot solar cells," *Nano Energy*, vol. 6, pp. 159–166, 2014.
- [46] A. Martí, E. Antolín, P. García-Linares, I. Ramiro, I. Artacho, E. López, E. Hernández, M. J. Mendes, A. Mellor, I. Tobías, D. Fuertes Marrón, C. Tablero, A. B. Cristóbal, C. G. Bailey, M. Gonzalez, M. Yakes, M. P. Lumb, R. Walters, and A. Luque, "Six not so easy pieces in intermediate band solar cell research," *Physics, Simulation, Photonic Eng. Photovolt. Devices II*, vol. 8620, no. photon 1, p. 86200J, 2013.
- [47] A. Luque, A. Marti, N. Lopez, E. Antolin, E. Canovas, C. Stanley, C. Farmer, and P. Diaz "Operation of the intermediate band solar cell under nonideal space charge region conditions and half filling of the intermediate band," *J. Appl. Phys.*, vol. 99, no. 9, pp. 1–9, 2006.
- [48] X. Yang, K. Wang, Y. Gu, H. Ni, X. Wang, T. Yang, and Z. Wang, "Improved efficiency of InAs/GaAs quantum dots solar cells by Si-doping," *Sol. Energy Mater. Sol. Cells*, vol. 113, pp. 144–147, 2013.
- [49] K. A. Sablon, J. W. Little, V. Mitin, A. Sergeev, N. Vagidov, and K. Reinhardt, "Strong enhancement of solar cell efficiency due to quantum dots with built-in charge," *Nano Lett.*, vol. 11, no. 6, pp. 2311–2317, 2011.

- [50] K. Driscoll, M. F. Bennett, S. J. Polly, D. V. Forbes, and S. M. Hubbard, "Effect of quantum dot position and background doping on the performance of quantum dot enhanced GaAs solar cells," *Appl. Phys. Lett.*, vol. 104, no. 2, p. 023119, 2014.
- [51] D. Kim, M. Tang, J. Wu, S. Hatch, Y. Maidaniuk, V. Dorogan, Y. Mazur, G. Salamo, and H. Liu, "Si-Doped InAs/GaAs Quantum-Dot Solar Cell with AlAs Cap Layers," *IEEE J. Photovoltaics*, vol. 6, no. 4, pp. 906–911, 2016.
- [52] A. P. Cédola, D. Kim, A. Tibaldi, M. Tang, A. Khalili, J. Wu, H. Liu, and F. Cappelluti, "Physics-based modeling and experimental study of Si-doped InAs/GaAs quantum dot solar cells," *Int. J. Photoenergy*, vol. 2018, pp. 1–10, Feb. 2018.
- [53] D. Kim, S. Chan, M. Tang, J. Wu, and H. Liu, "The influence of direct, delta, and modulation QD Si doping on InAs/GaAs quantum dot solar cells," in *2018 IEEE 7th World Conference on Photovoltaic Energy Conversion, WCPEC 2018 - A Joint Conference of 45th IEEE PVSC, 28th PVSEC and 34th EU PVSEC*, Waikoloa HI USA, 2018, pp. 2759–2762.
- [54] D. Zhou, P. Vullum, G. Sharma, S. Thomassen, R. Holmestad, and T. Reenaas, and B. Fimland, "Positioning effects on quantum dot solar cells grown by molecular beam epitaxy," *Appl. Phys. Lett.*, vol. 96, no. 8, pp. 10–13, 2010.
- [55] L. Cuadra, A. Martí, and A. Luque, "Type II broken band heterostructure quantum dot to obtain a material for the intermediate band solar cell," *Phys. E Low-Dimensional Syst. Nanostructures*, vol. 14, no. 1–2, pp. 162–165, 2002.
- [56] A. Luque, P. G. Linares, A. Mellor, V. Andreev, and A. Martí, "Some advantages of intermediate band solar cells based on type II quantum dots," *Appl. Phys. Lett.*, vol. 103, no. 12, p. 123901, 2013.
- [57] W. H. Chang, Y. A. Liao, W. T. Hsu, M. C. Lee, P. C. Chiu, and J. I. Chyi, "Carrier dynamics of type-II InAsGaAs quantum dots covered by a thin GaAs<sub>1-x</sub>Sb<sub>x</sub> layer," *Appl. Phys. Lett.*, vol. 93, no. 3, pp. 28–31, 2008.

- [58] J. He, C. Reyner, B. Liang, K. Nunna, D. Huffaker, N. Pavarelli, K. Gradkowski, T. Ochalski, G. Huyet, V. Dorogan, Y. Mazur, and G. Salamo, “Band alignment tailoring of  $\text{InAs}_{1-x}\text{Sb}_x/\text{GaAs}$  quantum dots: Control of type I to type II transition,” *Nano Lett.*, vol. 10, no. 8, pp. 3052–3056, 2010.
- [59] W. T. Hsu, Y. A. Liao, F. C. Hsu, P. C. Chiu, J. I. Chyi, and W. H. Chang, “Effects of GaAsSb capping layer thickness on the optical properties of InAs quantum dots,” *Appl. Phys. Lett.*, vol. 99, no. 7, pp. 1–4, 2011.
- [60] J. He, F. Bao, and J. Zhang, “Capping effect of GaAsSb and InGaAsSb on the structural and optical properties of type II GaSb/GaAs quantum dots,” *Appl. Phys. Lett.*, vol. 100, no. 17, p. 171914, 2012.
- [61] J. Hwang, A. J. Martin, J. M. Millunchick, and J. D. Phillips, “Thermal emission in type-II GaSb/GaAs quantum dots and prospects for intermediate band solar energy conversion,” *J. Appl. Phys.*, vol. 111, no. 7, p. 074514, 2012.
- [62] S. Tomić, “Effect of Sb induced type II alignment on dynamical processes in InAs/GaAs/GaAsSb quantum dots: Implication to solar cell design,” *Appl. Phys. Lett.*, vol. 103, no. 7, p.072112, 2013.

## Chapter 2 Introduction to solar energy and solar cells

*This chapter sets forth the fundamental concepts required to understand the mechanism behind a conventional solar cell (SC). The solar resource and its interaction with semiconductor materials are first introduced. Followed by the illustration of the p-n junction model which is further derived into the SC operation mode.*

## 2.1 Solar resource

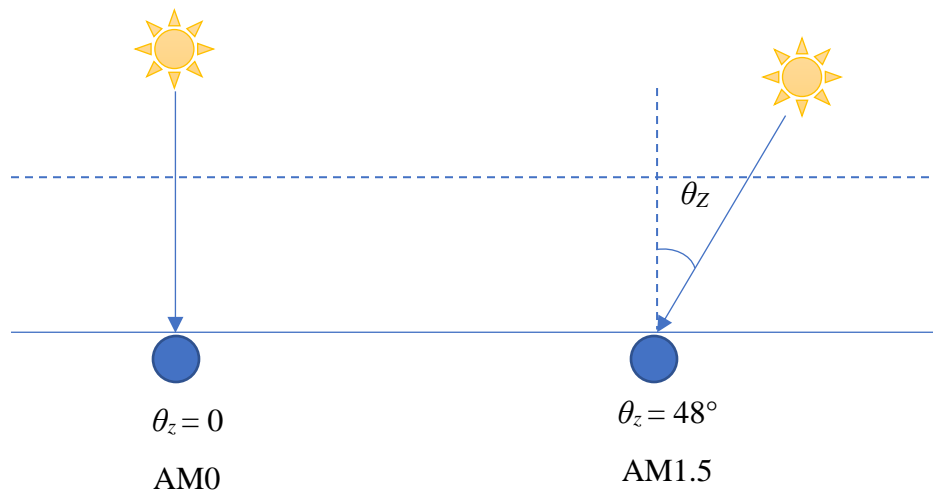
Large amount of energy is irradiated by the sun and it is wasteful not to harness this free energy. The wavelength of the sunlight extends from the ultraviolet (UV) region (10 nm-400 nm) to the visible light region (400 nm-700 nm) and beyond the infrared (IR) region (>700 nm) [1]. As the highest irradiance level occurs in the visible light region, solar cell engineers should focus on materials with strong absorption in this region.

Solar irradiance may be inconsistent due to the fluctuation of power emission of the sun, location on earth, time of the day, local atmospheric condition *etc.* Thus, a benchmark is required for universal researching and testing. The American Society for Testing and Materials (ASTM) photovoltaic research community has established three test conditions based on different air masses (AM1.5G, AM1.5D and AM0), as illustrated in Figure 2.1.

Air mass (AM) indicates the amount of atmosphere the sunlight must travel through before reaching the earth. It is expressed as [1]:

$$AM = \frac{1}{\cos(\theta_z)} \quad \text{Equation 2.1}$$

where  $\theta_z$  is the zenith angle, illustrated in Figure 2.1(a).



(a)

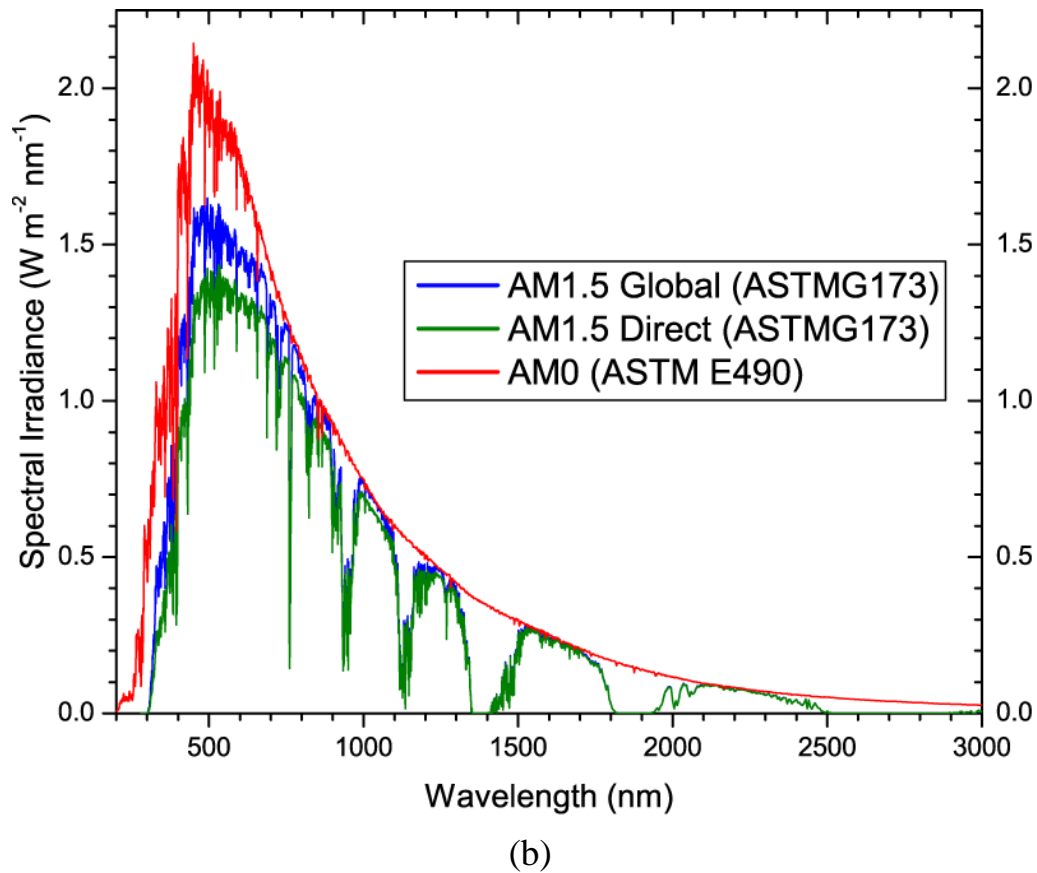


Figure 2.1 Schematic of (a) air mass and (b) ASTM Reference Spectra at AM1.5G, AM1.5D and AM0

AM0 ( $\theta_z = 0^\circ$ ) is the benchmark for extra-terrestrial, space SCs where the spectrum appears approximated by the black body radiation at 6000 K, as shown in Figure 2.1(b). AM1.5, given at  $\theta_z = 48^\circ$  which is the typical angle that takes into account the inconsistency factors, is the benchmark for terrestrial SCs which includes the atmospheric effects such as Rayleigh scattering and oxygen, ozone and water vapour absorptions. AM1.5Global has an integrated spectral irradiance of  $1000 \text{ W/m}^2$  and is used to test the flat panel modules mostly situated on roof tops or in solar cell fields. AM1.5Direct has an integrated spectral irradiance of  $900 \text{ W/m}^2$  and is used to test the solar concentrators of which the absorption of light is enhanced by heliostats (device that consist of one or multiple mirrors).

## 2.2 Semiconductors for solar cells

### 2.2.1 Optical properties

#### 2.2.1.1 Bandgap

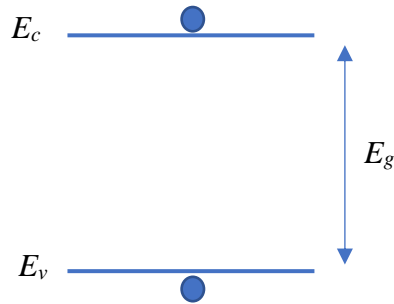


Figure 2.2 Simple schematic of a bandgap including CB and VB

A bandgap is a range of energy levels or a band of energy where carriers are not allowed to occupy. In other words, the bandgap is the difference in energy levels between the minimum point of the conduction band (CB) and the maximum point of the valence band (VB), as described in Equation 2.2. Figure 2.2 displays a simplified bandgap diagram. In order to excite an electron from VB to CB, the energy corresponding to the bandgap energy ( $E_g$ ) is required. For instance, electrons in Gallium Arsenide (GaAs) requires an energy of 1.42 eV to travel from VB to CB.

$$E_g = E_c - E_v \quad \text{Equation 2.2}$$

For the solar cell materials, the existence of a bandgap is essential because the scarcity of energy levels reduces the probability of an excited electron to relax back to its original position, which gives the excited electron an opportunity to be collected for external use. In case of metals, in contrast, the abundance of energy levels promotes electron transfers, which means that the excited electrons quickly decay back to the original position through the continuum of energy levels, thus rendering the electron incapable of being employed for external work.

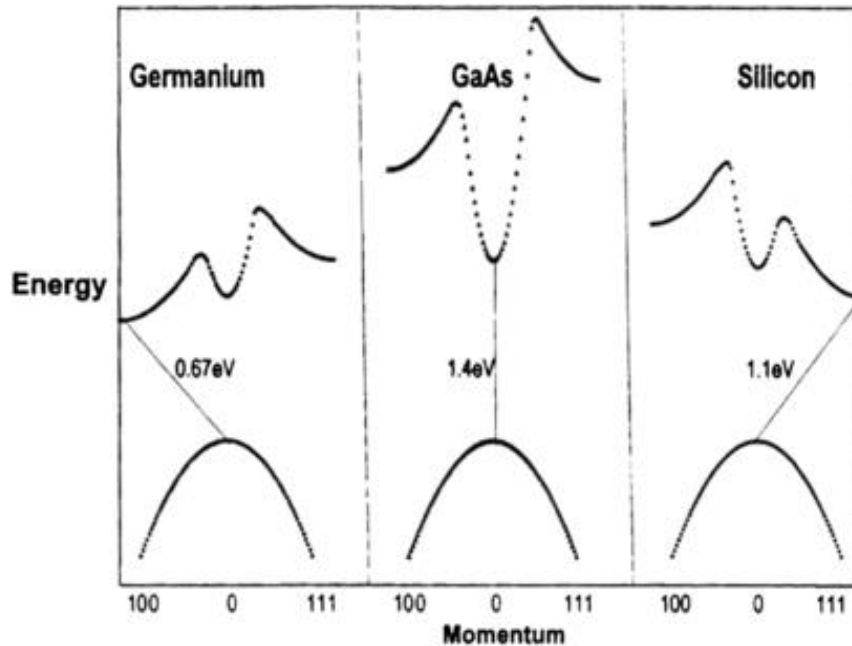


Figure 2.3 Direct and indirect bandgaps depicted using Ge, GaAs and Si

The bandgap can be classified into two types, direct and indirect bandgap. For the direct bandgap materials, the electrons from VB can be directly excited into the CB *without* changing the momentum because the minimum of CB is directly above the maximum of VB. In contrast, the indirect bandgap materials require an *excess* phonon to change the momentum, as well as their bandgap energy, because the wave-vectors of the CB minimum and the VB maximum are not the same. Figure 2.3 illustrates the bandgap of representative semiconductor materials: Germanium (Ge), GaAs and Silicon (Si). Unlike the direct bandgap material GaAs, Ge and Si require additional energy with their bandgap energy—1.1 eV and 0.67 eV, respectively—to excite the electrons into CB.

The choice of bandgap determines the range of light energies that the material can absorb, or in simple terms, the total amount of light which can be used to convert into electrical energy. For example, GaAs can only absorb the light with wavelength less than 870 nm and the rest of the spectrum is not utilised. Figure 2.4 indicates the amount of light that can be absorbed by the GaAs in shaded red colour and the unexploited light in clear.

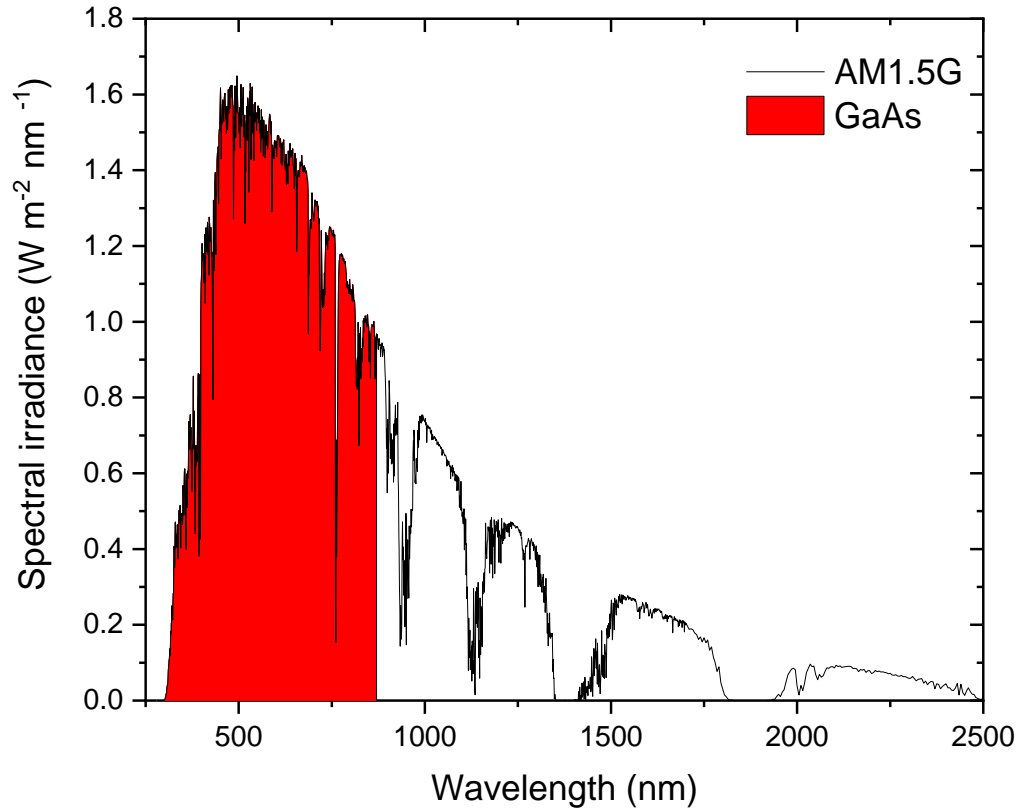


Figure 2.4 ASTM Spectra with GaAs absorption range

### 2.2.1.2 Absorption

Figure 2.5 illustrates the absorption of photons with different photon energy. When a photon (green) with energy exactly equal to the bandgap travels through a material, the photon is absorbed by the material and the absorbed energy is used to excite an electron across the bandgap. This transition of electron leaves a hole (absent electron) in VB, generating an electron-hole pair. For the photon (orange) with insufficient energy, it passes through the material without an interaction. With the photon (blue) having excess energy, electron-hole pair is generated, along with dissipation of heat energy ( $kT$ ).

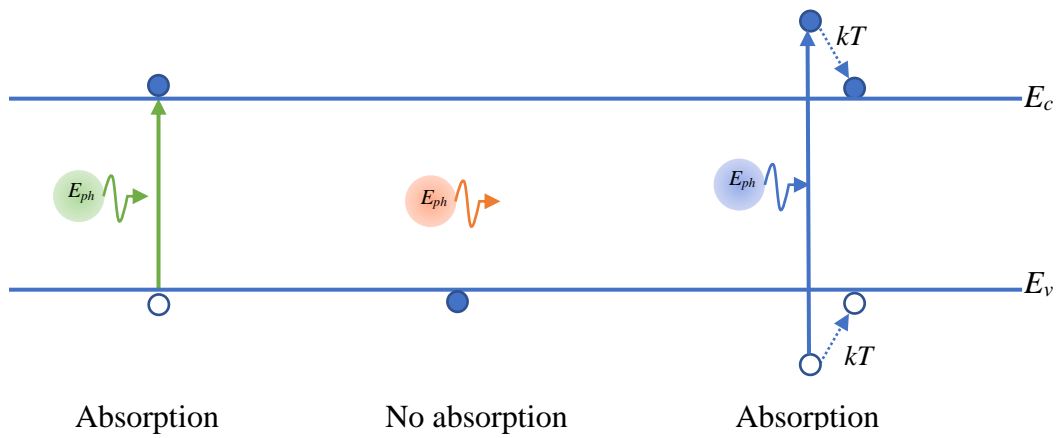


Figure 2.6 Schematic of photon absorption, no absorption and absorption with extra thermal energy

Absorption is an important process for SC operation since it generates electrons and holes which are required to power external devices. The efficacy of light absorption in materials

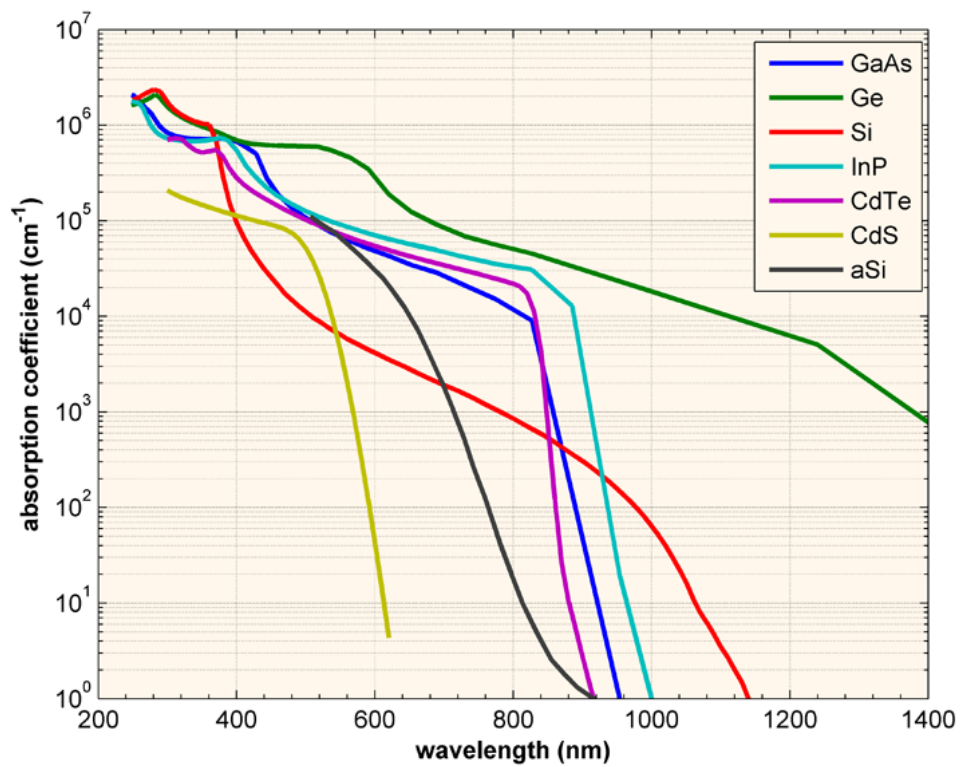


Figure 2.5 Absorption coefficients of semiconductor materials with direct and indirect bandgaps [2]

can be denoted as the absorption coefficient ( $\alpha$ ) which describes how readily the electrons can be excited into the CB.

Figure 2.6 presents a list of semiconductor materials with their corresponding  $\alpha$  at different wavelengths. In general, the direct bandgap materials (GaAs, InP, CdTe, CdS) have higher  $\alpha$  and sharper edges compared to the indirect bandgap materials (Ge, Si, aSi). A material with high  $\alpha$  requires thinner thickness to absorb a certain amount of light. For example, 3  $\mu\text{m}$ -thick GaAs absorbs the same amount of light as 300  $\mu\text{m}$ -thick Si. Therefore, the use of direct bandgap materials is beneficial to the performance of SC. Despite having a low  $\alpha$  and indirect bandgap, Si material is an extremely popular candidate for SCs that has, in fact, achieved a higher efficiency than GaAs materials. This is mainly due to the maturity of Si technology; in theory, if III-V technology has reached the same level of development, GaAs SCs would have achieved better performances.

#### *2.2.1.3 Recombination*

Recombination is the scattering of the excited electrons, which can be categorised into three types. Figure 2.7 illustrates three types of recombinations: (1) The electron collides with a hole, generating a photon with equivalent energy. This process is called radiative recombination. (2) The electron collides with defect-induced trap states within the bandgap ( $E_{trap}$ ), generating heat energy (phonon) instead of a photon. This non-radiative process is called Shockley-Read Hall (SRH) recombination. (3) The electron collides with another electron within the CB and excite that electron into higher energy states ( $E_I$ ) while relaxing itself back to the VB. This non-radiative recombination process was discovered by Pierre Auger and named as the Auger recombination.

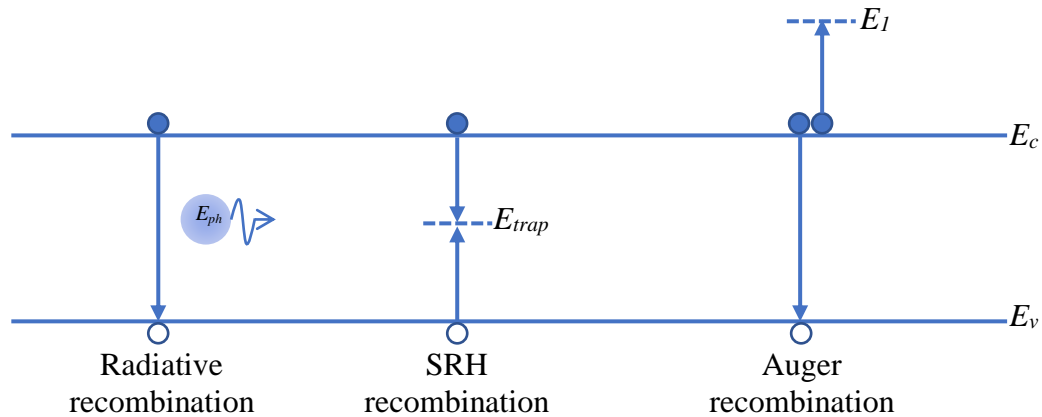


Figure 2.7 Three types of recombinations: radiative, SRH and Auger recombination

For SC operations, the recombination processes are undesirable because it is, ultimately, a loss of electron in the CB. Amongst the recombination processes, radiative recombination is less undesirable than the non-radiative recombinations as the generated photon can still excite electrons. Shockley-Read Hall recombination is the most dominant loss mechanism but this type of recombination can be partially avoided by improving the quality of the material. Auger recombination is inevitable because electrons must exist within the material however the rate of this recombination can be regulated by the number of electrons within the CB.

## 2.2.2 Doping and impurities

### 2.2.2.1 Intrinsic carrier concentration

At absolute zero ( $T = 0$  K) semiconductor materials without doping have no carriers to conduct electricity because the “intrinsic carrier concentration” ( $n_i$ ) is zero. In other words, the “self-contained carrier population” is not enough to conduct at 0 K. As the temperature increases, the bound electrons gain thermal energies to break free of the lattice and, hence, conduct some electricity. At room temperature ( $T = 300$  K) the  $n_i$  of Si, GaAs and Ge is  $1.5 \times 10^{10} \text{ cm}^{-3}$ ,  $1.8 \times 10^6 \text{ cm}^{-3}$  and  $2.4 \times 10^{13} \text{ cm}^{-3}$ , respectively. Ge has a higher conductivity due to the greater population.

### 2.2.2.2 Types of doping

Doping is a technique that can alter the “self-contained carrier population” within the material by replacing the base material atoms with dopant atoms, allowing semiconductors to conduct electricity at absolute zero. The n-type and p-type dopants are atoms which have surplus electrons and holes, respectively. For example, Si is an n-type dopant for GaAs material as Si (group IV) has as an extra electron compared to Ga (group III) and Beryllium (group II) is a p-type dopant for GaAs.

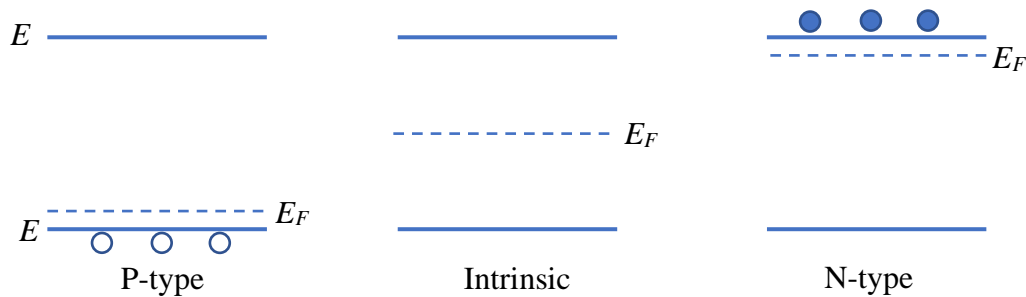


Figure 2.8 Effect of p- and n-type doping on the  $E_F$

Figure 2.8 illustrates the effects of doping on Fermi level ( $E_F$ ) of which describes the occupancy of energy states at  $T = 0$  K. By replacing the intrinsic atoms with donors or acceptors, the number of electrons or holes changes, resulting in the modification of the occupation of states. For instance, p-type material has less electrons, and, thus, the level of the highest filled electron state must be decreased so that  $E_F$  lowers. On the contrary, n-type material has more electrons, causing the  $E_F$  to be raised.

### 2.2.2.3 Majority and minority carriers

For the doped materials with the imbalanced number of electrons or holes, the type of carrier which has a higher and lower population is the called “majority carriers” and “minority carriers”, respectively. In n-type materials, electrons are the majority carriers and holes are the minority carriers; in p-type materials, holes are the majority carriers and electrons are the minority carriers.

### 2.2.3 Carrier transport

Carrier transport describes the motion of free carriers within the material. Electrons in CB and holes in VB are considered as free carriers and their movement is random. There is no particular path the carriers follow. However, when the carriers collide with other particles, they will scatter and change their direction. In the absence of external interference, semiconductors have a net carrier movement of zero; as though the carriers move randomly within the material, they will ultimately scatter back to the original position.

#### 2.2.3.1 Diffusion

Diffusion is a phenomenon which describes the motion of carriers caused by a concentration gradient. The movement of carriers starts from the region with a higher concentration and propagates toward the region with lower concentration until the carriers are evenly spread across both regions. For example, when a p-doped material is connected to a n-doped material, the electrons in n-type region (high electron concentration) diffuse towards the p-type region (low electron concentration).

#### 2.2.3.2 Drift

Drift is a phenomenon which describes the motion of carriers caused by a potential gradient e.g. the presence of an electric field. The movement of carriers starts from region with higher potential to the region with lower potential. Electrons accelerated to the opposite direction of the electric field, whereas holes are accelerated to the same direction of the electric field. Namely, if the direction of the electric field is towards the right (+ → -), electrons will drift towards left (←) because the left region is less negative compared to the right.

#### 2.2.3.3 Carrier lifetime

The purpose of using semiconductor material with a bandgap in SC is to prevent the excited electrons from recombining at a fast rate and, hence, to increase the possibility for exploiting the excited electrons. The average amount of time for which the excited

electrons remain in CB before they recombine is denoted as the lifetime  $\tau$  of electrons, as given in Equation 2.3 [1]:

$$\tau = \frac{\Delta n}{R} \quad \text{Equation 2.3}$$

It is dependent on the number of generated electrons  $\Delta n$  and the rate of recombination  $R$ . An alternative expression which expands  $R$  into the three different types of recombination:

$$\tau_{rad} = \frac{1}{B_{rad}N_a}, \quad \tau_{Aug} = \frac{1}{A_n N_d^2}, \quad \tau_{SRH} = \frac{1}{B_n N_t} \quad \text{Equation 2.4}$$

Where  $B_{rad}$ ,  $A_n$  and  $B_n$  are recombination coefficients which are dependent on the material properties;  $N_a$ ,  $N_d$  and  $N_t$  are concentration of holes, electrons and trap states, respectively.

SC engineers should design this lifetime to be as long as possible so that the probability of carrier collection is greater.

#### 2.2.3.4 Diffusion length

The other parameter associated with recombination is the diffusion length ( $L$ ), describing the average distance that the carriers can travel before they recombine. The diffusion length equation is correlated to carrier lifetime via the following equation [1]:

$$L = \sqrt{D\tau} \quad \text{Equation 2.5}$$

Where  $D$  represents the diffusivity, which is a measure of diffusion, that describes the movement of particles from high concentration to low concentration.

It is important to distinguish the difference between the diffusion length and the physical length (or thickness) of the device. The long diffusion length is beneficial to increase the collection probability. However, if the thickness of the n-type material is thicker than the diffusion length, the photo-generated electrons cannot reach the negative terminal and will be lost in the process. The diffusion length for a silicon SC is typically 100-300  $\mu\text{m}$  and,

thereby, the thickness of the devices is 300  $\mu\text{m}$ . This can also be explained in terms of carrier mobility. Electrons are more mobile compared to holes, hence, they diffuse a longer distance. As a result, the thickness of n-type region is thicker compared to the p-type region.

## 2.2.4 PN junction

PN junction is the building block of light emitting diode (LED), LASER, photodetector and SC devices. Its function is differentiated by the operating modes i.e. LED and Laser in forward bias mode, photodetector and SC in reverse bias mode.

### 2.2.4.1 Formation of PN junction

A pn-junction is formed by connecting two oppositely doped materials, as shown in Figure 2.9. Due to the high electron (hole) concentration in n-type (p-type) material, the majority carriers will diffuse into the oppositely charged region leaving behind their immobile ion cores. The positively and negatively charged ion cores in n-type and p-type materials, respectively, build an internal electric field. This built-in electric field ( $E$ ) sweeps any charged carriers aside and enable charge separation. Therefore, the region in which the carriers are swept away by the built-in electric field is called the depletion region.

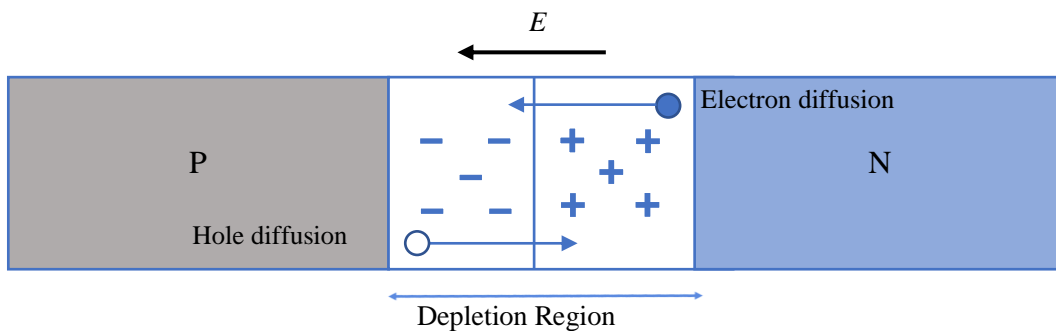


Figure 2.9 Schematic of a PN junction illustrating carrier diffusion and depletion

The width of depletion region and the strength of the built-in electric field are dependent on the level of doping or density of the dopants. For example, a higher doping level results in stronger electric field and shorter width of depletion region. Stronger electric field separates the photo-generated carriers more effectively, which is advantageous for less recombination. However, the effective absorption area is smaller due to shortened depletion region, and, hence, the absorption of light becomes less efficient.

#### 2.2.4.2 PN junction at equilibrium

The extent to which the built-in electric field is accumulated depends on two factors: diffusion and drift. When the diffusion of majority carriers is counter-balanced by the drift of minority carriers, the junction is at equilibrium, which implies that the net current is zero; else it is under bias.

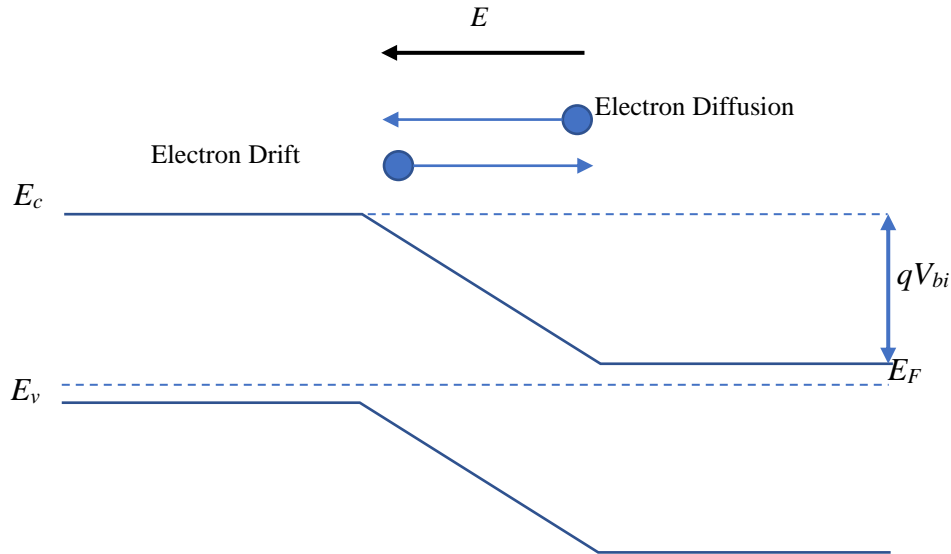


Figure 2.10 PN junction at equilibrium with balanced drift and diffusion

Figure 2.10 shows the simplified band diagram of a pn-junction at equilibrium where the minority electron drift is equal to the majority electron diffusion. The  $E_F$  is equalised across the whole junction due to the band bending effect by the built-in electric field induced potential difference ( $V_{bi}$ ).

#### 2.2.4.3 PN junction under bias

When an external voltage is applied to the pn-junction, the junction is under a bias. There are two so-called “modes” of bias: forward bias mode and reverse bias mode. They differ in the promotion of one phenomenon to oppose the other. In the forward bias, the majority carrier diffusion is promoted so that large current can flow across the junction. In the

reverse bias, the majority carrier diffusion is demoted, providing the large resistance against the current flow.

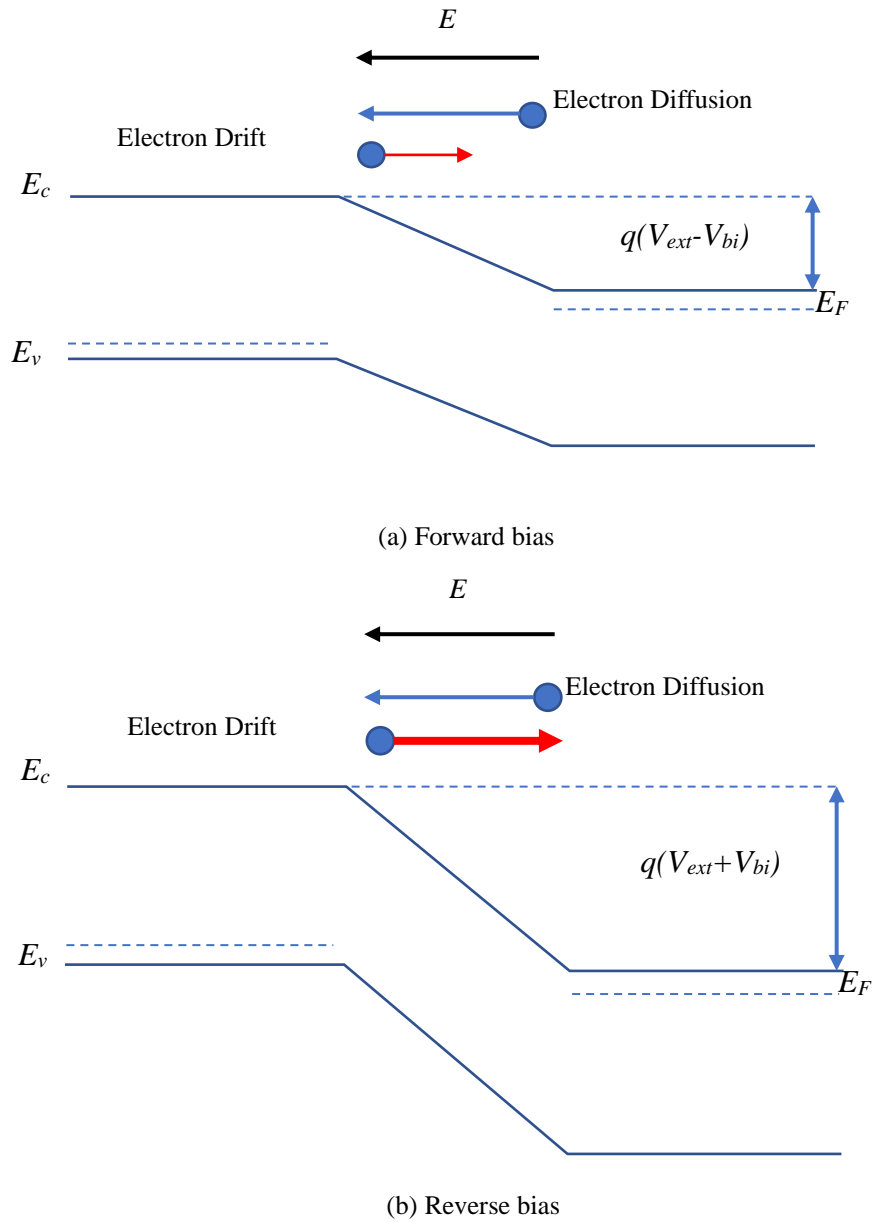


Figure 2.11 PN junction under (a) forward bias mode and (b) reverse bias mode

Under forward bias, the external voltage ( $V_{ext}$ ) applies a force which works against  $V_{bi}$ , reducing the strength of the built-in electric field, which, in effect, favours the majority carrier diffusion. Figure 2.11(a) illustrates the reduction of built-in potential difference caused by the external force:  $q(V_{ext}-V_{bi})$ . Consequently the electric field which was accumulated to equalise both diffusion and drift becomes weaker. A weaker electric field results in less minority carrier drift (short red arrow) and relatively more majority carrier diffusion. The Fermi level which was equal at equilibrium has now been split: raised in n-type region due to more electron diffusion and lowered in p-type region due to hole diffusion. Overall, large amount of current flow is generated.

Under reverse bias, in Figure 2.11(b), the external voltage strengthens the built-in electric field and, therefore, minority carrier drift is promoted (red thick arrow). Majority carrier diffusion is relatively impeded so no current flow is contributed. The only source of current flow is produced by the minority carrier drift, but, the amount of current flow is very limited due to the small population of minority carriers. Fermi level is split in the opposite manner:  $E_F$  lowered in n-type region due to less electron diffusion and raised in p-type region due to less hole diffusion.

## 2.3 Solar cell operation

SC can harness energy from sunlight and convert it into electrical energy to power external devices [1]. The operation of SC requires two essential features: photon absorption and charge separation. The photon absorption captures the incident light which is used to excite electrons into CB. Absorption is achieved using the semiconductor materials with bandgaps between 0.5 eV (2500 nm) to 3 eV (400 nm). The charge separation drives the excited electrons towards the terminals and an external load. Charge separation is achieved by the pn-junction from doping materials with p- and n- type dopants. Both features should be satisfied simultaneously otherwise the device is only an ideal light absorbing material or pn-junction in reverse bias mode [1].

### 2.3.1 PN junction solar cell operation

A conventional GaAs SC with a bandgap of 1.42 eV absorbs the spectrum up to 870 nm at room temperature. The material is doped with Be and Si as respective p- and n-type dopants and connected together to form the pn-junction.

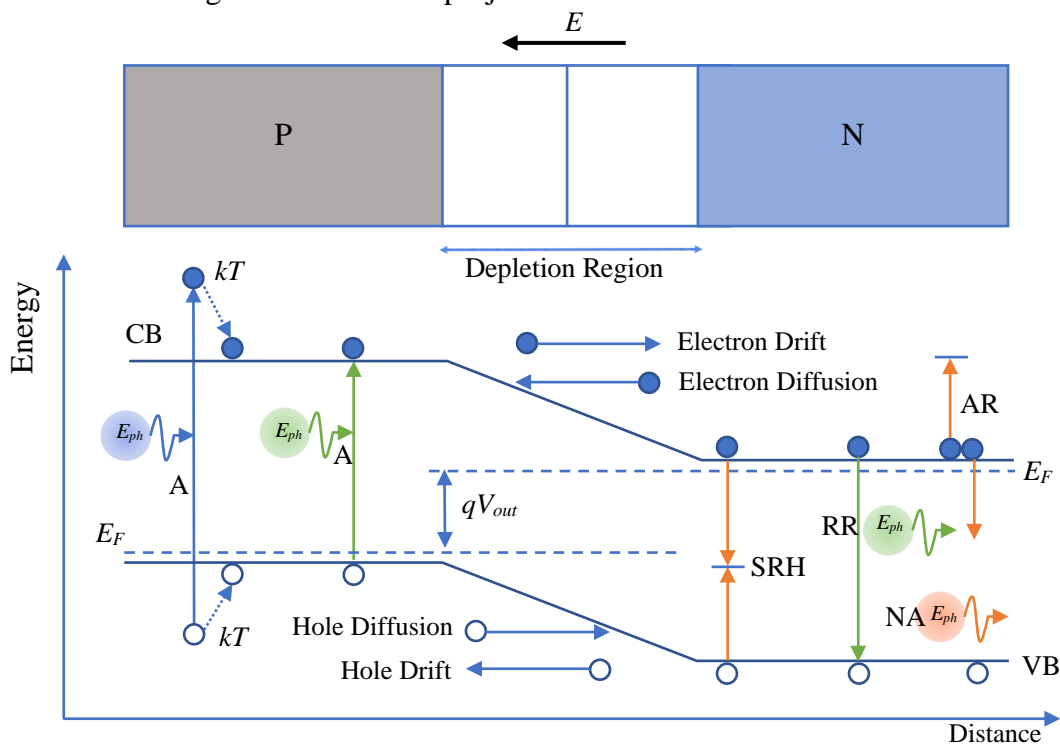


Figure 2.12 Schematic of a PN junction solar cell including all operating mechanisms:

A (Absorption), SRH (Shockley-Read Hall), RR (Radiative recombination), AR (Auger recombination), NA (No Absorption)

Figure 2.12 shows a comprehensive schematic including all operating mechanisms. To summarise and recap:

When the green photon with 1.42 eV energy travels through the GaAs SC, the photon is absorbed (A), and subsequently an electron in VB gains this amount of energy to leap across the bandgap and enters the CB. When the blue photon with 1.7 eV encounters the SC, the photon is also absorbed to generate an electron-hole pair with additional thermal energy ( $kT$ ). However, when the orange photon with 1.2 eV energy passes through the SC, no interaction occurs, and thus the photon is not absorbed (NA).

When the excited electron enters CB, it experiences a drift force exerted by the built-in electric field ( $E$ ) and is guided towards the n-type region. Holes drift and diffuse in directions opposite to the direction of electrons.

This charge separation process is featured by the asymmetric pn-junction that only permits the electrons and holes to travel towards the n-type and p-type region, respectively.

Once the electrons drift out of the depletion region into the n-type region, they become majority carriers. Then, they drift towards the negative terminal in order to be extracted for external use. During this phase, electrons are susceptible to radiative, Shockley-Read Hall and Auger recombinations (RR, SRH and AR).

### 2.3.2 Ideal solar cell conditions

Ideally, a perfect SC exhibits an optimum bandgap, full absorption of light, complete carrier separation and lossless carrier transport.

Semiconductor materials have a bandgap ranged from 0.5 eV to 3 eV. Solar spectrum has a wider spread, but the highest intensity lies in the visible light region 400 nm to 700 nm (1.77 eV to 3.1 eV). GaAs and InP have a bandgap of 1.42 eV and 1.35 eV, respectively, which covers the absorption of infra-red region as well as the visible light region, and hence they have the optimum bandgaps.

Full absorption in SC refers to the absorption of the photons with energy greater or equal to the bandgap, which is different from absorption of the whole solar spectrum. It can be achieved for all semiconductor materials by increasing the optical depth or the material thickness. Indirect bandgap material such as Si is able to achieve full absorption through 300  $\mu\text{m}$ -thick absorption layer. For the direct bandgap materials such as GaAs, on the other hand, only 3  $\mu\text{m}$ -thick intrinsic region is needed to obtain full absorption.

Complete carrier separation requires the asymmetric junction to have an infinite strong built-in electric field in order to instantly sweep all excited carriers outside the depletion region, leaving no possibility for recombinations. Strong electric field can be achieved by increasing the doping levels of pn-junction.

Lossless carrier transport ensures the separated carriers diffuse through the material without obstruction. It demands the material has no defects or impurities lest particle collisions occur. Lossless carrier transport also means that carriers have infinite long lifetimes and diffusion length.

### 2.3.3 Practical limitations

There are limits and contradictions for the design and manufacturing process of SCs. For example, strong absorption leads to strong recombinations. Although GaAs and InP have direct bandgaps and high absorption coefficients, they suffer from recombinations as much as they benefit from absorption.

Increasing absorption through thickening of the material depth has negative effects such as increasing the distance carriers required to diffuse which leads to losses during the carrier transport process. In addition, thicker materials are heavier, resulting in restriction to the usage of solar panels. Si solar panels are mostly situated on roof tops, solar cell fields *etc.* GaAs solar panels are integrated onto spaceships and satellites because for space applications, lighter weight has higher priority.

The side effect of heavy doping is the introduction of defect states which act as recombination centres or trap states, and, thus, promote SRH recombination. In addition, it reduces the effective bandgap by adding tails to the CB and VB. For materials with less mature growth techniques, dopant levels are closely monitored to prevent the heavy doping effects. GaAs materials have the highest doping level of  $10^{18} \text{ cm}^{-3}$  whereas Si materials can be doped at  $10^{19} \text{ cm}^{-3}$ .

The negative impact of achieving lossless carrier transport is to oppose full absorption and strong electric field. Therefore, the objective of SC design is to find the optimum compromise between all the factors.

### 2.3.4 Shockley Queisser limit

In 1961, Shockley and Queisser published their work on finding the optimum compromise between the factors (radiative and non-radiative recombinations, spectrum losses, carrier mobilities, parasitic resistances *etc.*) and established a theoretical maximum efficiency of 33.1% for the best SC [3]. In the publication, the authors compared the importance of finding the SC theoretical upper limit to the second law of thermodynamics. Without knowing the maximum value, researchers would be directionless with regard to finding the most effective path to improve the system. The authors described factors such as series resistance and reflection losses as the friction in a power plant; the ultimate factor which limits the SC performance is the radiative recombination mechanism. In this regard, the authors presented their theoretical calculation taking only the radiative recombination mechanism into account, and results indicated that the maximum efficiency lies at 33.1% which corresponds to materials with a bandgap of 1.34 eV.

## 2.4 References

- [1] J. Nelson, *The Physics of Solar Cells*. Imperial College Press, London, 2003. ISBN-13 978-1-86094-3492
- [2] Honsberg C. and Bowden S., “Absorption Coefficient,” PVCDROM – 3. PN Junction. <http://www.pveducation.org/pvcdrom/absorption-coefficient> accessed on 29 Jan 2022.
- [3] W. Shockley and H. J. Queisser, “Detailed balance limit of efficiency of p-n junction solar cells,” *J. Appl. Phys.*, vol. 32, no. 3, pp. 510–519, Mar. 1961

## Chapter 3 Experimental methods

*This chapter details the experimental procedures required to complete the research. It consists of three stages: sample growth, device fabrication and characterisation.*

*First, the samples were grown with the designed solar cell (SC) structure on the substrate by using molecular beam epitaxy (MBE). Second, the grown samples are taken into the cleanroom for solar cell device fabrication. P-type and n-type metal contacts are deposited onto sample to form ohmic contacts. Third, the fabricated device is characterised to determine performances. Atomic force microscopy (AFM), scanning electron microscopy (SEM) and photoluminescence (PL) measure the material quality and morphology. Current density versus voltage (J-V) characterization and external quantum efficiency (EQE) examine the solar cell efficiency.*

### 3.1 Sample growth

Epitaxial structure is vertically stacking layers of atoms or molecules on top of each other in an orderly manner. There are two methods to achieve this: physical and chemical growth, e.g. molecular beam epitaxy (MBE) and metal-organic vapour-phase epitaxy (MOVPE), respectively. The MBE, which offers extremely high precision and accuracy, is most likely to form the designed structure [1], [2]. MOVPE, on the other hand, has moderate precision and accuracy but a faster growth rate. Metal-organic chemical vapour deposition (MOCVD) which is one type of MOVPE has a growth rate of  $\sim 100$  nm per minute, and MBE has  $\sim 10$  nm per minute [3]. For nano device projects such as QDSCs or QD lasers, precision is the top-most priority and, hence, the MBE method is adopted for sample growth.

#### 3.1.1 Molecular beam epitaxial growth

The main reason that MBE achieves extreme high growth precision (thickness control of 0.5 nm) is due to the ultra-high vacuum (UHV) condition ( $\sim 10^{-11}$  Torr). Under this condition, the growth chamber is so clean that only the particles ejected from the effusion

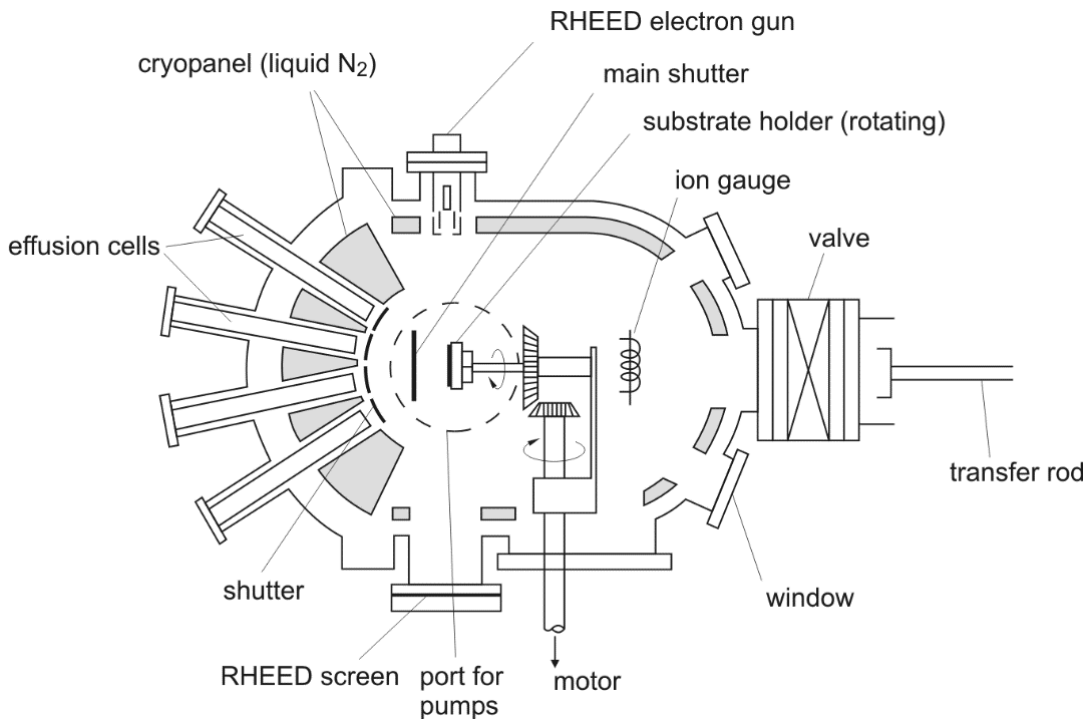


Figure 3.1 Schematic diagram of an MBE growth chamber

cells are present and the path towards the substrate is not obstructed by any impurity. Hence, the material composition is extremely pure and the grown structure is precise.

Figure 3.1 presents the schematic diagram of an MBE growth chamber. For QDSC projects, all samples are grown by a group III-V MBE which has a material base of Boron (B), Aluminium (Al), Gallium (Ga), Indium (In), Arsenic (As), Antimony (Sb) and solid source Phosphorous (P). In addition, there are two more source materials, Beryllium (Be) and Silicon (Si), for doping. The high purity source materials are stored in the effusion cells. The chamber is maintained under an UHV environment with the aid of a liquid nitrogen cryopanel. Substrate holder can rotate  $360^\circ$  to ensure uniform deposition. Shutters are used to control the flux rate of the molecular beam. The growth modes and deposition rate are monitored by the reflection high energy electron diffraction (RHEED) system consisting of a RHEED gun and a screen. *In situ* monitoring system is another advantage of MBE over MOVPE, which allows immediate feedback of the deposition rate so that the flux rate can be constantly adjusted.

### 3.1.2 MBE growth modes

Figure 3.2 illustrates three modes of thin film epitaxial growth: (a) Volmer—Weber (VW), (b) Frank—van der Merwe (FM) and (c) Stranski—Krastanov (SK) [4].

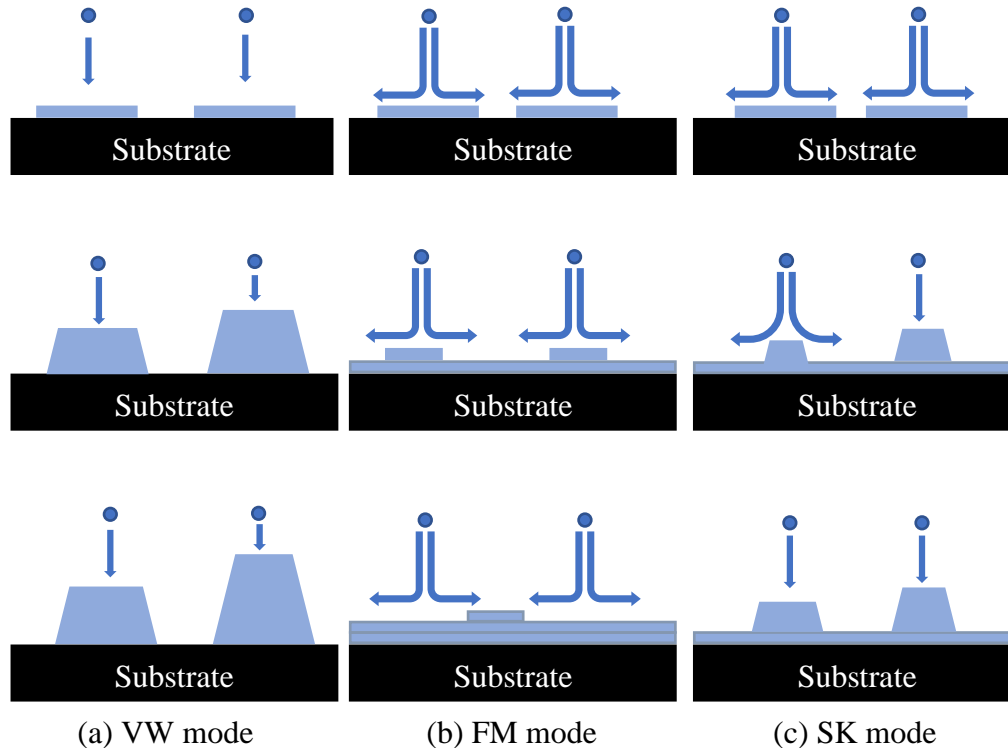


Figure 3.2 Three MBE growth modes: (a) VW mode, (b) FM mode and (c) SK mode

Under VW growth mode, 3-D islands are more likely to form due to the short migration length of the adatoms. Since the atoms injected onto the sample surface have less energy to travel, they cluster with another recently injected atom. As a result, islands are formed. FM growth mode, on the contrary, has long migration length. Therefore, the adatoms tend to spread out and cover the surface, resulting in a 2-D layer growth. SK growth is a compromise between the two modes and is commonly used to grow the QDs. SK growth starts off following the FM growth by forming 2-D layers of adatoms. However, when a critical thickness is reached, the growth mode transitions toward VW and begins to form islands.

### 3.1.3 Self-assembled quantum dots

InAs QDs grown on GaAs substrate is a demonstration of SK mode growth [5]. Due to InAs/GaAs lattice mismatch, the initially tolerable 2-D layer growth is soon undermined by the accumulated strain. When the accumulated strain overtakes surface tension, the critical thickness is reached and further growth results in forming 3-D islands instead of 2-D layers [6]. The QD growth under SK mode is described as “self-assembled quantum dots”.

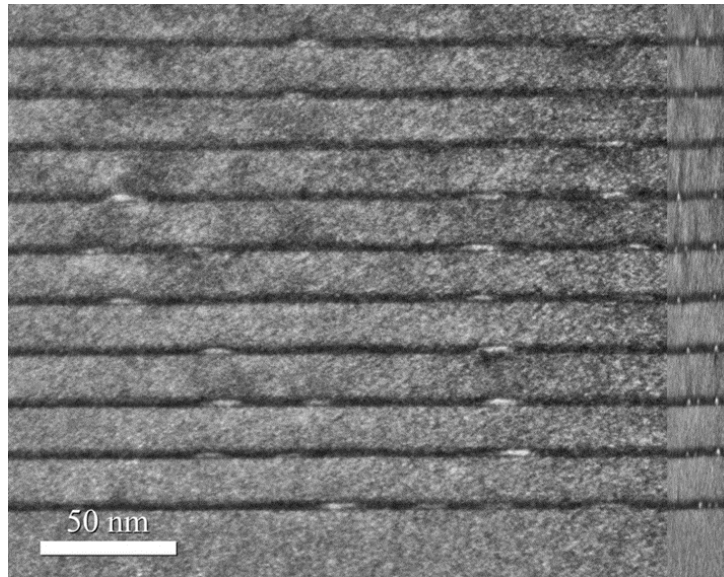


Figure 3.3 TEM image of InAs QDs grown under SK mode

Figure 3.3 illustrates a transmission electron microscopy (TEM) image of InAs QDs which are grown by MBE under SK mode. The dark grey layers are the 2-D wetting layers and the white lens-like islands are the self-assembled QDs.

### 3.2 Device fabrication

Post growth, the samples are taken into the London Centre for Nanotechnology (LCN) cleanroom. The as-grown SC wafers are fabricated into SC devices through patterning, etching, surface treatment and metallisation.

The dexterity of fabrication skill has an impact on the device performance. More advanced and complicated processes require multiple steps of photolithography, etching, thermal evaporation and sputtering which result in a higher metal contact quality and SC fill factors. There are three established recipes for our SC fabrication (created by Dr D. Kim and Dr A. Onno): top-bottom contact with shadow-masks, top-bottom contact with photo-masks and top-top contact with photo-masks; ranked in terms of complexity. The average fill factors are 60 %, 80 % and 80 %, respectively. Photos of the fabricated SCs are shown in Figure 3.4. The photo on the left used the top-bottom recipes, in which the n-type metal contact is on the backside of the sample. The photo on the right which uses top-top contact method shows the n-type metal contact with mesa shaped outline.



Figure 3.4 Photos of fabricated QDSCs with top-bottom contact on the left and top-top contact on the right

### 3.2.1 General process

#### 3.2.1.1 Top-bottom contact with shadow-masks

Top-bottom contact with shadow-masks recipe is the least complex recipe. Figure 3.5 illustrates the cross-sectional diagrams of QDSC before and after fabrication. The term “top-bottom” refers to the position of contacts which are on front-surface side and the back-substrate side of the sample, respectively. The metals deposited on the bottom of n-type material interface consisted of 10 nm Ni/ 100 nm AuGe (88:12)/ 30 nm Ni/ 200 nm Au. 200 nm AuZn (95:5) is thermally deposited on p-type material interface through a shadow mask with SC grid patterns.

Fabrication sequence:

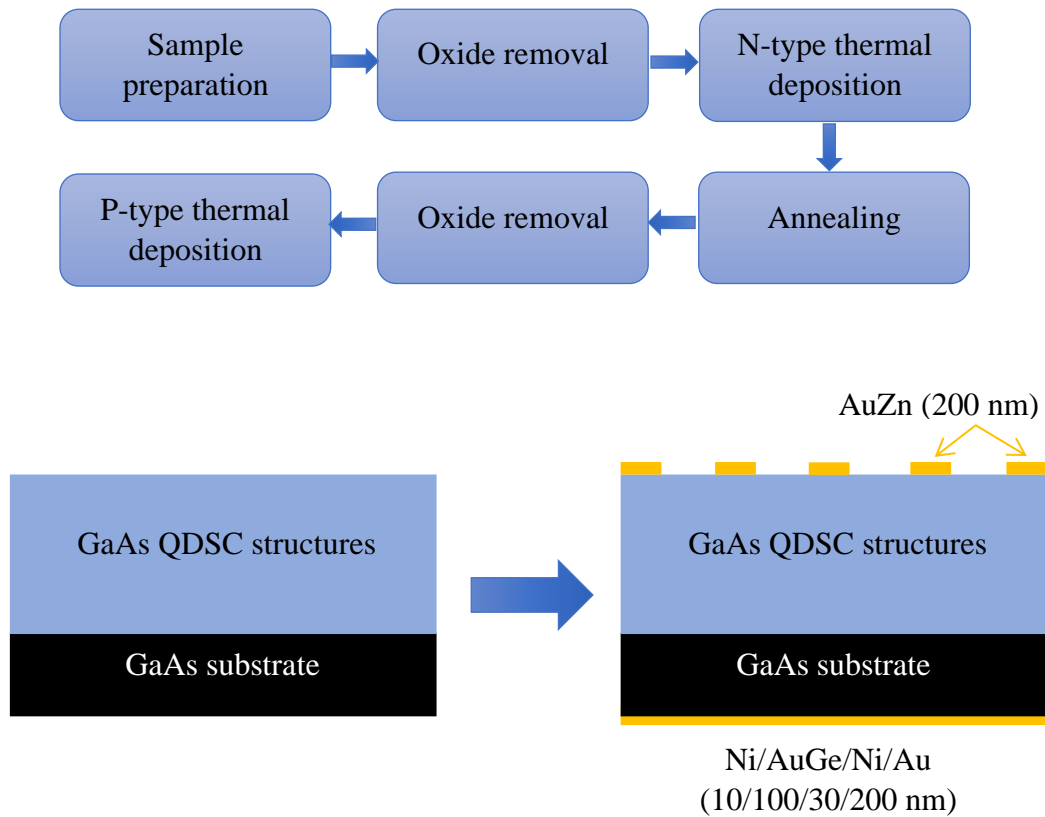


Figure 3.5 Cross-sectional diagrams of QDSC structure before and after top-bottom contact with shadow-masks

### 3.2.1.2 Top-bottom contact with photo-masks

Top-bottom contact with photo-masks implies the application of photolithography, which is more complex than the previous recipe. Completed device structure is displayed in Figure 3.6. The n-type contact procedures are identical. On the other hand, for the p-type contact, the typical photolithography was employed to define a pattern, and the p-type contact of 20 nm Ti/ 50 nm Pt/400 nm Au was sputtered. Additional lift-off and wet-etch processes are required to finish the fabrication.

Fabrication sequence:

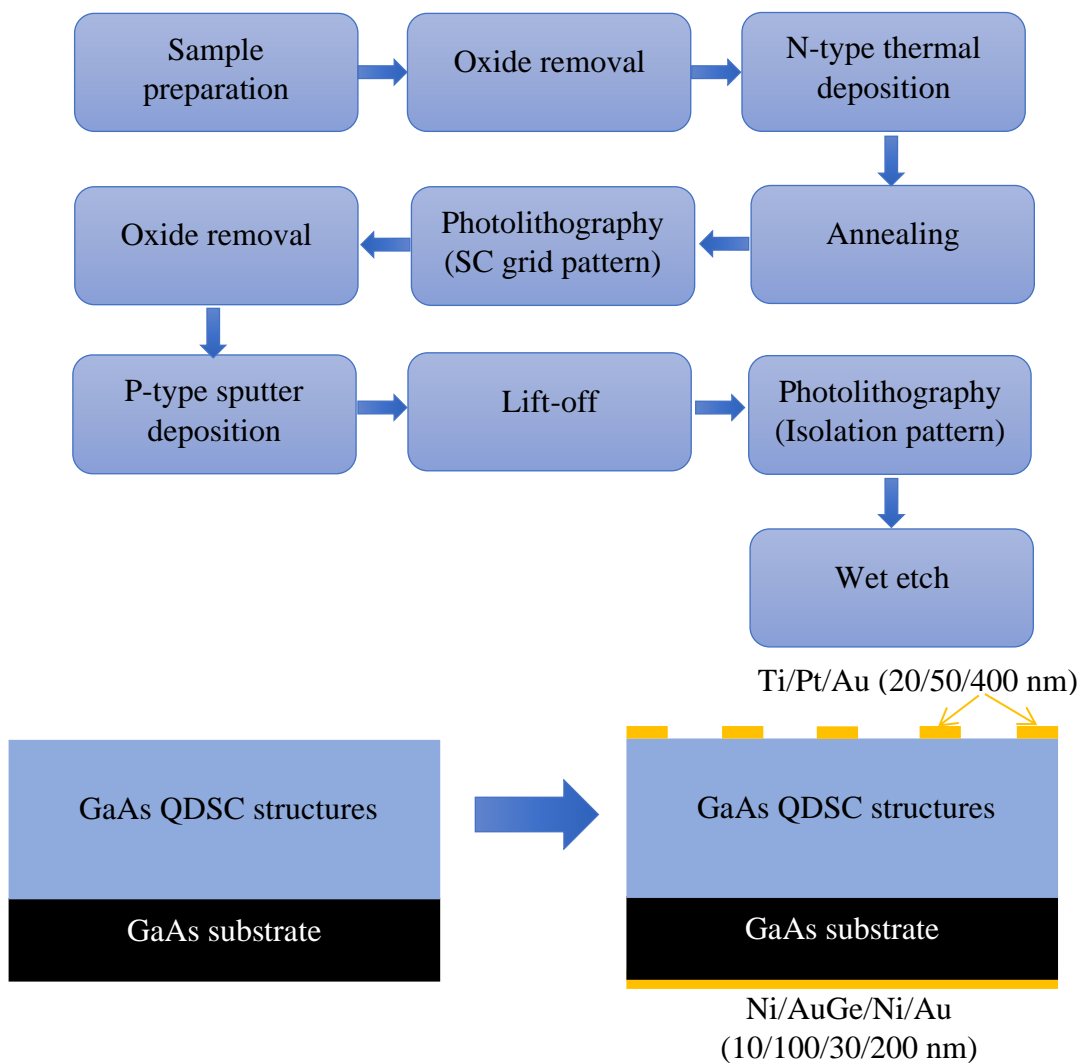


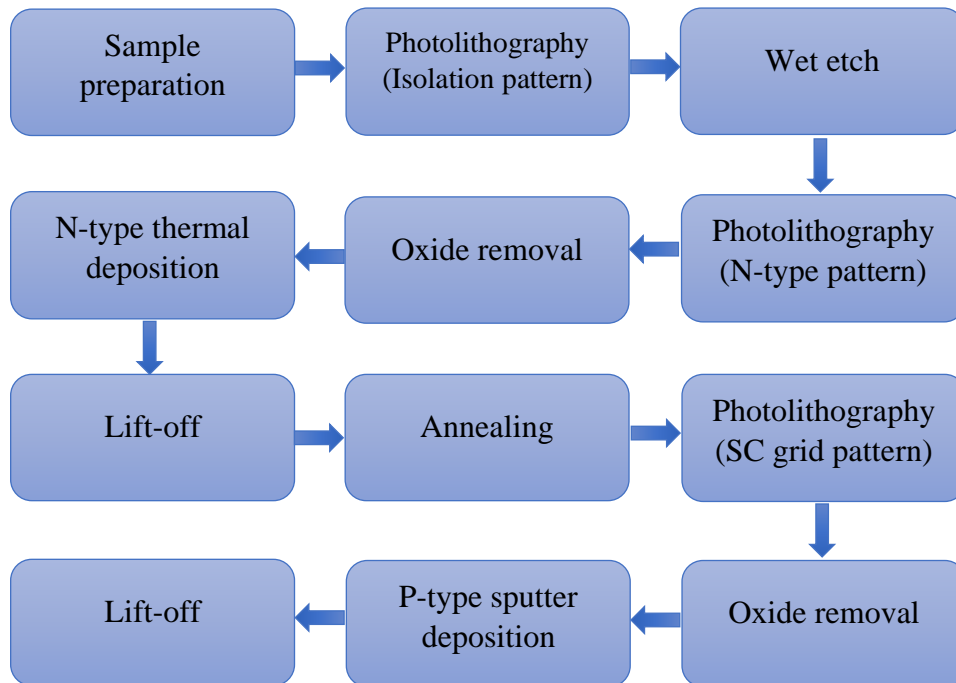
Figure 3.6 Cross-sectional diagrams of QDSC structure before and after top-bottom contact with photo-masks

### 3.2.1.3 Top-top contact with photo-masks

Top-top contact with photo-masks recipe requires additional photolithography, lift-off and wet-etch steps. This configuration is commonly applied to GaAs SC samples grown on Si substrates, as shown in Figure 3.7. Due to lattice mismatch between GaAs and Si, buffer layers are required to compensate the strain [7]. Applying metal contact at the bottom of the Si substrate causes electron extraction through the defective buffer layers which may result in loss of electrons [8]. The solution is to bypass the defected layers by depositing the contacts above the buffer layer i.e. relocating the n-type contact from bottom of the substrate to the surface of the sample (hence the name “top-top contact”).

Fabrication sequence begins with mesa etching, followed by n-type contact thermal evaporation and completed with p-type contact sputtering. Contact materials are the same as previous recipe.

Fabrication sequence:



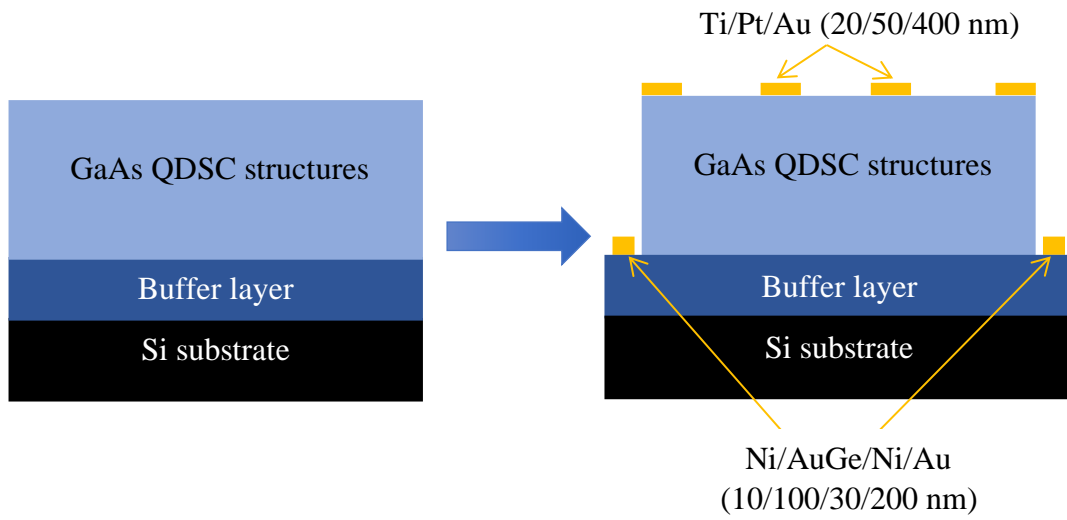


Figure 3.7 Cross-sectional diagrams of QDSC structure before and after top-top contact with photo-masks

### 3.2.2 Sample preparation

All 3-inch wafers are manually cleaved into quarter-wafers by a diamond-tip scribe as shown in Figure 3.8. The cleaved samples are cleaned with acetone and isopropyl alcohol (IPA) solutions for 5 minutes or longer, respectively.

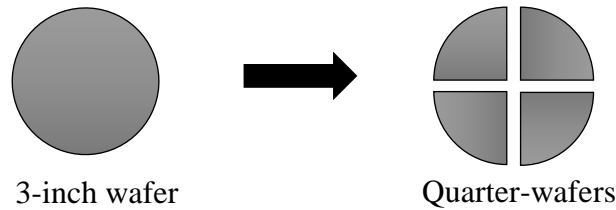


Figure 3.8 Sample wafer cleaved into quarter-wafers

### 3.2.3 Oxide removal

Prior to metallisation, an oxide removal or deoxidation step is performed because the presence of surface oxide has detrimental effects on the metallisation. The native oxide on the surface can increase the parasitic resistance and prevent ohmic contact formation. Also, the surface oxide may result in a roughened surface, which induces the unwanted metal peel-off during the lift-off process.

To remove the native oxide of wafers, all samples were treated with diluted ammonia solution ( $\text{NH}_3 : \text{H}_2\text{O} = 1 : 19$ ) for 40 seconds and subsequently dried with nitrogen ( $\text{N}_2$ ) gun.

### 3.2.4 Photolithography

The photolithography process consists of five steps. The purpose of photolithography is to print device patterns on the sample for further processing such as metal deposition and etching. Compared to the shadow-mask method, photolithography offers more accurate pattern shape which is essential for nano-devices. However, the photolithography procedure involves the deposition of light-sensitive photoresists onto sample surface. This may have a negative impact, particularly to SC devices, on the device performance. Any uncleaned photoresist residual can hinder the device absorption of sunlight.

#### 3.2.4.1 Pre-bake

Pre-bake or dehydration process aims to remove the remaining solutions on the surface so that the photoresists can be uniformly spin-coated. The procedure is to place the samples on the hot plate at 190 °C for 10 minutes after the samples are cleaned. Incomplete procedure may result in inter-mixing of photoresist and cleaning solutions, which causes blurring in the coated photoresist.

#### 3.2.4.2 Spin-coating

There are two types of photoresists: positive and negative. For the positive photoresist, the area on which the UV light is exposed is removed after developing. On the other hand, for the negative photoresist, the UV-exposed area is strengthened so that the unexposed area is removed after developing.

In this work, two different photoresists, S1818 and LOR 10B, were used for fabrication. Both are positive photoresists for which the exposed area is removed after developing process. The photoresists are dropped onto the sample by a pipette, and then the sample is rotated at 4000 rpm for 30 seconds. The dropped photoresists should cover the whole sample to avoid uneven layers of photoresist.

For samples requiring lift-off process, bilayer photoresist comprised of LOR 10B and S1818 photoresist is used as shown in Figure 3.9.

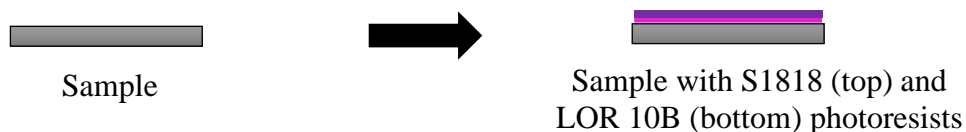


Figure 3.9 Spin-coated sample with S1818 and LOR 10B photoresists

#### 3.2.4.3 Soft bake

Baking crystallises the spin-coated photoresists. S1818 photoresist requires 90 seconds of baking on the hot plate at 115 °C, and LOR 10B requires 10 minutes at 190 °C. The target thicknesses of the S1818 and LOR10B are 1.8 µm and 0.9 µm, respectively [9], [10]. In

practice, the thickness detected by profile-measuring devices can be slightly thicker, ~1.9  $\mu\text{m}$ . The mismatch may be caused by expired photoresist impurities or slower spin-coater rpm.

#### 3.2.4.4 Alignment and exposure

Aligning is to imprint the desired pattern onto the sample with photoresists and it requires extreme precision. Any mismatch may result in faulty metal deposition or mesa etching and consequently the device will be irreversibly short-circuited. However, if the mismatch has been detected by microscope before metallisation or etching, this faulty pattern can be removed by acetone or remover 1165 solution.

Photoresists need to be exposed under UV light once the pattern and the sample are correctly aligned, illustrated in Figure 3.10. The exposure time is between 2.7 s to 3.2 s depending on the thickness of the photoresist. In this work, single layer (S1818) and bilayer (S1818 and LOR10B) require 2.7 s and 3.2 s, respectively.

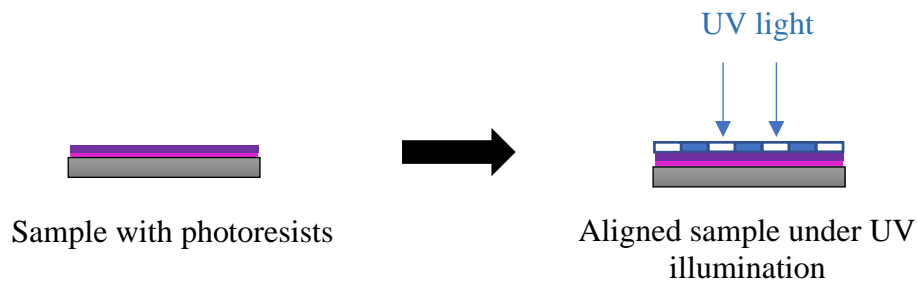


Figure 3.10 Sample under UV exposure

#### 3.2.4.5 Developing

Developing is the final step of photolithography, which dissolves the positive photoresist that were exposed under UV light and, hence, form the desired pattern. Once the photoresists undergo UV exposure, the exposed area becomes less rigid. In this work, the sample is immersed into MF-319 developer solution for 50 s to dissolve the softened photoresists. Subsequently, the sample is dipped into de-ionised water for 20 s to stop further development process.

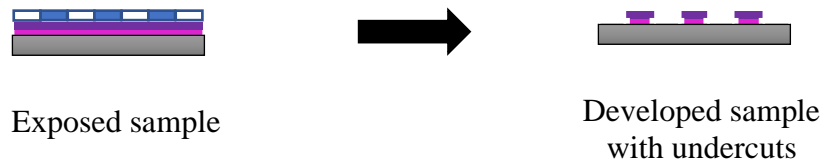


Figure 3.11 Developed sample

It has been mentioned that the samples which require lift-off process has an extra LOR 10B photoresist layer. During development, this light-insensitive layer interacts with the developer solution more vigorously than S1818. As a result, top S1818 layer would be less developed than bottom LOR 10B layer and form undercuts as shown in Figure 3.11. These undercuts will increase the rate of lift-off process. More importantly, the undercut can avoid the metal peel-off issue during lift-off process. Without the undercut, the metals can be deposited on the sidewall of photoresists and thus connected to the metal on the surface, resulting in poor edge of metallisation after lift-off process.

### 3.2.5 Metal contact deposition

Metal contact deposition or metallisation is a process that deposits metal or alloy onto the surface of the sample, as shown in Figure 3.12. The purpose is to form an electron-rich ohmic contact so that the photogenerated electrons can be extracted and passed onto external devices. The choice of metal sources, therefore, becomes crucial; their workfunction must be matched with the sample's electron affinity, otherwise there will be an energy barrier at the interface which limits electron extraction. For GaAs samples, the n-type surface is matched by Ni, AuGe (88:12) and Au; the p-type surface is matched by AuZn (95:5) or Ti, Pt and Au.

Two methods are used to perform metallisation, thermal evaporation and magnetron sputtering. Thermal evaporation deposits metal on the samples by heating and evaporating the sources. Sputtering utilises magnetic force to accelerate the charged particles or ions provided by plasma towards the target source, and then the target source material is deposited on the samples. Sputtering can deposit very high melting point metals such as Ti and Pt, but thermal evaporators cannot melt and evaporate this type of metal.

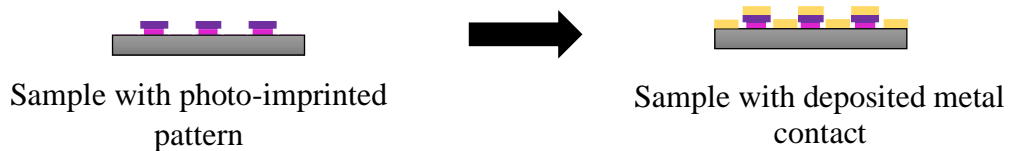


Figure 3.12 Metallised sample

### 3.2.6 Lift-off

Lift-off process is carried out after metallisation. It removes the unwanted metal patterns by dissolving the photoresists underneath, thus, leaving behind the desired metal pattern with a clean surface, as shown in Figure 3.13. The procedure is to immerse the metallised sample into Remover 1165 solution at 65 °C. The process may take up to 2 hours to lift-off the very detailed metal pattern e.g. the overlay indicators. Ultrasonication can increase the rate of lift-off. However, it can only be applied to large patterns with adhesive contacts.

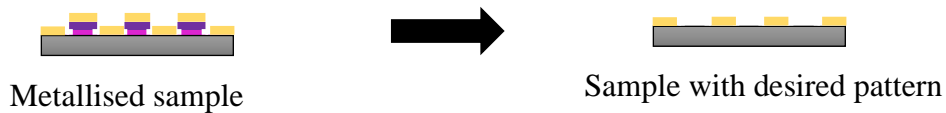


Figure 3.13 Sample with desired contact pattern

N-type mesa-like metal contacts can use ultrasonication, but the p-type grid-like metal contacts cannot.

### 3.2.7 Wet etching

Etching is an irreversible process that removes certain layers of the sample. There are two methods to remove the sample layers: wet etch or dry etch. Wet etch uses liquid chemicals to dissolve the sample material. Dry etch, or ion-milling, physically removes the sample layers by bombarding the surface with ions.

Here, the purpose of etching is to create mesas that isolate individual SC devices and also to reach the contacting layer for n-type metal deposition, as illustrated in Figure 3.14. The sample layers are mainly composed of GaAs materials and the depth required to etch is at least 3000 nm; hence, the wet etch method is adopted.

The etching process is carried out after imprinting the mesa patterns via photolithography and its procedure is to immerse the sample with mesa patterns into the selective etchant solution ( $\text{H}_2\text{SO}_4 : \text{H}_2\text{O}_2 : \text{H}_2\text{O}$  at 1 : 10 : 80 ratio) which specifically targets GaAs materials. The etch rate is between 600 to 800 nm per min; therefore, the time required to etch 3000 nm is between 4 to 5 minutes. The photoresist is then cleaned using acetone and IPA solution.

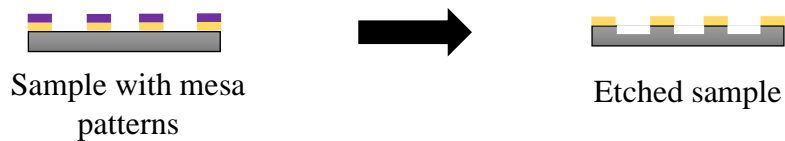


Figure 3.14 Wet-etched sample

### 3.2.8 Thermal annealing

In order to forge an electron-rich ohmic contact, thermal annealing is performed after N-type metallisation [11]. Samples placed into the rapid thermal processing (RTP) machine are heated up to 390 °C then held at that temperature for 60 s. The purpose of annealing is to intermix the Ni-AuGe-Ni interfaces so that the alloy bond becomes stronger, resulting in better ohmic formation.

### 3.3 Solar cell characterisation

Characterisation process can be carried out post sample growth or device fabrication. Atomic force microscopy, scanning electron microscopy and photo-luminescence are used to examine the material morphology and purity of the as-grown wafers. External quantum efficiency and current density versus voltage characterisation are carried out to examine the performances of SC device.

#### 3.3.1 Atomic force microscopy (AFM)

Atomic force microscopy (AFM) examines the surface morphology of the sample. Its operation principle is demonstrated in Figure 3.15. The cantilever with a small tip is placed above the sample. A laser beam is focused onto the tip and reflected back to a photodetector. As the cantilever scans through the sample, the tip will be repelled by the atomic force of the uneven QDs, causing oscillations in the reflected signal. This reflected signal is recorded to print out the surface morphology of the sample, as shown in Figure 3.16.

AFM is used to observe the QD qualities. The size or shape of the QD can be measured to

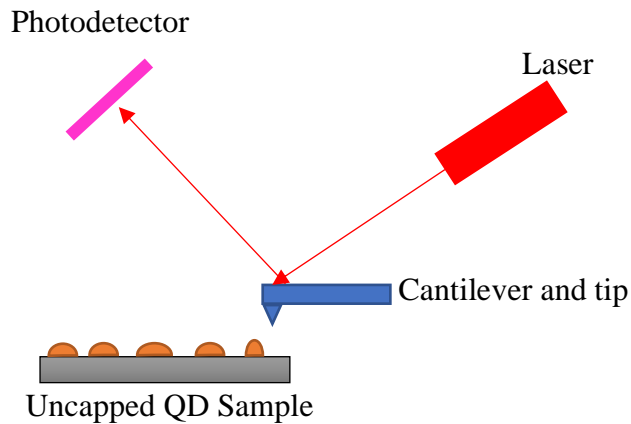


Figure 3.15 AFM operation mechanism

calculate the bandgap energy and, hence, determine the intermediate band position. The density of QDs can be estimated by counting the number of dots per area (Figure 3.16 a). Defect density can also be found with the same method. The uniformity of QDs can be visualised using the 3D imaging function (Figure 3.16 b).

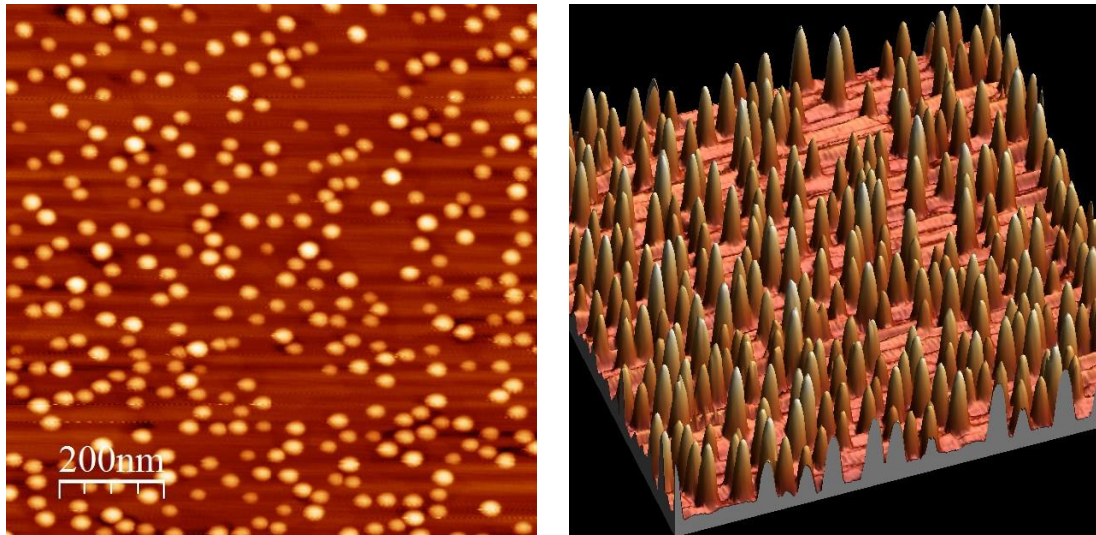


Figure 3.16 (a) 2D and (b) 3D AFM image of QDs

### 3.3.2 Scanning electron microscopy (SEM)

Scanning electron microscopy (SEM) is another method to examine sample morphology. It is used to determine the cross-sectional structure of the QDSC. The operation mechanism is very similar to the AFM apparatus, hence, not illustrated. SEM utilises electron beams, instead of laser beams, to focus the sample. The materials bombarded by the electrons will emit secondary electrons which are detected by the electron screen to depict the sample structure as shown in Figure 3.17.

The SEM image provides very high resolution ( $<1$  nm). It can be used to measure the thickness of the sample layers and compare the monitored thickness in MBE with actual thickness to confirm the MBE growth precision. It can also measure the metal deposition and etching thickness to identify the flaws made during the fabrication process. Figure 3.17 shows an example of a QDSC SEM image, it illustrates an intrinsic layer with a thickness of 109.0 nm (measured from Pa 2 to Pa R2) and an emitter layer with a thickness of 530.8 nm (measured from Pa 1 to Pa R1).



Optical attributes can be analysed using PL measurements. The position of the peaks indicates material compositions or higher excited states. The intensity of the peaks reflects the recombination rate which is an indirect prove of material quality. The full width at half maximum (FWHM), or the sharpness, of the peaks shows the purity of the material or the uniformity of the QDs. Figure 3.18 illustrates peak positions at 830 nm and 1000 nm, corresponding to the bandgap of GaAs and InAs QD at 10 K, respectively. High intensity at GaAs wavelength demonstrates good material quality. The broad FWHM at InAs QDS wavelength suggests QD irregularity such as bimodal distribution of QDs but no indication of any excited states.

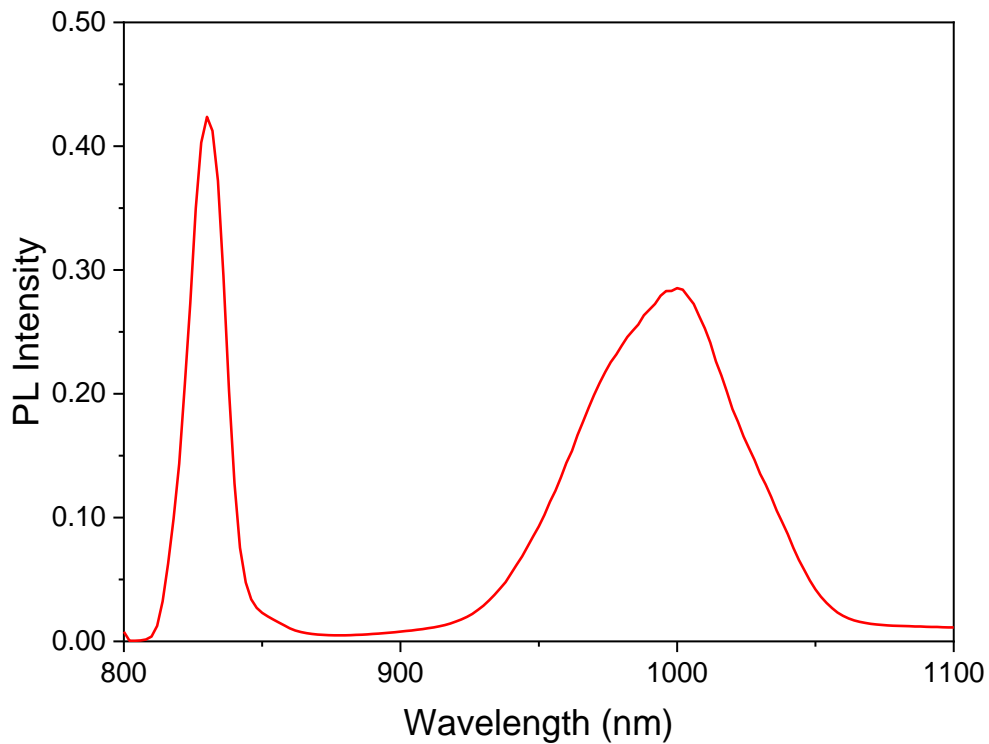


Figure 3.18 PL graph of QDSC

### 3.3.4 External quantum efficiency (EQE)

External quantum efficiency (EQE) measures the current contribution of the SC. In theory, it is a ratio of [12]:

$$EQE = \frac{\text{number of carriers collected}}{\text{number of photons injected at a particular } \lambda} \quad \text{Equation 3.1}$$

which depends on the absorption of the SC material and the carrier collection of the SC device. The operation principle involves an injection of monochromatic beams which produce photons at different wavelengths and the collection of current output through metal contacts at the particular wavelength.

EQE measurements are performed by a monochromator chopping the light from the halogen lamp. The photon wavelengths range from 400 nm to 1100 nm. The current output is collected by connecting the metal contacts to the sourcemeter via a four-wire probe. Data are processed by a SC analysis software which plots an EQE spectrum as shown in Figure 3.19.

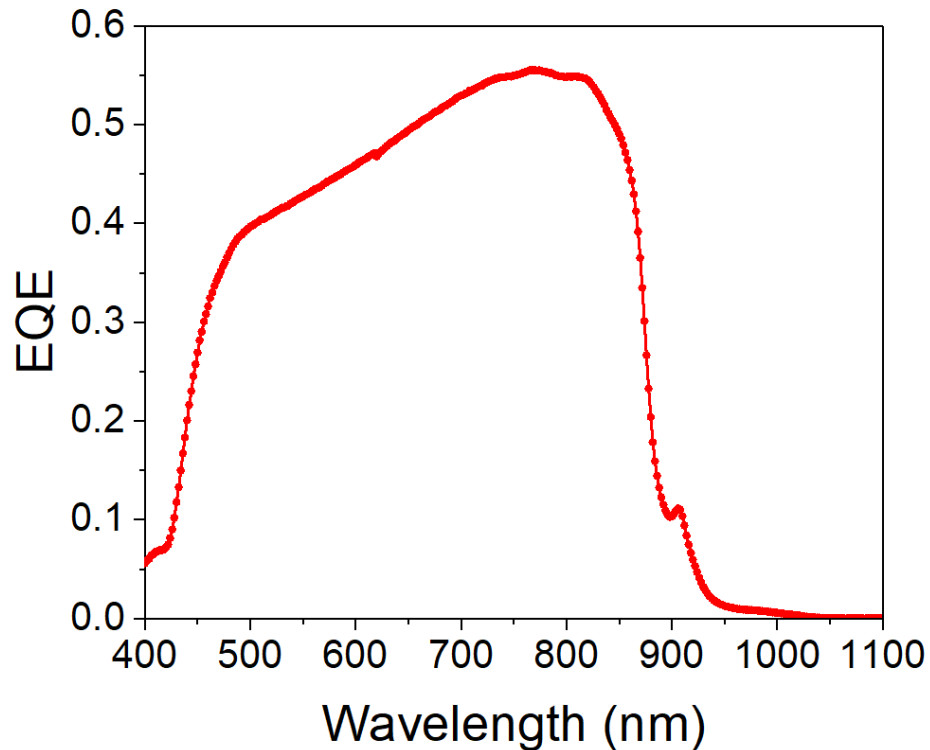


Figure 3.19 EQE spectrum of QDSC

The position and height of the peaks indicates material composition and the magnitude of current contribution, respectively. The sharp drop at 870 nm correspond to GaAs material bandgap at room temperature. The extra peak at 920 nm indicates carrier absorption and extraction at the wetting layer. Most of the current arises at the band edge of GaAs.

### 3.3.5 Current density-voltage ( $J$ - $V$ ) characterisation

The current density versus voltage ( $J$ - $V$ ) characteristics are important parameters for SC devices. The parameters include short-circuit current density ( $J_{sc}$ ), open-circuit voltage ( $V_{oc}$ ), fill factor ( $FF$ ) and most important of all—power conversion efficiency ( $\eta$ ).

This project simulates the AM1.5G testing condition, where the sunlight is produced by a calibrated solar simulator with a xenon lamp. Metal contacts are connected to the sourcemeter to measure current and voltage output. These data are further processed by a SC analysis software to generate the  $J$ - $V$  curves and parameters. Figure 3.20 shows the  $J$ - $V$  curve of a QDSC. The SC has a  $J_{sc}$  of 13.8 mA/cm<sup>2</sup>,  $V_{oc}$  of 0.73 V,  $FF$  of 80 % and  $\eta$  of 10 %.

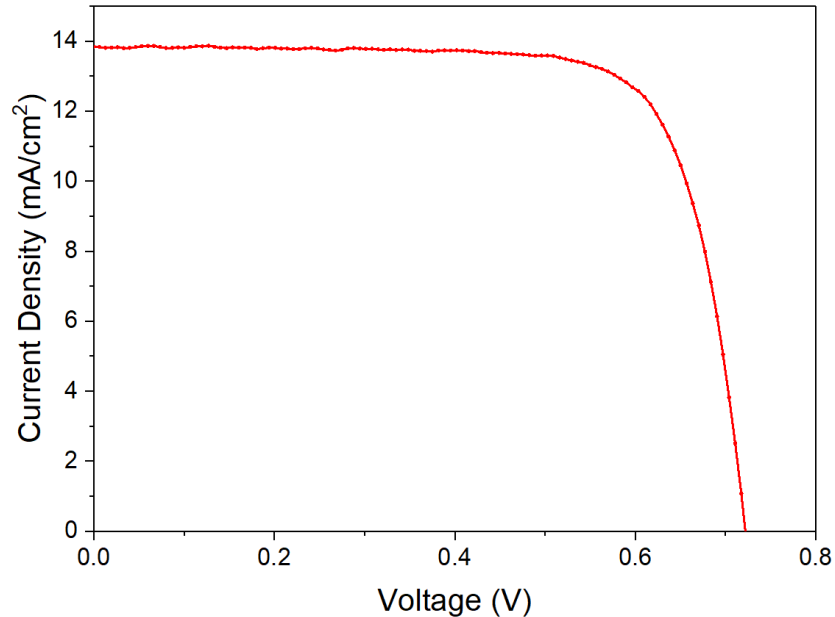


Figure 3.20  $J$ - $V$  curve of QDSC

### 3.3.5.1 Short-circuit current density ( $J_{sc}$ )

Short-circuit current ( $I_{sc}$ ) is the maximum current output of the SC, which is obtained when the voltage is at zero.  $J_{sc}$  is calculated by dividing the  $I_{sc}$  by the active area (0.0707 cm<sup>2</sup>). Moreover,  $J_{sc}$  is the sum of all individual EQE in the spectrum [12]:

$$J_{sc} = q \int_0^{\infty} F(\lambda)EQE(\lambda)d\lambda \quad \text{Equation 3.2}$$

Where  $q$  is electron charge and  $F(\lambda)$  is the individual photon flux (m<sup>-2</sup>s<sup>-1</sup>nm<sup>-1</sup>).

### 3.3.5.2 Open-circuit voltage ( $V_{oc}$ )

Open-circuit voltage ( $V_{oc}$ ) is the maximum voltage output, obtained at zero current. It is dependent on the temperature of device ( $T$ ), short-circuit current density ( $J_{sc}$ ) and dark saturation current ( $J_0$ ) [12]:

$$V_{oc} = \frac{nkT}{q} \ln\left(\frac{J_{sc}}{J_0} + 1\right) \quad \text{Equation 3.3}$$

$J_{sc}$  does not vary in large magnitudes; thus,  $V_{oc}$  is more dependent on  $J_0$  which is limited by the recombination of the material [13]. Theoretically,  $V_{oc}$  is the difference of the quasi-Fermi level split and, hence, the maximum  $V_{oc}$  equals to the size of the material bandgap. Si (GaAs) SCs with a bandgap of 1.1 eV (1.42 eV) has a maximum  $V_{oc}$  of 0.7 V (1.1 V). However, high bandgap materials have a low photon absorption rate, and therefore the current output is reduced.

### 3.3.5.3 Fill factor (FF)

Fill factor ( $FF$ ) describes the “squareness” of a  $J$ - $V$  curve as illustrated in Figure 3.21.

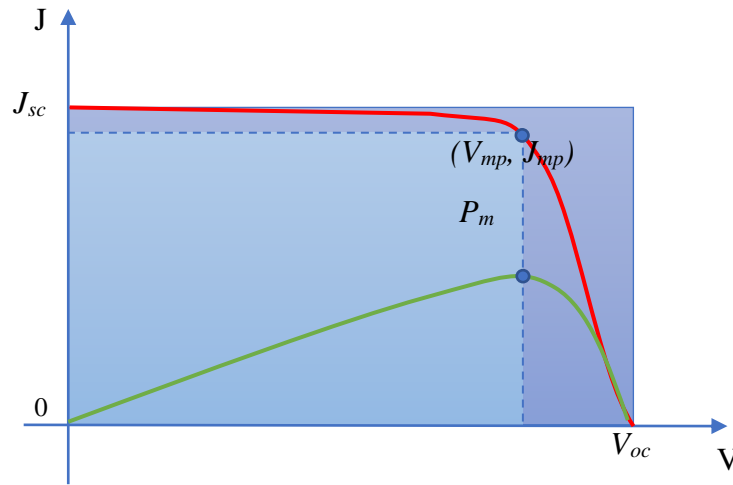


Figure 3.21 detailed  $J$ - $V$  curve

It is a ratio of [12]:

$$FF = \frac{J_{mp}V_{mp}}{J_{sc}V_{oc}} \quad \text{Equation 3.4}$$

Where  $J_{mp}$  and  $V_{mp}$  are the current density and voltage at the maximum power point ( $P_m$ ), respectively. From the figure, it depicts the ratio between the light blue square and dark blue square which reflects how close the fabricated SC is to the ideal SC output. Thus,  $FF$  is an indicator of the fabrication dexterity.

### 3.3.5.4 Power conversion efficiency ( $\eta$ )

Power conversion efficiency ( $\eta$ ) is the ultimate indicator of SC performance. It is calculated using the following equation [12]:

$$\eta = \frac{J_{sc}V_{oc}}{P_{IN}} FF \quad \text{Equation 3.5}$$

Where  $P_{IN}$  is the input power density,  $1000 \text{ Wm}^{-2}$  for AM1.5G. The theoretical maximum efficiency predicted by Shockley and Queisser is 33.1%. According to the April 2020

national renewable energy laboratory (NREL) report, the best single junction SC has 29.1%. Moreover, the best QDSC has 16.6% and our lab-record QDSC has 9.75% efficiency [14].

# Best Research-Cell Efficiencies

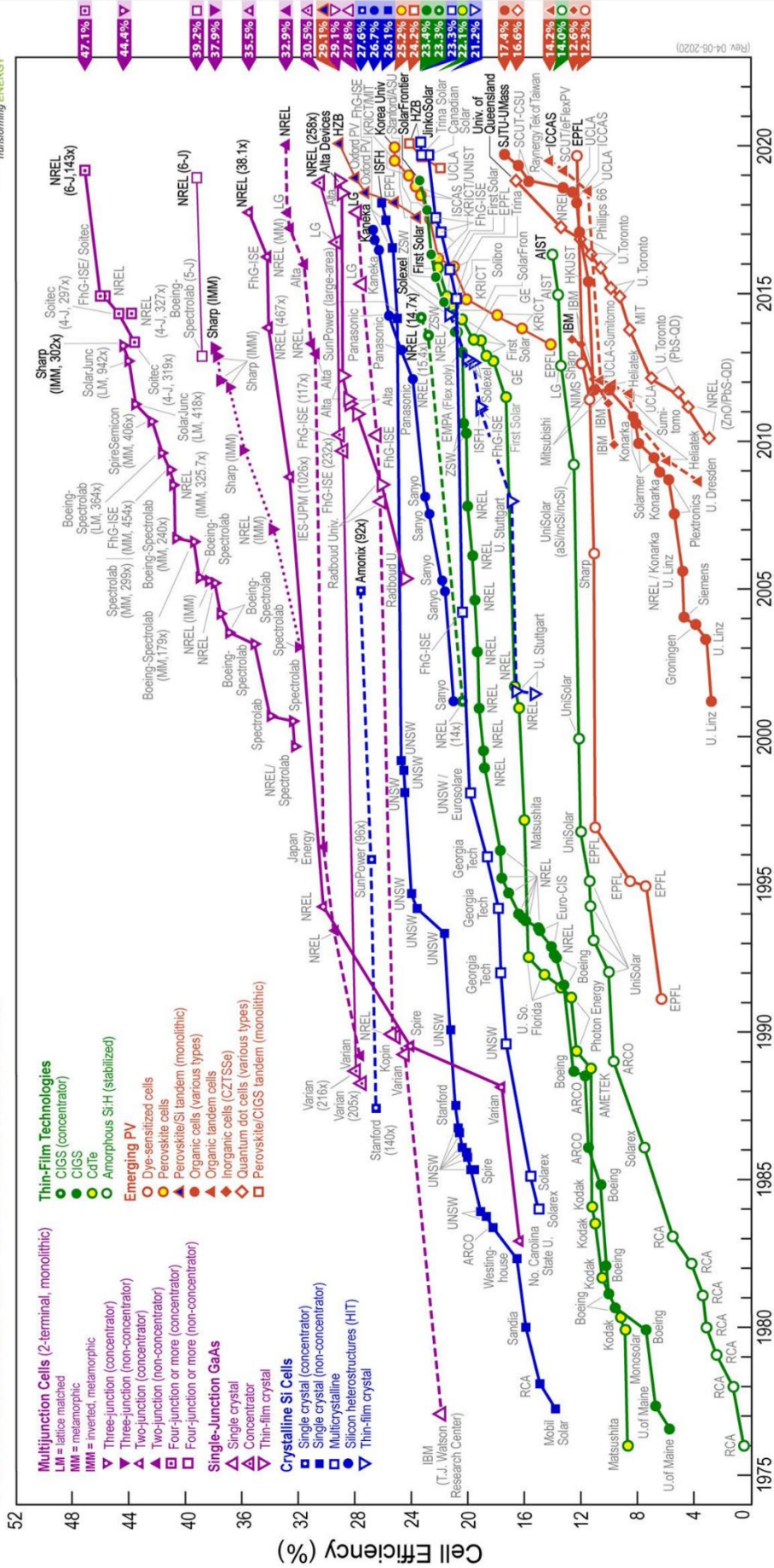


Figure 3.22 NREL solar cell efficiencies Apr 2020

### 3.4 References

- [1] A. Y. Cho and J. R. Arthur, "Molecular beam epitaxy," *Prog. Solid State Chem.*, vol. 10, pp. 157–191, 1975.
- [2] J. R. Arthur, "Molecular beam epitaxy," *Surf. Sci.*, vol. 500, no. 1, pp. 189–217, 2002.
- [3] P. H. Singer, "Molecular Beam Epitaxy.," *Semicond. Int.*, vol. 9, no. 10, pp. 42–47, 1986.
- [4] Y. C. Chen, P. K. Bhattacharya, and J. Singh, "Strained layer epitaxy of InGaAs by MBE and migration enhanced epitaxy - comparison of growth modes and surface quality," *J. Cryst. Growth*, vol. 111, no. 1–4, pp. 228–232, 1991.
- [5] A. Marti, L. Cuadra, and A. Luque, "Quantum dot intermediate band solar cell," *Conf. Rec. IEEE Photovolt. Spec. Conf.*, Anchorage AK USA, vol. 2000-Jan, pp. 940–943, 2000.
- [6] C. Heyn, "Critical coverage for strain-induced formation of InAs quantum dots," *Phys. Rev. B*, vol. 64, no. 16, p. 165306, Oct. 2001.
- [7] Y. Wang, Z. Ren, M. Thway, K. Lee, S. Yoon, I. Peters, T. Buonassisi, E. Fitzgerald, C. Tan, and K. Lee, "Fabrication and characterization of single junction GaAs solar cells on Si with As-doped Ge buffer," *Sol. Energy Mater. Sol. Cells*, vol. 172, no. July, pp. 140–144, 2017.
- [8] M. Yamaguchi, A. Yamamoto, and Y. Itoh, "Effect of dislocations on the efficiency of thin-film GaAs solar cells on Si substrates," *J. Appl. Phys.*, vol. 59, no. 5, pp. 1751–1753, 1986.
- [9] Dow Chemical Company, "Microposit S1800 G2 Series Photoresists," *Data Sheet*, no. October, pp. 1–6, 2006.
- [10] MicroChem Corp., "LOR Lift Off Resists Datasheet," pp. 1–6, 2002.

- [11] P. Lam, J. Wu, S. Hatch, D. Kim, M. Tang, H. Liu, J. Wilson, and R. Allison, “Effect of rapid thermal annealing on InAs/GaAs quantum dot solar cells,” *IET Optoelectron.*, vol. 9, no. 2, pp. 65–68, Apr. 2015.
- [12] J. Nelson, *The Physics of Solar Cells*. Imperial College Press, London, 2003. ISBN-13 978-1-86094-3492
- [13] A. Augusto, S. Y. Herasimenka, R. R. King, S. G. Bowden, and C. Honsberg, “Analysis of the recombination mechanisms of a silicon solar cell with low bandgap-voltage offset,” *J. Appl. Phys.*, vol. 121, no. 20, p. 205704, 2017.
- [14] S. Chan, D. Kim, A. Sanchez, Y. Zhang, M. Tang, J. Wu, and H.Liu, “InAs/GaAs quantum dot solar cells with quantum dots in the base region,” *IET Optoelectron.*, vol. 13, no. 5, pp. 215–217, Oct. 2019.

## Chapter 4 InAs/GaAs quantum dot solar cell with QDs in base region

*The positioning effect of quantum dots (QDs) embedded within the n-type base region is investigated in this chapter. The purpose of embedding the QDs into the base region was to induce background doping effect that recovers lost voltage. Three quantum dot solar cell (QDSC) samples were grown by MBE, in which the QDs are positioned in the intrinsic, deep base or shallow base region. The results show strong voltage enhancement (27%) with 9.75 % power conversion efficiency for deep base region QDSC. Shallow base region QDSC also has strong voltage enhancement (22%), but the current density falls short, resulting in 7.53% efficiency. Nonetheless, the results confirm that the background doping effect is present and the effect is stronger than the Si-doped QDs in the intrinsic region.*

## 4.1 Introduction

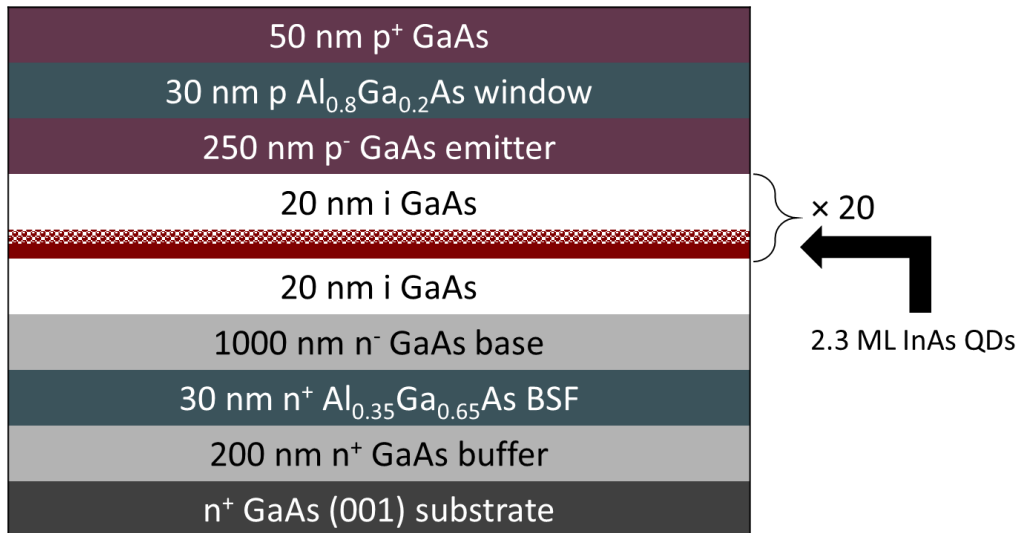
Since the IBSC proposal in 1997, QDSCs have attracted considerable attention due to their potential to achieve a theoretical conversion efficiency of IBSCs up to 63.2 % [1]–[3]. In particular, the unique property of QDs, such as three-dimensional carrier confinement and discrete density of states, offers the energy levels of the confined states in a QD, which acts as an intermediate band in SCs [4]. A great deal of effort has been dedicated to preventing the substantial  $V_{oc}$  drop while minimising the degradation of  $J_{sc}$  in QDSCs [5]–[7]. For instance, Sablon *et al.* reported that the negatively charged n-doped QDs in QDSCs significantly improved the  $J_{sc}$  without the deterioration of  $V_{oc}$  [8]. Lam *et al.*, investigating the effect of n-type doping concentration of QDs in QDSCs, demonstrated that the  $V_{oc}$  increased from 56 mV to 105 mV as n-type doping level increased from 6 to 18 electrons per QD [9]. In addition to the n-type doping of QD, Driscoll *et al.* theoretically suggested that embedding QDs into the reduced recombination regions resulted in voltage recovery [10]. Therefore, QDSCs with QDs in the base region provided better voltage output than those in the emitter region.

In this chapter, we investigate the influence of QD position within the base or the n-type regions, in order to recover the voltage degradation. Unlike the SC samples from Sablon *et al.* and Lam *et al.*, which include a sheet of Si-dopant in the spacer layer or in the wetting layer, we do not include any Si-dopants but relocate the QD layers into the n-type (Si-doped) base region. We expect this design should also achieve the n-doping effects such as voltage enhancements via the background Si-dopants. Furthermore, we split the base region into upper and lower sections and investigate in detail which section provides a stronger enhancement. The samples with two different QD positions are also compared with conventional QDSC sample. The one has QDs in the upper section (close to the intrinsic region) and the other has QDs in the lower section (close towards the substrate), which are denoted by shallow and deep base QDSCs, respectively.

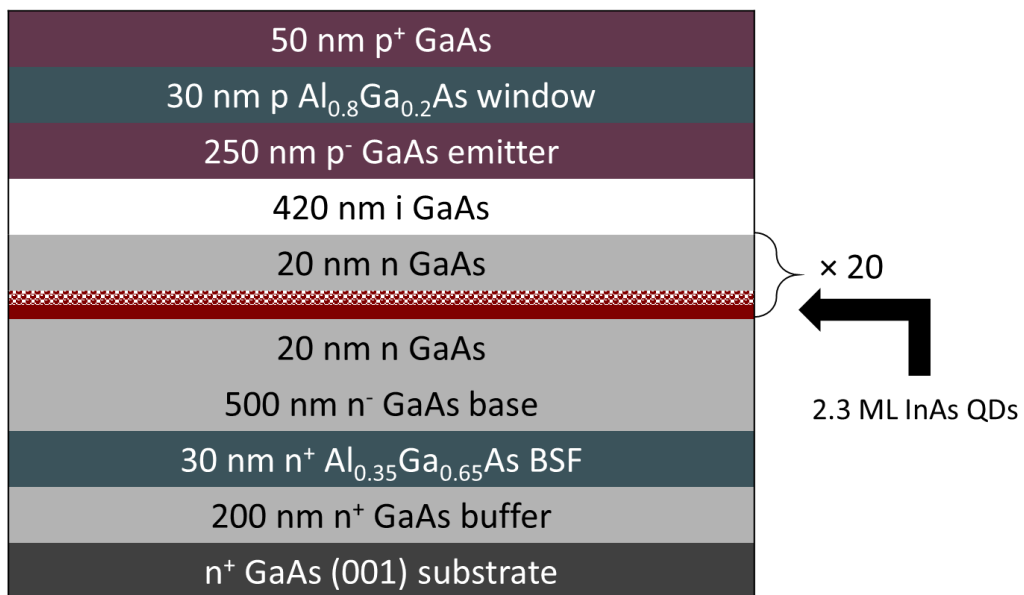
## 4.2 Experimental work

### 4.2.1 Growth

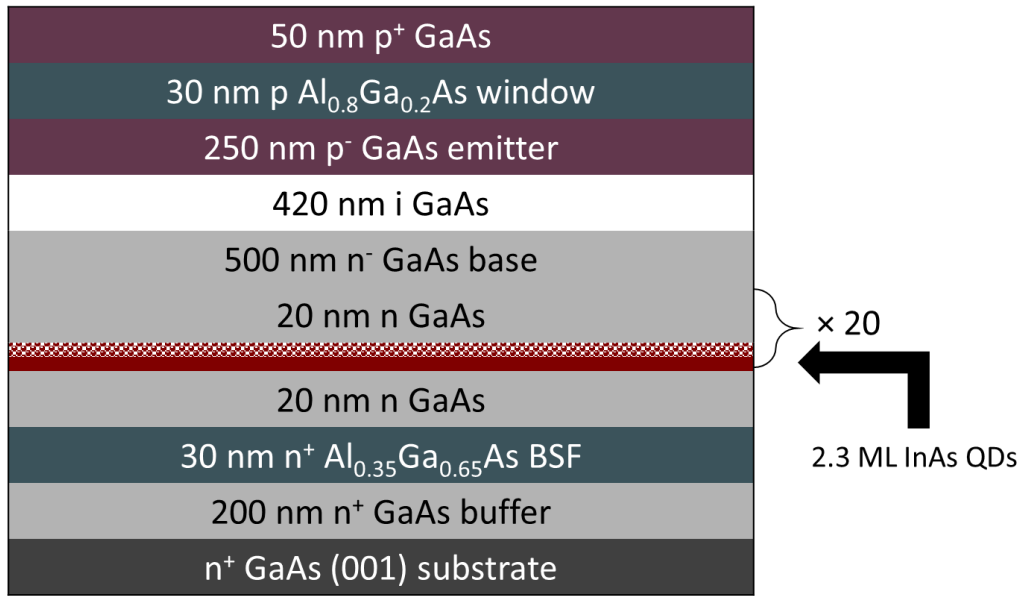
To investigate the effect of QD position in the base region on the performance of QDSCs, three QDSC samples are grown by MBE, as shown in Figure 4.1. Unlike the reference sample in which the QDs are located in the middle of the intrinsic region, the shallow and deep base QDSC samples position the QDs in upper and lower base region, respectively.



(a) Ref QD



(b) Shallow QD



(c) Deep QD

Figure 4.1 QDSC sample structures with QDs in (a) intrinsic region (b) shallow base region (c) deep base region

All samples have a typical p-i-n structure, consisting of a 200 nm n<sup>+</sup>-GaAs buffer layer with Si doping level of  $1 \times 10^{18} \text{ cm}^{-3}$ , a 30 nm n<sup>+</sup>-Al<sub>0.35</sub>Ga<sub>0.65</sub>As Back surface field (BSF) with Si doping level of  $1 \times 10^{18} \text{ cm}^{-3}$ , a 1000 nm n GaAs base region with Si doping level of  $1 \times 10^{17} \text{ cm}^{-3}$ , a 420 nm i-GaAs intrinsic region, a 250 nm p<sup>-</sup>-GaAs emitter region with Be doping level of  $2 \times 10^{18} \text{ cm}^{-3}$ , a 30 nm p-Al<sub>0.8</sub>Ga<sub>0.2</sub>As window with Be doping level of  $2 \times 10^{18} \text{ cm}^{-3}$  and 50 nm p<sup>+</sup>-GaAs contact layer with Be doping level of  $1 \times 10^{19} \text{ cm}^{-3}$ .

For the QD regions, 20 layers of 2.3 monolayer InAs QDs separated by 20 nm GaAs spacer layer were inserted in the intrinsic, shallow base and deep base region. The GaAs spacer layer for both shallow and deep base samples were doped with Si at  $1 \times 10^{17} \text{ cm}^{-3}$ , while the spacer layers for the reference sample are undoped. Moreover, the QDs were grown under the Stranski-Krastanov mode at a substrate temperature of 500 °C. High growth temperature GaAs spacer layers were applied during the growth to suppress formation of dislocations.

### 4.2.2 Fabrication

Post MBE growth, samples are cleaved into quarter-wafers and cleaned in acetone and isopropanol solution for 10 minutes. To remove the surface oxides, the samples are treated with diluted ammonia solution (1:19) for 50 seconds. Then, a photolithography pattern was defined to isolate the individual devices and subsequently, samples were wet-etched to a height of 4000 nm using  $\text{H}_2\text{SO}_4$ :  $\text{H}_2\text{O}$ :  $\text{H}_2\text{O}$  (1:10:80) mixture solution for 5 minutes. In order to form an n-type contact, a Ni/AuGe/Ni/Au (10/100/30/300 nm) scheme was thermally evaporated onto the backside of the samples. For the p-type contact, a grid pattern was defined by photolithography and a Ti/Pt/Au (20/50/400 nm) scheme was magnetically sputtered onto the surface of the samples. To obtain ohmic contact formation, thermal annealing was applied to all samples at 420 °C for 30 seconds. Noted that the anti-reflection coating and surface passivation are not applied.

### 4.2.3 Characterisation

A Veeco Nanoscope V atomic force microscope (AFM) is used to examine the QD morphology of an uncapped QDSC sample. Transmission electron microscopy (TEM) is conducted by our collaborative partner from Warwick. The temperature dependent and power dependent photoluminescence (PL) spectra are obtained using a diode-pumped solid-state laser at 2.33 eV (532 nm) excitation power. Temperature is controlled (from 10 K to 300 K) by a Helium-cooled cryostat during the measurement. Current density versus voltage (J-V) characteristics are measured by a calibrated solar simulator with a xenon lamp under one sun (AM 1.5G) illumination at room temperature. Data is collected by a sourcemeter and processed using a software to plot the J-V graph. External quantum efficiency (EQE) measurements are carried out using the light beam from a halogen lamp, which are passed into a monochromator. The monochromatic beams are calibrated with a GaAs photo-diode and the data is analysed using a software to plot the EQE spectrum.

## 4.3 Results and Discussion

### 4.3.1 AFM

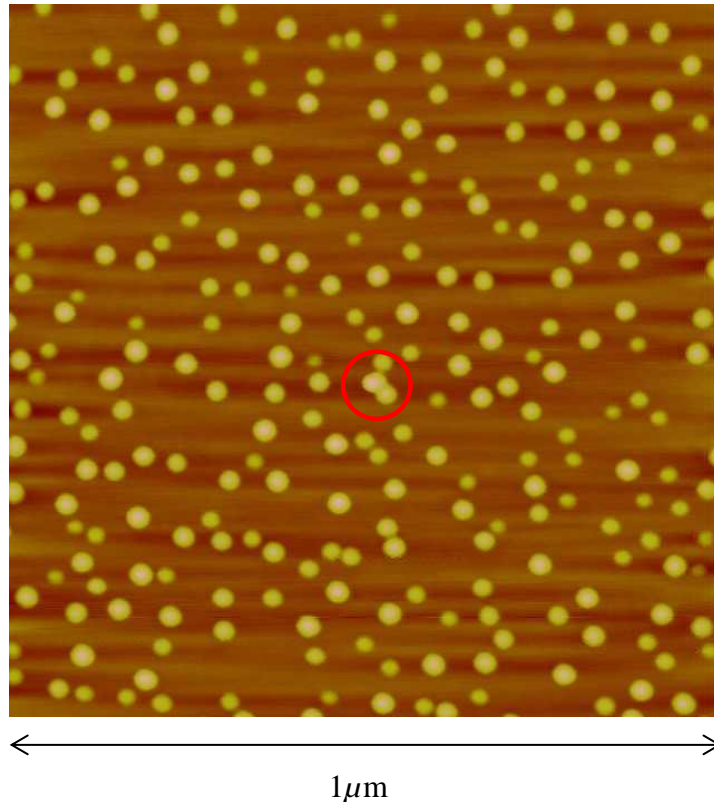


Figure 4.2 AFM image of the uncapped QDSC

To characterise the surface morphology of QDs, AFM measurement was carried out. Figure 4.2 presents the AFM image of the uncapped QDSC that has no emitter layer. The dot density is estimated to be  $3.4 \times 10^{10} \text{ cm}^{-2}$ . The number of defects is not obvious, but a cluster of 3 dots is spotted at the centre of the image. Bimodal QDs are present in this sample, i.e. QDs merge into two sizes, hence, are not uniform. The diameter of the large QDs is 30 nm with an average height of 5 nm and the smaller QDs has 15 nm diameter with 3 nm height. These non-uniformity has an impact of broadening the peaks in the PL spectra, but the QD height difference of 2 nm for this particular sample is not significant [11], [12].

### 4.3.2 TEM

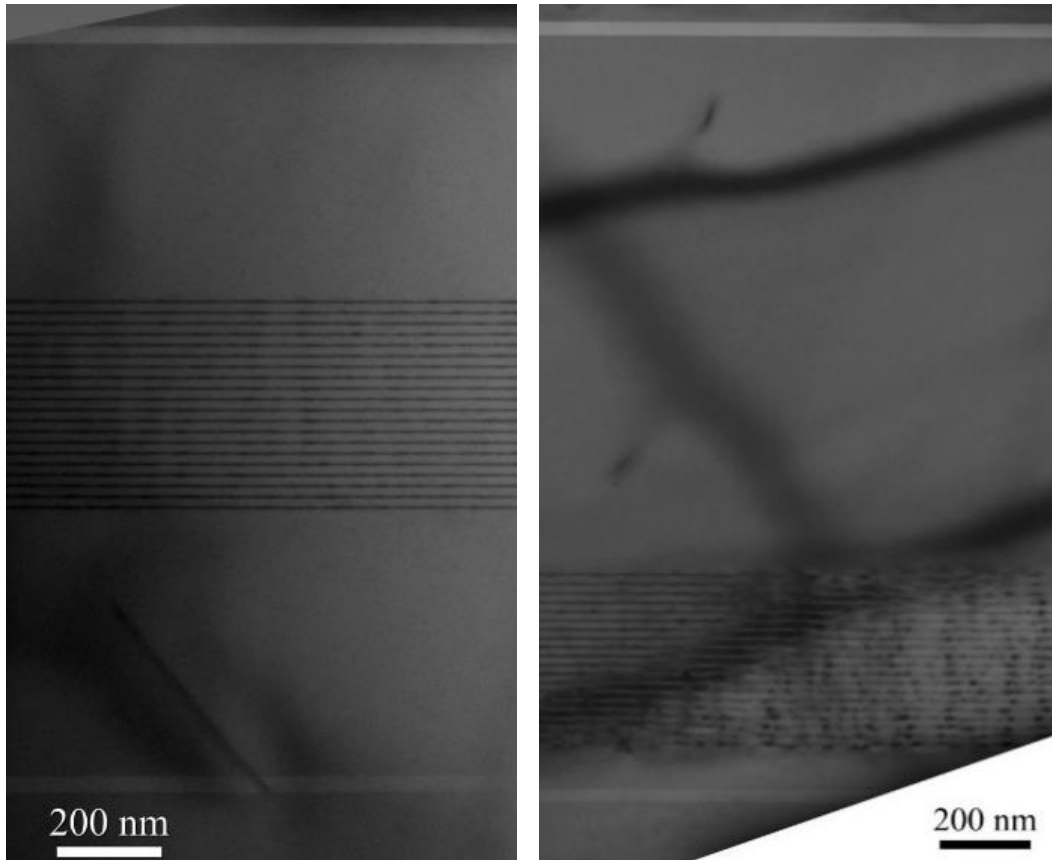
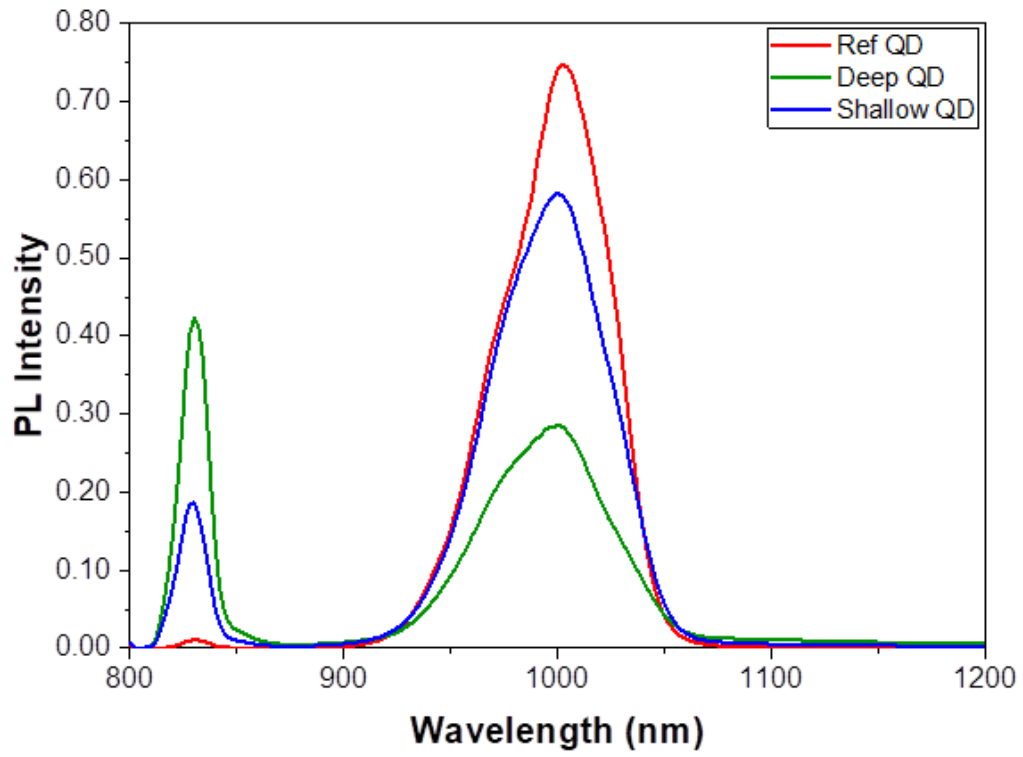


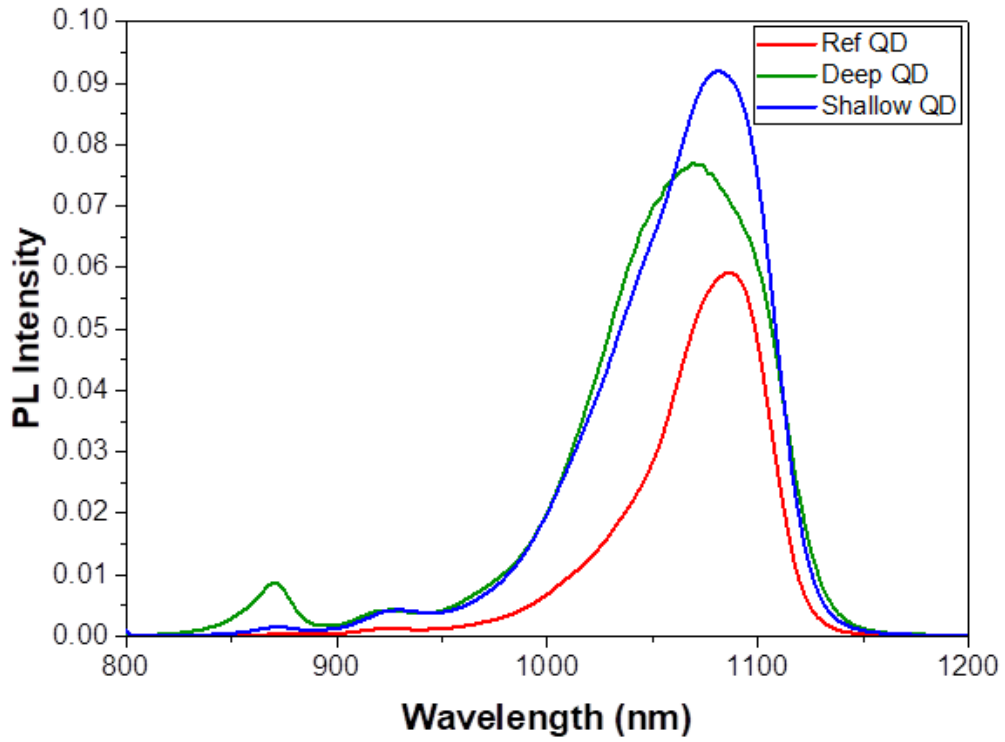
Figure 4.3 Cross sectional TEM images of (a) shallow and (b) deep base QDSCs

Figure 4.3 presents the TEM images of the shallow and deep base QDSCs. Due to similar colour of identical materials, the intrinsic and base regions cannot be distinguished from the TEM images. Therefore, the BSF and window layers, with a brighter colour, are used as references to inspect the sample structure. It is observed that 20 layers of QDs are positioned in the middle (Figure 4.3 (a)) and lower section (Figure 4.3 (b)) of the structure, which confirms that QDs are located at the correct position.

### 4.3.3 PL



(a)



(b)

Figure 4.4 PL graphs of QDSCs at (a) 10 K and (b) 300 K

To characterise the optical properties of the QDSCs, the PL measurements were conducted at 10 K and 300 K. As shown in Figure 4.4 (a), there are two evident peaks positioned at 830 nm and 1000 nm for all samples at 10 K. The peaks at 830 nm and 1000 nm correspond to the bandgap of GaAs and InAs QD, respectively. The narrow linewidth of the GaAs peaks indicates the high quality of materials. On the other hand, the FWHM of the QD peak is broadened due to the QD bimodal size distributions, which was confirmed by previous AFM image.

In terms of the peak intensity, it is observed that ref QD sample has the lowest peak intensity at 830 nm but the highest at 1050 nm. On the contrary, deep QD sample has the highest GaAs peak intensity but the lowest QD peak intensity. This behaviour can be explained by the position of the QDs within the sample. For the ref QD sample, QDs are embedded in the intrinsic region which is closer to the surface than the other samples. Accordingly, the emission from QDs (GaAs) is more (less) likely to be detected. Similarly, QDs in deep QD sample are buried further away from the surface and, thus, QD emission is more difficult to be observed.

As shown in Figure 4.4 (b), the room temperature PL measurements showed red-shifted GaAs and InAs QD peak at 870 nm and ~1080 nm, respectively. In addition, there are extra peaks appearing at 930 nm wavelength. This alteration has been reported in most QDSCs and the peak at this wavelength corresponds to the wetting layer (WL). The formation of WL is inevitable under S-K growth and the nature of WL is a 2-D quantum well layer that can increase the dimensionality of the QDs (0-D). The appearance of WL peaks signifies potential voltage losses in the QDSCs.

The peak intensities have also changed with rising temperature. The QD peak intensities are far more evident than GaAs intensities due to the temperature-independent properties of QDs [13], [14]. Also, unlike the shallow and deep base QD samples, the PL intensity of ref QD sample dramatically decreased as the temperature increased, indicating that the ref QD sample is more susceptible to thermal carrier escapes. This is because the QDs located in the intrinsic region experience a built-in electric field promoting the carriers to escape

out of the QDs [15]. On the other hand, for the shallow and deep QD samples, the QDs located outside the intrinsic region do not undergo the internal field. Hence, the less carriers escape out of the QDs, resulting in higher QD peak intensities.

#### 4.3.4 EQE

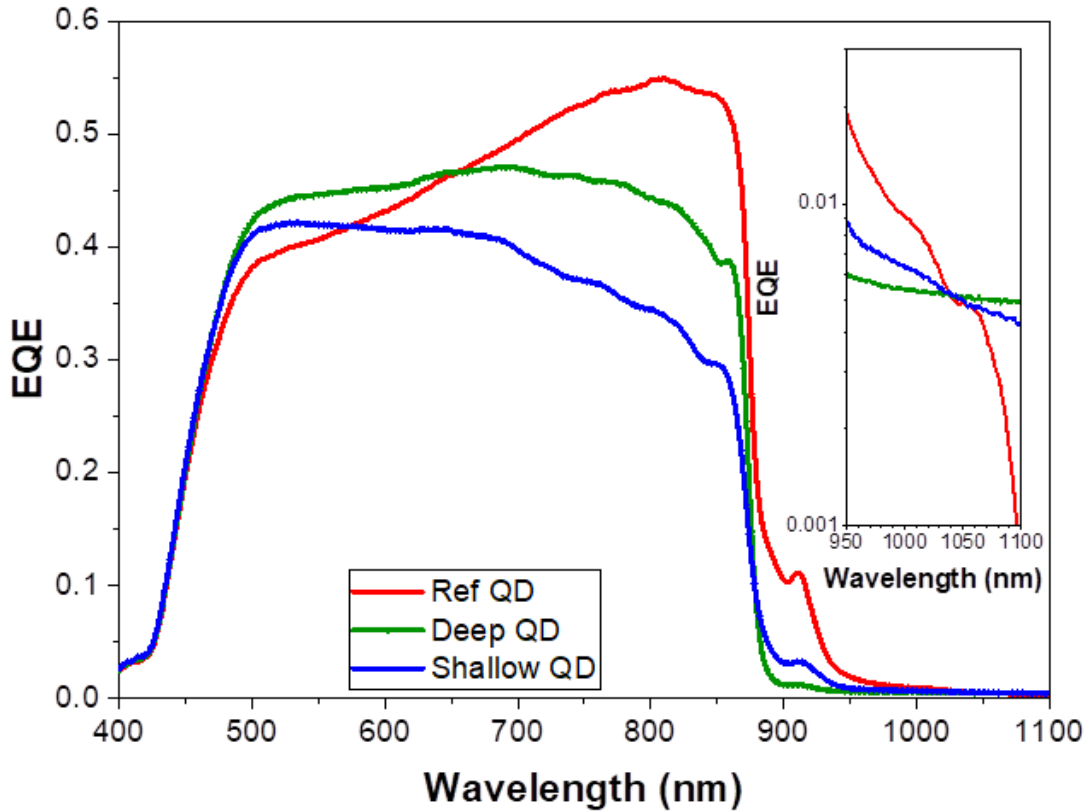


Figure 4.5 EQE spectra of QDSC with log-scaled sub-bandgap inset

Figure 4.5 illustrates the external quantum efficiency (EQE) spectra of the QDSCs. The inset shows the sub-bandgap spectrum around QD absorption region, where the y-axis is adjusted to log-scale. In linear-scaled EQE spectrum, sharp drops at 870 nm are observed in all samples due to GaAs bandgap. Within the supra-bandgap region (400 nm to 900 nm), the ref QD sample has shown an increasing current contribution whereas the deep and shallow QD samples have a diminishing current contribution. In particular, the shallow QD sample shows a more significant decline, which can be explained by the carrier diffusion length. Embedding QDs in the base region reduces the diffusion length of the holes,

causing the photogenerated carriers to be lost at the QD sites before contributing to photocurrent. Moreover, for the shallow QD sample, the close location of QDs to the depletion region resulted in a shorter diffusion length of holes and higher probability for carrier recombination compared with the deep QD sample, finally leading to the lower photocurrent.

Beyond the supra-bandgap region, current contribution at 915 nm arises from the WLs. In this region, the ref QD sample also showed much higher current contribution than that of both deep and shallow QD samples in a similar way with the supra-bandgap region. In the inset of Figure 4.5, log-scaled EQE spectrum shows the sub-bandgap region (950 nm to 1100 nm) where QD absorptions contributed to the photocurrent. Again, ref QD sample has shown greater current contribution than both base QD samples and the cause of this observation is, still, the carrier diffusion length. The ref QD sample, for which QDs are located in the intrinsic region, utilises the internal electric field to sweep photogenerated carriers and, hence, shows higher carrier collection rate. On the other hand, QDs located outside intrinsic region do not undergo this drift force. Thus, the carriers have a shorter diffusion length and higher probability to recombine.

#### 4.3.5 J-V

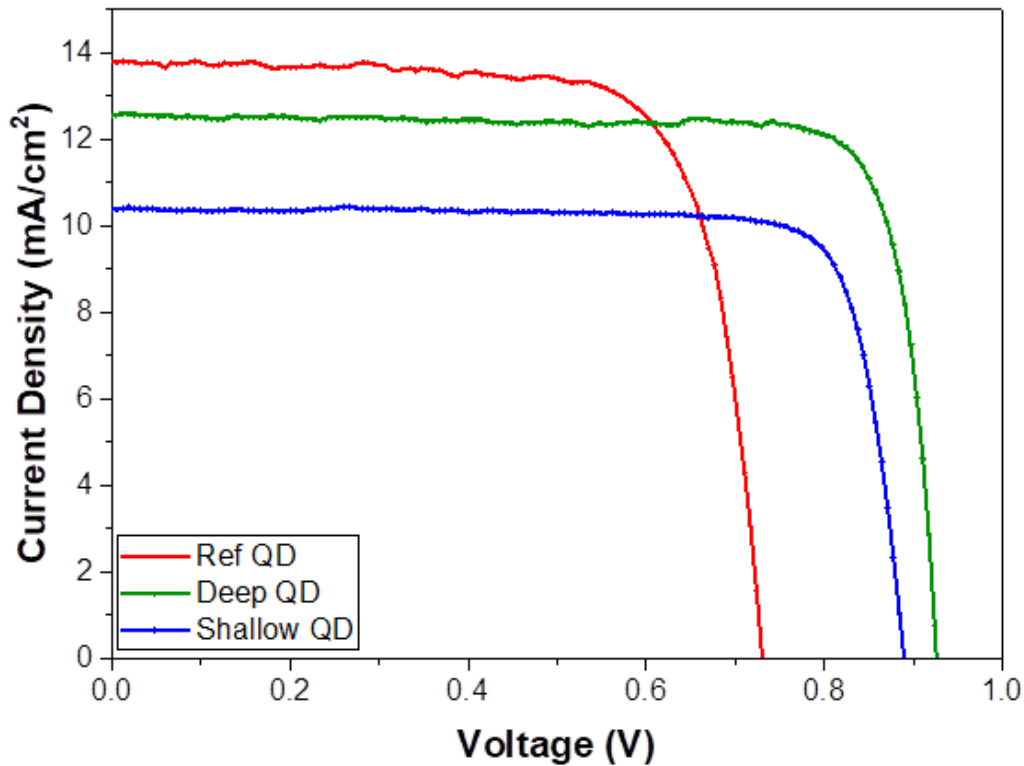


Figure 4.6 J-V characteristic of QDSCs

Device	$J_{sc}$ (mA/cm <sup>2</sup> )	$V_{oc}$ (mV)	$FF$ (%)	$\eta$ (%)
Ref QD	13.78	730.02	74.67	7.52
Deep QD	12.58	926.20	83.63	9.75
Shallow QD	10.40	889.53	82.46	7.63

**Table 4.1 Parameters of J-V Characteristics**

Figure 4.6 illustrates the J-V curves of the QDSCs and Table 3.1 records the solar cell performance parameters. The ref QD sample has the highest current density of 13.78 mA/cm<sup>2</sup>, but, due to a low voltage output, the sample obtain the lowest conversion efficiency of 7.52%. This outcome has been anticipated since the observation of room temperature PL measurement when the peak at 930 nm was identified. Further results from EQE spectrum have supported this finding. Although the strong current contribution

between supra- and sub- bandgap would result in a high  $J_{sc}$ , the continuous states within the wetting layers can reduce the effective bandgap between CB and IB by promoting carrier escapes. Consequently, the effect of carrier escape has caused a drastic voltage reduction that was enough to counter the benefit of current production and, thus, result in the lowest overall efficiency.

The shallow and deep QD samples have achieved  $V_{oc}$  of 889 mV and 926 mV respectively. According to the PL results, re-locating the QDs away from the intrinsic region preserves the GaAs material quality of the absorption region, and, hence, higher radiative recombinations are observed at 870 nm wavelength, especially for the deep QD sample. As a result, the deep QD sample has a higher voltage output than that of the shallow QD sample. In comparison to the ref QD sample, the inclusion of QDs within the intrinsic region may introduce defect states, as well as the intermediate band states, causing additional voltage reduction (along with carrier escape).

In terms of  $J_{sc}$ , the shallow and deep QD samples have achieved 10.40 mA/cm<sup>2</sup> and 12.58 mA/cm<sup>2</sup>, respectively, both of which are less than the ref QD. The cause of reduction is attributed to the shortening of the diffusion length which ultimately resulted in poor carrier collection. The deep QD sample with a longer carrier diffusion length than the shallow QD sample has achieved a higher  $J_{sc}$ .

Despite the less carrier collection, the  $\eta$  of shallow and deep QD samples are higher than the ref QD sample. In particular, the deep QD sample has obtained a  $\eta$  of 9.75%, which is a 29% marginal increase compared to 7.52% of the ref QD.

#### 4.4 Discussion

In general, QDSC that attempt to implement the IBSC have their QD layers inserted into the intrinsic region, because photogenerated carriers can diffuse and be collected via the aid of build-in electric field [15]. As shown in Figure 4.7 (a), electron generated within the electric field region experience a drift force which drives it out of the region and towards the contacts. On the other hand, if the QD layers are located outside the intrinsic region, into the base region (Figure 4.7 (b)&(c)), the QDs are more likely to act as defective

recombination sites (rather than sub-bandgap absorption matrix) and trap the electrons before reaching the gold contact.

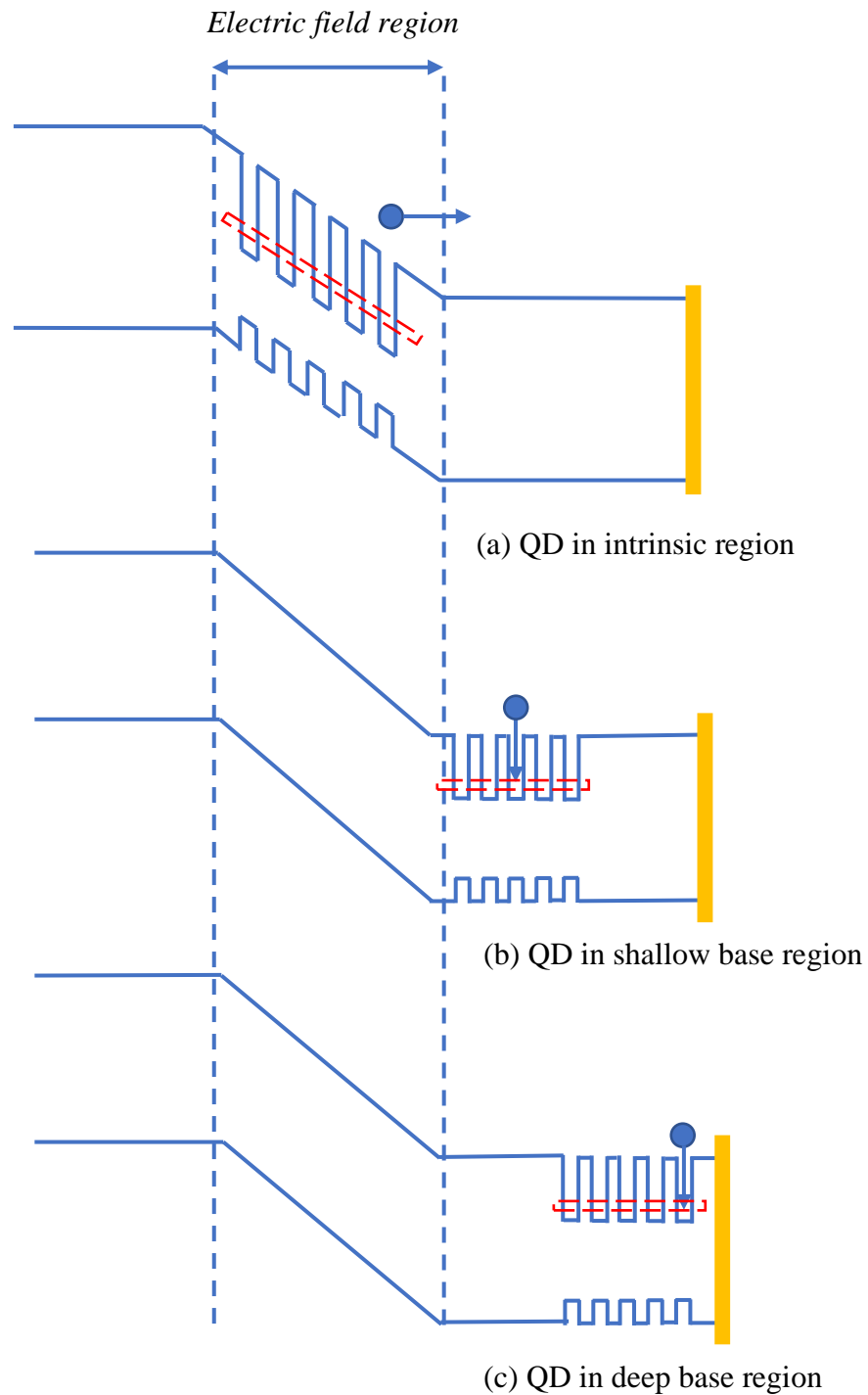


Figure 4.7 A simplified schematic diagram of the energy band of (a) Ref QD, (b) shallow QD and (c) deep QD under operation: including the electric field, QD region (red dotted box), electron movements and gold contact

However, it is worth pointing out that even if the electron in Figure 4.7 (a) has been drift out of the intrinsic region, it still needs to travel through the base region then reach the metal contact. This implies that losses can still occur within the base region. Furthermore, Figure 4.7 illustrates an approximation of the electric field region (though in theory it should be sufficiently accurate), the actual area of effect of the electric field could be wider, for example covers the QD layers at the shallow base region. Although it is very unlikely that the electric field will cover the QD layers in the deep base region, carriers absorbed (trapped) by the QDs at that region may still escape by colliding with a photon with low energy. In fact, photons with low energy are more likely to exist deeper into the material.

Based on our finding, the results have shown that relocating the QDs outside the intrinsic region *indirectly* improve the GaAs material quality in the intrinsic region and that is *potentially* more important than utilising the electric field to sweep the electrons out of the region [18]. Securing a high-quality absorption region increases the number of photogenerated carriers that can be later separated and collected. Without a reasonable absorption region, there would be no carriers to utilise the internal electric field for collection. Thus, we found that photon absorption rate has a higher priority than carrier collection rate.

The main focus, here, would be to find the best region to locate the QD layers [19]. From the data, embedding the QDs into the shallow base region is not effective. QDs act as recombination centres regardless which region they are positioned. However, if the recombination centres are adjacent to the region of maximum carrier generation (the absorption region), then the probability of recombination is higher [18]. As a result, carriers are lost due to recombination and, ultimately, current production is reduced. Locating the QD layers further away from the absorption region can partially solve the recombination problem. As demonstrated in this work, embedding the QDs in deeper base region have, first, preserved the absorption region quality and, also, avoided the carrier recombination issue, resulting in the highest conversion efficiency.

## 4.5 Conclusion

The purpose of this project is to achieve background doping effects such as voltage recovery by locating QDs in the base regions. We have accomplished this by designing and fabricating three QDSC devices with QDs embedded in different regions: intrinsic, shallow base and deep base regions. The results have shown both samples with QDs embedded within the base region have achieved voltage recovery of at least 150 mV (27%). This is due to the preservation of high material quality that has suppressed carrier recombination from QDs and maintained an effective bandgap. However, the shallow base sample with QDs located adjacent to the absorption region suffered from a reduced current density of  $1.2 \text{ mA/cm}^2$  (10%) with respect to deep base sample. This current reduction is attributed to a lower carrier collection that is proportional to the diffusion length. Although this drawback is insignificant when compared to the overall power conversion efficiency, it should be taken into account in future investigations.

## 4.6 References

- [1] A. Luque and A. Martí, “Increasing the Efficiency of Ideal Solar Cells by Photon Induced Transitions at Intermediate Levels,” *Phys. Rev. Lett.*, vol.78, no.26, pp. 5014-5017, Jun. 1997.
- [2] A. Luque, A. Martí, and C. Stanley, “Understanding intermediate-band solar cells,” *Nat. Photonics*, vol. 6, no. 3, pp. 146–152, 2012.
- [3] A. Martí, L. Cuadra, and A. Luque, “Quantum dot intermediate band solar cell,” *Conf. Rec. IEEE Photovolt. Spec. Conf.*, Anchorage AK USA, vol. 2000-Jan, pp. 940–943, 2000.
- [4] A. Martí, E. Antonlin, C. Stanley, C. Farmer, N. Lopez, P. Diaz, E. Canovas, P. Linares, A. Luque, “Production of photocurrent due to intermediate-to-conduction-band transitions: A demonstration of a key operating principle of the intermediate-band solar cell,” *Phys. Rev. Lett.*, vol. 97, no. 24, pp. 1–4, 2006.
- [5] D. Kim, M. Tang, J. Wu, S. Hatch, Y. Maidaniuk, V. Dorogan, Y. Mazur, G. Salamo, and H. Liu, “Si-Doped InAs/GaAs Quantum-Dot Solar Cell with AlAs Cap Layers,” *IEEE J. Photovoltaics*, vol. 6, no. 4, pp. 906–911, 2016.
- [6] D. Kim, S. Chan, M. Tang, J. Wu, and H. Liu, “The influence of direct, delta, and modulation QD Si doping on InAs/GaAs quantum dot solar cells,” in *2018 IEEE 7th World Conference on Photovoltaic Energy Conversion, WCPEC 2018 - A Joint Conference of 45th IEEE PVSC, 28th PVSEC and 34th EU PVSEC*, 2018, pp. 2759–2762.
- [7] F. K. Tutu, P. Lam, J. Wu, N. Miyashita, Y. Okada, K. Lee, N. Ekins-Daukes, J. Wilson, and H. Liu, “InAs/GaAs quantum dot solar cell with an AlAs cap layer,” *Appl. Phys. Lett.*, vol. 102, no. 16, p. 163907, 2013.
- [8] K. A. Sablon, J. W. Little, V. Mitin, A. Sergeev, N. Vagidov, and K. Reinhardt, “Strong enhancement of solar cell efficiency due to quantum dots with built-in charge,” *Nano Lett.*, vol. 11, no. 6, pp. 2311–2317, 2011.

- [9] P. Lam, S. Hatch, J. Wu, M. Tang, V. Dorogan, Y. Mazur, G. Salamo, I. Ramiro, A. Seeds, and H. Liu, “Voltage recovery in charged InAs/GaAs quantum dot solar cells,” *Nano Energy*, vol. 6, pp. 159–166, 2014.
- [10] K. Driscoll, M. F. Bennett, S. J. Polly, D. V. Forbes, and S. M. Hubbard, “Effect of quantum dot position and background doping on the performance of quantum dot enhanced GaAs solar cells,” *Appl. Phys. Lett.*, vol. 104, no. 2, p. 023119, 2014.
- [11] S. Hatch, J. Wu, K. Sablon, P. Lam, M. Tang, Q. Jiang, and H. Liu, “InAs/GaAsSb quantum dot solar cells,” *Opt. Express*, vol. 22, no. S3, pp. A679–A685, 2014.
- [12] D. Kim, S. Hatch, J. Wu, K. Sablon, P. Lam, P. Jurczak, M. Tang, W. Gillin, and H. Liu, “Type-II InAs/GaAsSb Quantum Dot Solar Cells with GaAs Interlayer,” *IEEE J. Photovoltaics*, vol. 8, no. 3, pp. 741–745, 2018.
- [13] M. A. Borji, A. Reyahi, E. Rajaei, and M. Ghahremani, “Effect of temperature on  $\text{In}_x\text{Ga}_{1-x}\text{As}/\text{GaAs}$  quantum dots,” *Pramana - J. Phys.*, vol. 89, no. 2, pp. 1–7, 2017.
- [14] S. Chen, W. Li, J. Wu, Q. Jiang, M. Tang, S. Shutts, S. Elliott, A. Sobiesierski, A. Seeds, I. Ross, P. Smowton, and H. Liu, “Electrically pumped continuous-wave III–V quantum dot lasers on silicon,” *Nat. Photonics*, vol. 10, no. 5, pp. 307–311, 2016.
- [15] N. Kasamatsu, T. Kada, A. Hasegawa, Y. Harada, and T. Kita, “Effect of internal electric field on InAs/GaAs quantum dot solar cells,” *J. Appl. Phys.*, vol. 115, no. 8, pp. 1–6, 2014.
- [16] J. Nelson, *The Physics of Solar Cells*. Imperial College Press, London, 2003. ISBN-13 978-1-86094-3492
- [17] A. Martí, L. Cuadra, and A. Luque, “Design constraints of the quantum-dot intermediate band solar cell,” *Phys. E Low-Dimensional Syst. Nanostructures*, vol. 14, no. 1–2, pp. 150–157, 2002.

- [18] X. J. Shang, J. He, H. Wang, M. Li, Y. Zhu, Z. Niu, and Y. Fu, “Effect of built-in electric field in photovoltaic InAs quantum dot embedded GaAs solar cell,” *Appl. Phys. A Mater. Sci. Process.*, vol. 103, no. 2, pp. 335–341, 2011.
- [19] A. Luque, A. Marti, N. Lopez, E. Antolin, E. Canovas, C. Stanley, C. Farmer, and P. Diaz “Operation of the intermediate band solar cell under nonideal space charge region conditions and half filling of the intermediate band,” *J. Appl. Phys.*, vol. 99, no. 9, pp. 1–9, 2006.

## Chapter 5 Investigation into current loss in InAs/GaAs quantum dot solar cells with Si-doped QDs

*It is well known that the employment of Si doping in quantum dots (QDs) can improve the voltage characteristic of quantum dot solar cells (QDSCs). However, this enhancement comes at the expense of the current loss. This chapter investigates the origin of the current loss in Si-doped QDSCs and proposes a method to recover the current loss while maintaining higher voltage. Photoluminescence (PL) measurements reveal that the insertion of additional GaAs layer in the intrinsic region can increase current gain (by 14 %) with minimal voltage loss (< 3 %). The capacitance-voltage measurements indicate that the current recovery is mainly attributed to the increased depletion width.*

## 5.1 Introduction

QDSCs are of great importance since they have the potential to overcome the Shockley-Queisser limit [1]–[3]. Although an introduction of the InAs QDs in GaAs solar cells, which enhances the sub-bandgap absorption, improves the current density characteristic, it suffers from voltage loss [4], [5]. This is because the wetting layer (WL) formed below the QDs increases the dimensionality of the QDs, similar to quantum wells (QWs); hence, the thermal carriers are likely to escape the QDs [6], [7]. In order to tackle this issue, various approaches, including Si-doped QDs, GaAs space layer, AlAs capping layer, and so on, have been explored [8]–[11]. For example, Lam *et al.* reported that a Si doping in InAs QDs showed a voltage recovery—up to 72 % (0.105 V)—of the lost voltage (0.145 V) [10]. However, the effect of the Si-doped QDs in QDSCs is limited because the voltage recovery is achieved at the expense of a depletion width shrinkage [11].

The following equation depicts the relationship between doping levels and depletion width [12]:

$$W = \sqrt{\frac{2\varepsilon}{q} V_{bi} \left( \frac{1}{N_A} + \frac{1}{N_D} \right)} \quad \text{Equation 5.1}$$

where  $W$  is the width of depletion region,  $N_A$  and  $N_D$  are the acceptor and donor concentration, where  $N_D$  can be regarded as the Si doping level in this investigation.  $\varepsilon$  is the permittivity of material (GaAs),  $q$  is electron charge and  $V_{bi}$  is the built-in voltage.

According to the equation, an increase in the doping density—the donor concentration—results in a reduction in  $W$ . As most photon absorption occurs in the depletion region of SCs, a shrinkage in  $W$ , originating from the rising level of Si dopants, causes a decrease of current output of the Si-doped QDSCs [13].

In this work, we aim to further investigate the current loss by Si-doped QDs in QDSCs and propose a solution to use Si-doped QDs without the reduction in  $W$ . First, to confirm the shrinkage of  $W$ , we performed the capacitance-voltage ( $C$ - $V$ ) measurement. The p-i-n solar cell structure can be regarded as an inverted diode and, thus, exhibits capacitor-like

characteristics. Figure 5.1 illustrates the interfaces at each side of the intrinsic region acting as the two parallel plates of the capacitor, and the separation distance ( $d$ ) between the plates is equal to the  $W$ .

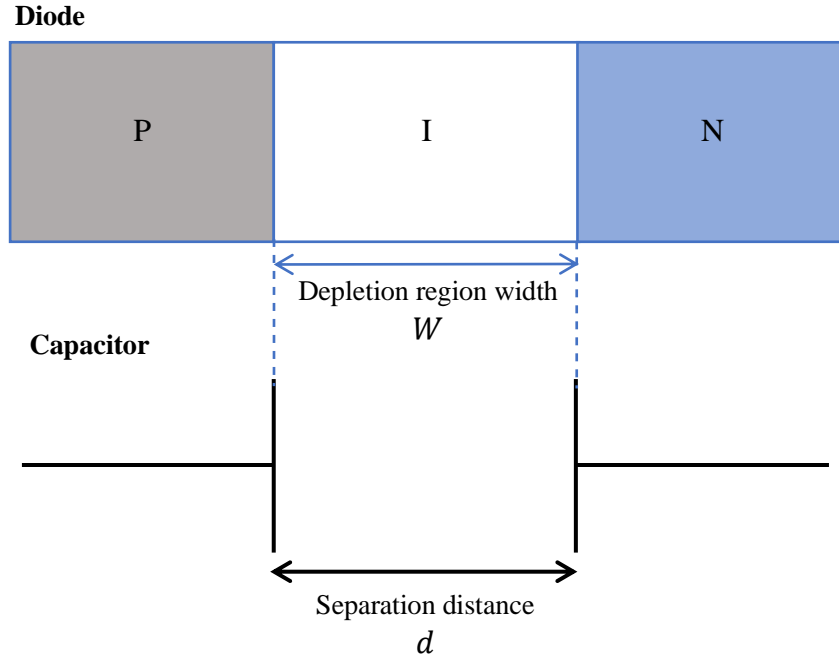


Figure 5.1 Schematic of diode—capacitor equivalency

The following equation expresses the capacitance ( $C$ ) of the solar cell as a function of the separation distance ( $d$ ):

$$C = \frac{\varepsilon A}{d} \quad \text{Equation 5.2}$$

where  $\varepsilon$  is the material permittivity and  $A$  is the area of the solar cell.

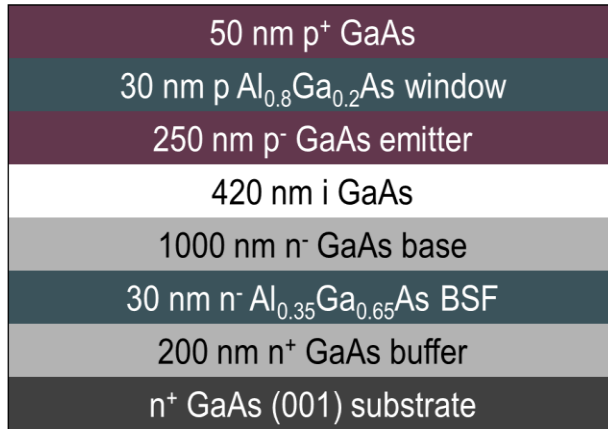
By obtaining the capacitance of the device via  $C$ - $V$  measurements, we calculate the separation distance, namely the depletion region width of each sample, and further examine the alteration between Si-doped and undoped samples to verify the Si-doping-induced shrinkage of  $W$ . Second, to solve the problem of the current density reduction, we proposed a method to extend the effective absorption area, i.e. the depletion region width, by

inserting additional (100 nm) intrinsic layers [14]. The additional intrinsic layers are introduced above, below, and in-between the intrinsic region.

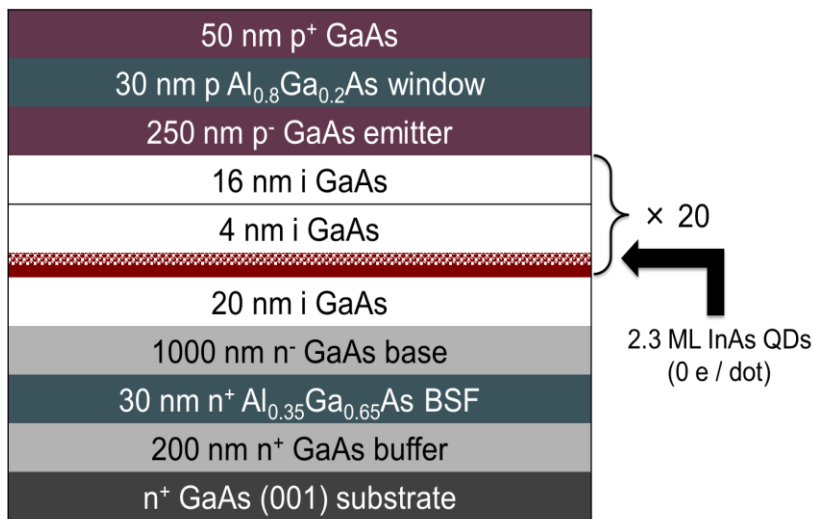
## 5.2 Experimental work

### 5.2.1 Growth

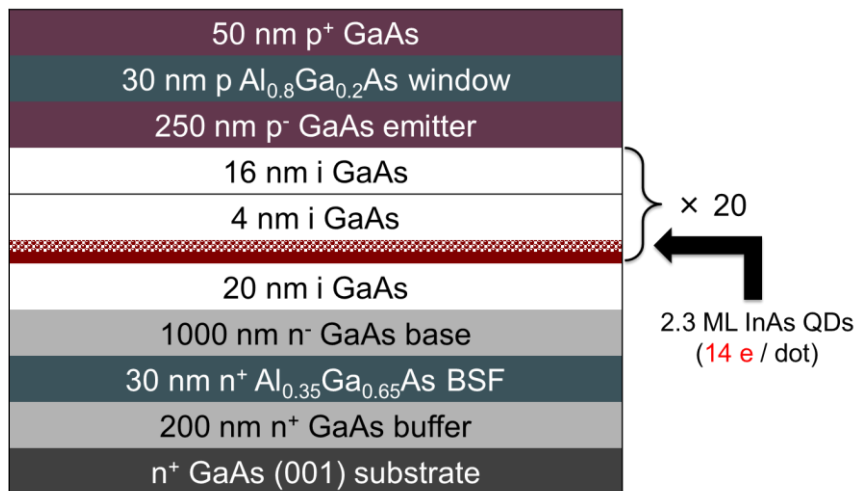
Figure 5.2 illustrates the p-i-n SC structures grown on  $n^+$  GaAs (001) substrates by MBE. In Figure 5.2 (a), the p-i-n structure of GaAs reference SC consists of a 200 nm-thick  $n^+$ -GaAs buffer layer:Si ( $n_d = 1 \times 10^{18} \text{ cm}^{-3}$ ), a 30 nm-thick  $n^+$ -Al<sub>0.35</sub>Ga<sub>0.65</sub>As back surface field (BSF):Si ( $n_d = 1 \times 10^{18} \text{ cm}^{-3}$ ), a 1000 nm-thick n-GaAs base region:Si ( $n_d = 1 \times 10^{17} \text{ cm}^{-3}$ ), a 420 nm-thick i-GaAs intrinsic region, a 250 nm-thick  $p^-$ -GaAs emitter region:Be ( $n_a = 2 \times 10^{18} \text{ cm}^{-3}$ ), a 30 nm-thick p-Al<sub>0.8</sub>Ga<sub>0.2</sub>As window layer:Be ( $n_a = 2 \times 10^{18} \text{ cm}^{-3}$ ), and a 50 nm-thick  $p^+$ -GaAs contact layer:Be ( $n_a = 1 \times 10^{19} \text{ cm}^{-3}$ ). For the comparison, undoped QDSC, Si-doped QDSC, and Si-doped QDSC with additional i-GaAs layer were also grown. Figures (b) and (c) present the conventional undoped and Si-doped QDSCs, respectively. For those samples, a 420 nm-thick i-GaAs layer was replaced by 20 pairs of 2.3 monolayer InAs QDs with a (4 + 16) nm GaAs spacer layers. The QDs were grown under the Stranski-Krastanov mode at a substrate temperature of 500 °C. High growth temperature GaAs spacer layers were applied during the growth to suppress the formation of dislocations [15]. Particularly, for the Si-doped QDSC, a doping density of 14 electrons per dot was chosen based on the previous report in which the best overall efficiency was achieved between 12 – 18 e/dot [10]. Figures (d) – (f) show new designs with the additional intrinsic GaAs layers (100 nm). As shown in Figure (d), the additional intrinsic layer (100 nm) was incremented into each 20 QD layers. In other words, the thickness of each spacer layer was increased by 5 nm (from 16 nm to 21 nm); hence denoted as Si-doped QDSC with 100 nm in spacer. The additional intrinsic layer was also inserted above or below the intrinsic region, respectively, in (e) and (f) with the nomenclature of Si-doped QDSC with 100 nm emitter or base.



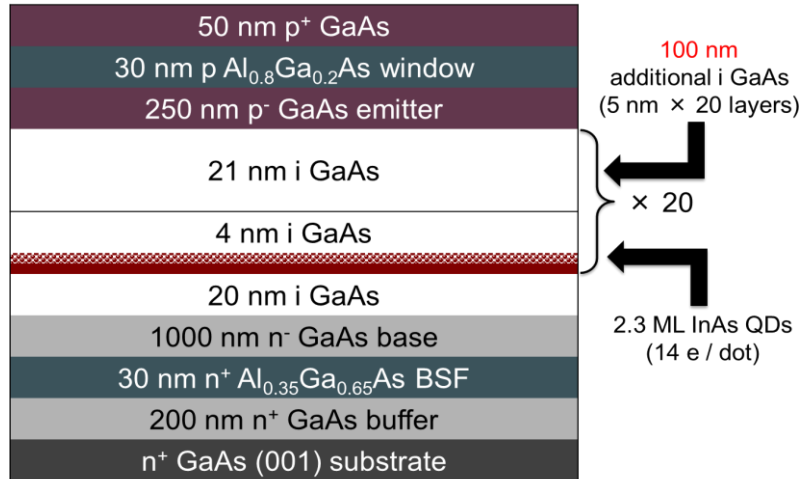
**(a) GaAs Ref SC**



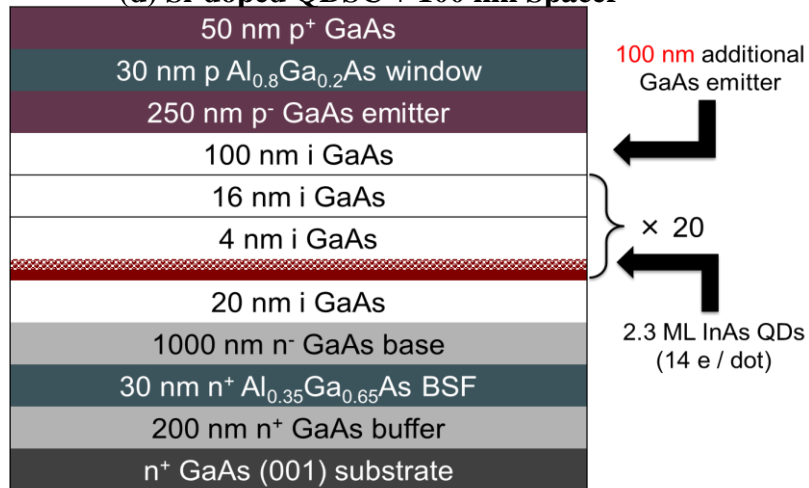
**(b) Undoped QDSC**



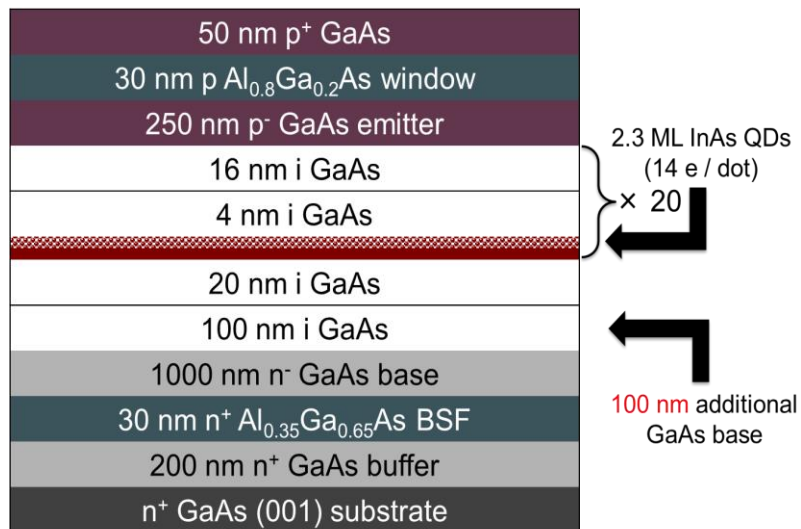
**(c) Si-doped QDSC**



**(d) Si-doped QDSC + 100 nm Spacer**



**(e) Si-doped QDSC + 100 nm Emitter**



**(f) Si-doped QDSC + 100 nm Base**

Figure 5.2 Schematics of the p-i-n solar cells

### 5.2.2 Fabrication

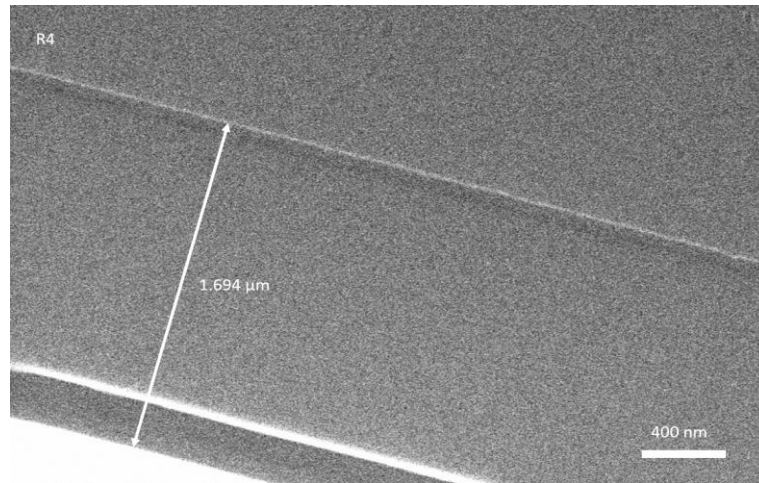
Post MBE growth, samples were cleaned ultrasonically with acetone and isopropanol solutions for 5 minutes each. Surface oxides were removed by using a diluted ammonia solution (1:19) for 50 seconds. A Ni/AuGe/Ni/Au (10/100/30/300 nm) scheme was thermally evaporated onto the backside of the sample to form n-type contact. A 200 nm-thick Au-Zn (95:5) alloy was thermally evaporated through a shadow mask of SC grid patterns to form the p-type contact. In order to form ohmic contact, thermal annealing was applied to all samples at 400 °C for 60 seconds [16]. Note that neither an anti-reflection coating nor surface passivation was applied.

### 5.2.3 Characterisation

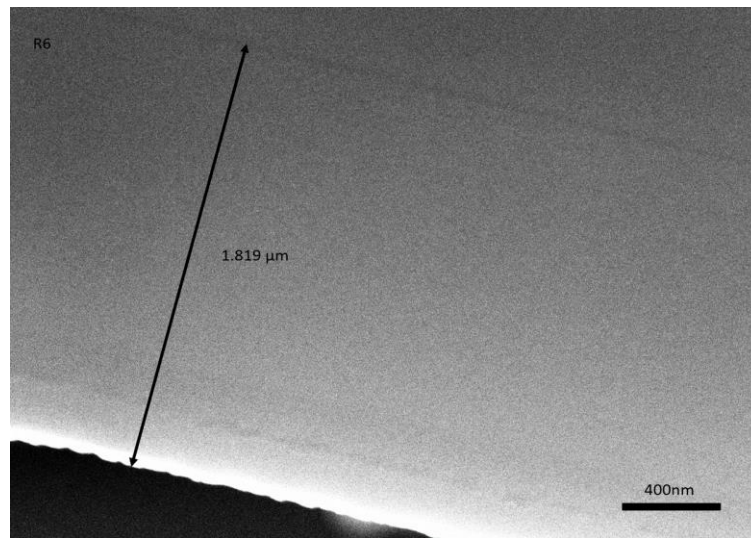
For the characterisation, temperature-dependent and power-dependent PL spectra were obtained using a diode-pumped solid-state laser at 2.33 eV (532 nm) excitation power. The temperature was controlled (from 10 K to 300 K) by a Helium-cooled cryostat during the measurements. Current density-voltage ( $J$ - $V$ ) characteristics were measured by a calibrated solar simulator with a xenon lamp under one sun (AM 1.5G) illumination at room temperature. Data was collected by a sourcemeter and processed using software to plot the  $J$ - $V$  graph. External quantum efficiency (EQE) measurements were carried out using the light beam from a halogen lamp, which are passed into a monochromator. The monochromatic beams were calibrated with a GaAs photo-diode and the data was analysed using a software to plot the EQE spectrum. The  $C$ - $V$  characteristics were measured using a four-point probe station connected to the sourcemeter.

## 5.3 Results and Discussion

### 5.3.1 SEM



**(a) Si-doped QDSC**



**(b) Si-doped QDSC + 100 nm  
Emitter**

Figure 5.3 Cross-sectional SEM images of (a) Si-doped QDSC and (b) Si-doped QDSC + 100 nm Emitter

To confirm the actual thickness of the samples with additional intrinsic layer, scanning electron microscopy (SEM) measurement was conducted. Figure 5.3 illustrates the cross-sectional SEM images of the Si-doped QDSC without/with a 100 nm-thick additional intrinsic layer. The lengths between the surface and the AlGaAs BSF for the samples

without/with the additional intrinsic layer were measured to be 1.694  $\mu\text{m}$  (Figure 5.3(a)) and 1.819  $\mu\text{m}$  (Figure 5.3(b)), respectively. This confirms that the thickness of the grown sample is accurate, and the additional intrinsic layer is 100 nm.

### 5.3.2 J-V

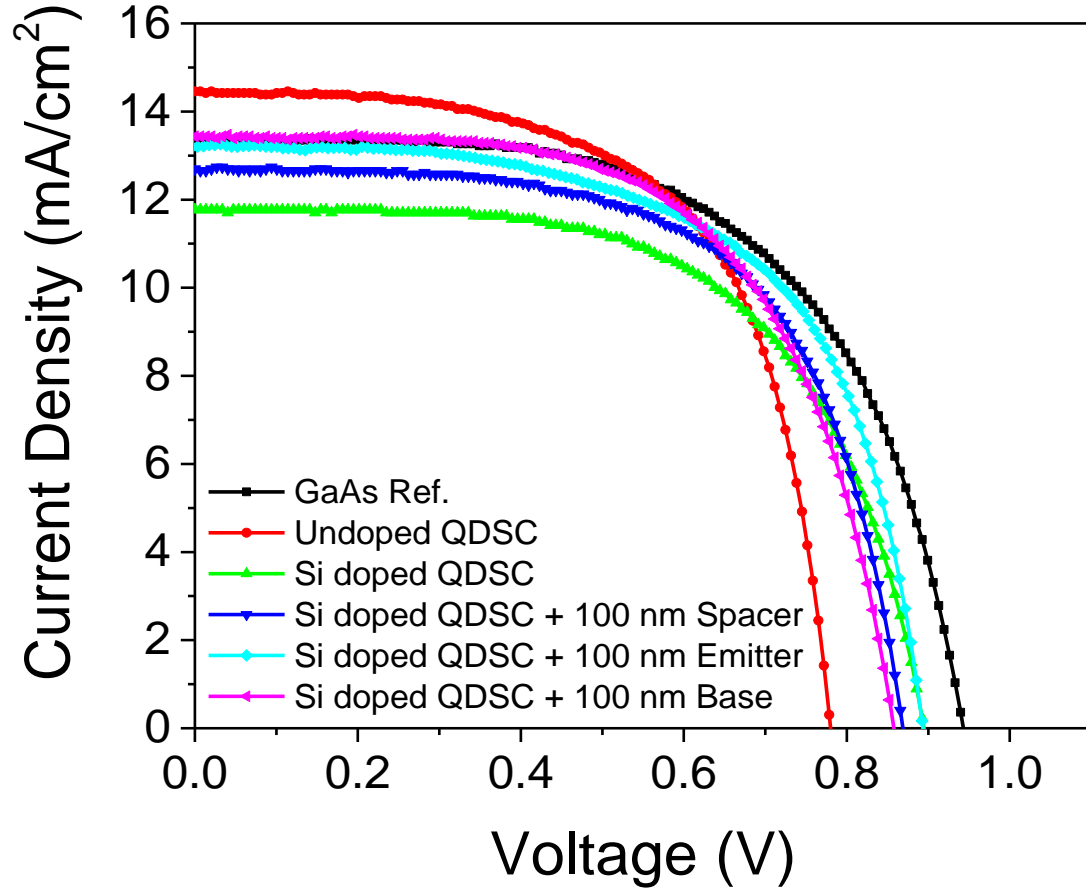


Figure 5.4 J-V characteristics of GaAs SC and QDSCs

Device	$J_{sc}$ (mA/cm <sup>2</sup> )	$V_{oc}$ (V)	FF (%)	$\eta$ (%)
GaAs	13.37	0.942	59.70	7.52
Undoped	14.42	0.779	62.73	7.05
Si doped	11.74	0.894	61.06	6.41
Thick Spacer	12.70	0.869	63.09	6.96
Thick Emitter	13.20	0.892	60.52	7.13
Thick Base	13.45	0.857	61.47	7.09

### Table 5.1 Parameters of $J$ - $V$ characteristics

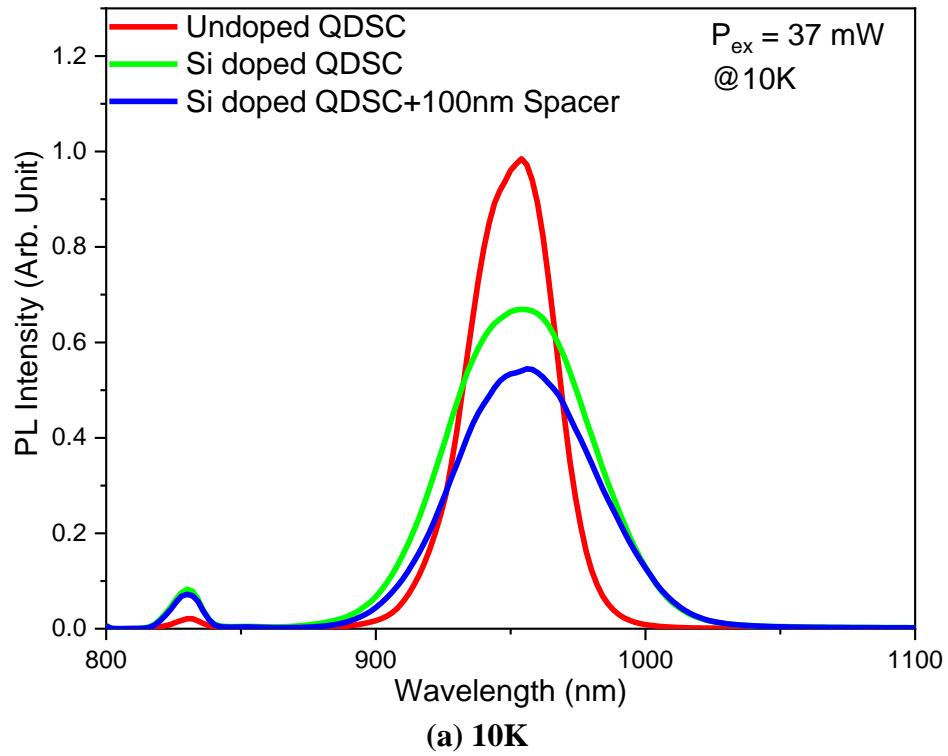
Figure 5.4 plots the  $J$ - $V$  characteristic curves and the parameter data are included in Table 4.1. The GaAs ref SC achieved a short-circuit current density ( $J_{sc}$ ) of 13.37 mA/cm<sup>2</sup> and an open-circuit voltage ( $V_{oc}$ ) of 0.942 V, thereby scoring an overall conversion efficiency ( $\eta$ ) of 7.52%. For the undoped QDSC, the  $J_{sc}$  increased by 1.05 mA/cm<sup>2</sup>, but the  $V_{oc}$  decreased significantly to 0.779 V, resulting in a poorer  $\eta$  of 7.05 %. This alteration has been observed in the previous chapter, and to recap, it is caused by the thermal communication between the intermediate band (IB) and conduction band (CB) through the WLs. In other words, the continuous energy levels within the WLs provide carriers with the multiple paths for the transition, reducing the energy bandgap between IB and CB. As a result, carriers with lower energy can travel towards the CB, which decreases the voltage output. For the Si-doped QDSC sample, the voltage recovery effect was observed (from 0.779 V to 0.894 V), but the current density was undermined (from 14.42 mA/cm<sup>2</sup> to 11.74 mA/cm<sup>2</sup>). This negative outcome is attributed to the shortening of the depletion width by Si doping in InAs QDs [11].

To regain the lost current density, the additional 100 nm-thick intrinsic layers were inserted to three different positions of Si-doped QDSCs, i.e. the spacer layer, emitter or base region. All thicker Si-doped QDSCs achieved higher current density than that of the typical Si-doped QDSC, at least 12.70 mA/cm<sup>2</sup>, while maintaining the voltage output in the range of 0.857 V to 0.892 V, at most 4 % less than 0.894 V. Hence, it was confirmed that the additional 100 nm intrinsic layer has indeed regained the lost current density without compromising the voltage output.

Among the thicker QDSCs, thick emitter and thick base QDSCs achieved similar current density of 13.20 and 13.45 mA/cm<sup>2</sup>, respectively. This demonstrates that inserting the additional intrinsic layer (as a bulk) above or below the QD layers has very similar impact on the current output and potentially on the depletion region width. On the other hand, the thick spacer QDSC produced a less  $J_{sc}$  of 12.69 mA/cm<sup>2</sup> than those of other two thick QDSCs, which falls short of expectation. We have predicted that incrementing the

additional 100 nm layer into 20 layers of spacer layer would improve the QD quality as well as the effective absorption, and, thus, achieve the highest current density of all [15].

### 5.3.3 PL



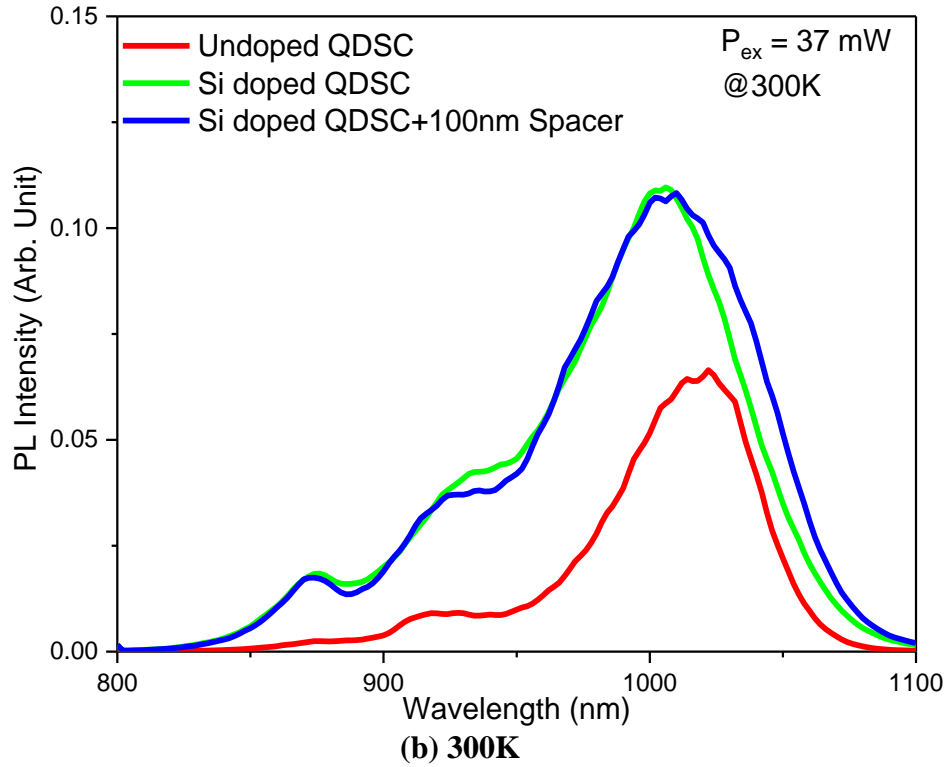


Figure 5.5 PL spectra of QDSCs at (a) 10 K and (b) 300 K

To find out the cause of the unexpected outcome, PL measurements were carried out. The PL measurement examines the optical characteristics of the material; here, we specifically examine the QDs quality of the undoped QDSC, Si doped QDSC and thick spacer QDSC. Figure 5.5 illustrates the PL spectra of the QDSCs at (a) 10K and (b) 300K. At 10K, the Si doped QDSC shows similar peak position at 955 nm and full width half maximum (FWHM) of 59 nm to the thick spacer QDSC. At 300K, these two samples also show similar attributes, including the peak position at 1010 nm and FWHM of 65–70 nm. Since the changes of the optical behaviour under rising temperature were identical, we conclude that increasing each spacer layer by 5 nm neither altered the QD size nor changed the QD uniformity. This is because the increase in thickness by 5 nm may not be large enough to show a clear improvement or the quality of the QDs might already reach optimum level at 16 nm spacer layer. Consequently, we no longer expect the thick spacer QDSC to achieve higher current density, but it should at least achieve similar current density to the other thicker QDSCs.

### 5.3.4 EQE

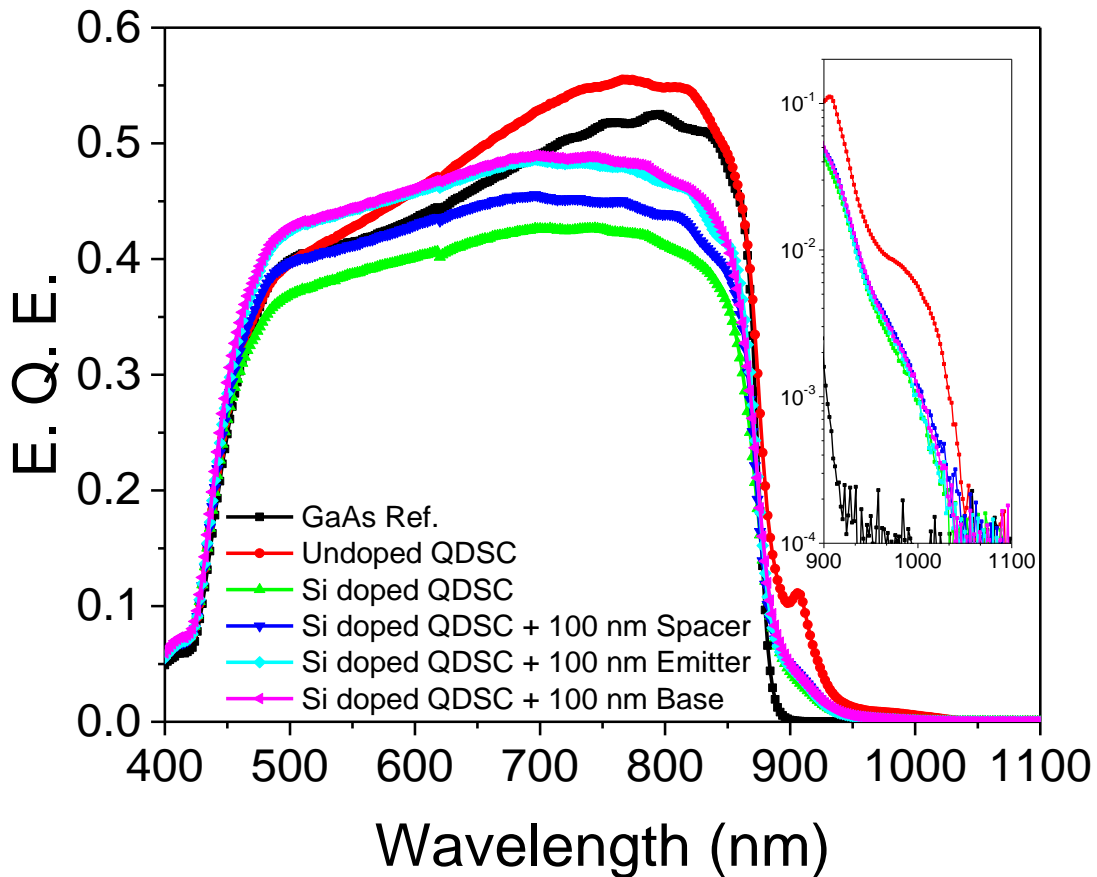


Figure 5.6 EQE spectra of GaAs SC and QDSCs

Figure 5.6 presents the EQE spectra of the QDSCs, and the QD absorption around the sub-bandgap region (900 nm – 1100 nm) is shown in the inset of Figure 5.6. The EQE measurements identify which range of spectrum the current originates from and the amount of current at the particular wavelength. All samples experience a sharp drop at 870 nm which corresponds to the GaAs bandgap. Within the inter-bandgap region (400 nm to 870 nm) all samples have an increasing trend of EQE. In particular, the GaAs ref SC and the undoped QDSC have a steeper gradient compared to the Si-doped QDSCs. In the sub-bandgap region, the GaAs ref SC produces a flat output whereas the undoped QDSC shows a strong peak at 930 nm. All Si-doped QDSCs exhibit an intermediate output level. The

EQE results are consistent with the  $J$ - $V$  characteristics. The undoped QDSC obtained stronger EQE than GaAs ref SC; therefore, the current density is higher. However, the peak at 930 nm revealed the weakness of thermal communication via the WL, resulting in a low voltage output.

Among the Si-doped QDSCs, all three thicker Si-doped QDSCs achieved higher EQE than that of the regular Si-doped QDSCs, with thick emitter and thick base SCs producing the highest EQE. This is in agreement with the current density ranking in  $J$ - $V$  characteristics. As shown in the inset of Figure 5.6 which depicts the QD absorption, moreover, all Si-doped QDSCs exhibit very similar trends, indicating that the additional intrinsic layers do not improve the QD quality. Hence, the EQE results implied that the current shortfall originated from the inter-bandgap material (GaAs) qualities rather than the QD qualities.

### 5.3.5 C-V

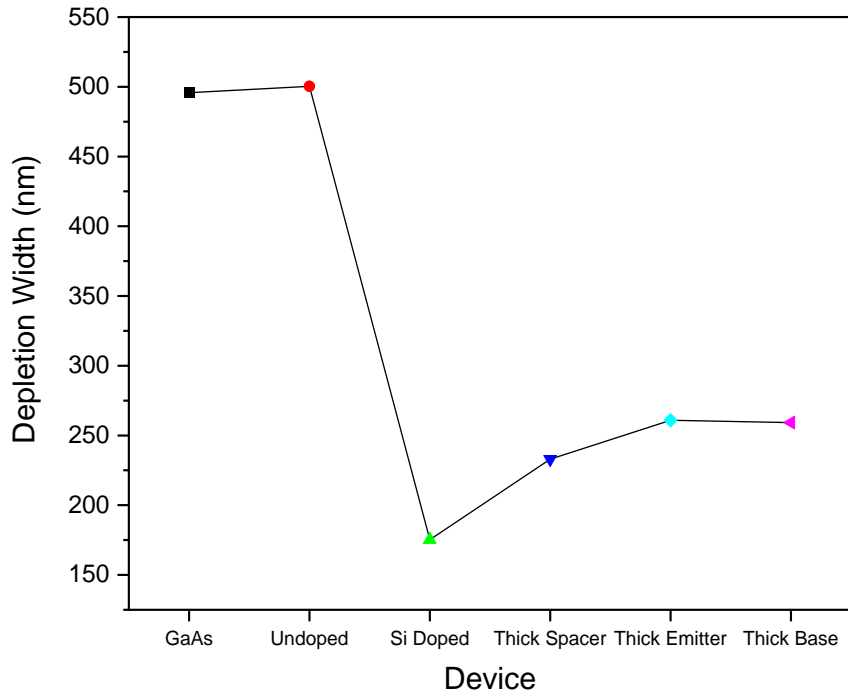


Figure 5.7 Depletion width of the GaAs SC and QDSCs

Device	Capacitance (nF)	Area (cm <sup>2</sup> )	Depletion width (nm)
GaAs	6.53	0.336	496
Undoped	6.76	0.351	500
Si doped	19.1	0.348	175
Thick Spacer	12.6	0.306	233
Thick Emitter	11.5	0.311	261
Thick Base	13.8	0.371	259

Table 5.2 Parameters of C-V characteristics

To confirm our hypothesis on the impact of depletion width, the *C-V* characteristics were measured. Figure 5.7 illustrates the depletion width of the SCs and Table 2 presents the parameters. Both the GaAs SC and undoped QDSC have 500 nm depletion width. In contrast, a 14 e/dot Si-doping significantly reduced the depletion width. Particularly, the conventional Si-doped QDSC experienced the largest reduction in depletion width by 320 nm. We anticipated that increasing the donor concentration would shrink the width, but such a large amount of the shrinkage (65%) is beyond our anticipation.

The thick spacer, emitter and base QDSCs have wider depletion widths of 233, 261 and 259 nm, respectively, than that of the typical Si-doped QDSC (175 nm). Although the width extensions are less than the expected width (100 nm), the results are in agreement with the *J-V* analysis that the inclusion of intrinsic layer above or below the QD layer has the same impact on the width. Furthermore, the depletion width of the thick spacer QDSC increased only by 58 nm, which is likely to contribute to the reduced current density of this device. However, the reason for the shorter extension width of thick spacer QDSC remains unclear. Our assumption is that the alternating layers of QDs and the thicker spacer layers causes the carriers to be less mobile during carrier transportation. Also, in terms of the material quality, growing 100 nm-thick layer at once would produce better quality of GaAs layers than repeating the growth of 5 nm layer by 20 times; thus, the better quality of the thick emitter and base QDSCs resulted in higher carrier mobility compared with thick spacer QDSC.

Numerical data also showed that the 14 e/dot Si-doping resulted in a shortening of depletion width by 320 nm (65 %) and current density loss of 2.68 mA/cm<sup>2</sup> (19 %). The employment of the additional intrinsic layers recovered the current density up to 1.71 mA/cm<sup>2</sup>, corresponding to 64 % of the lost current density. Based on the extrapolation method, an additional 200 – 300 nm intrinsic layer should be able to recover 100% of the lost current; thus, the drawback of using Si-doping in QDSCs could be solved. While this study strongly recommends deploying thicker intrinsic layers in future investigations, we should also be aware that over-extending the depletion width may weaken the strength of internal electric field and increase the transportation length, causing the current density to be reduced rather than increased.

## 5.4 Discussions

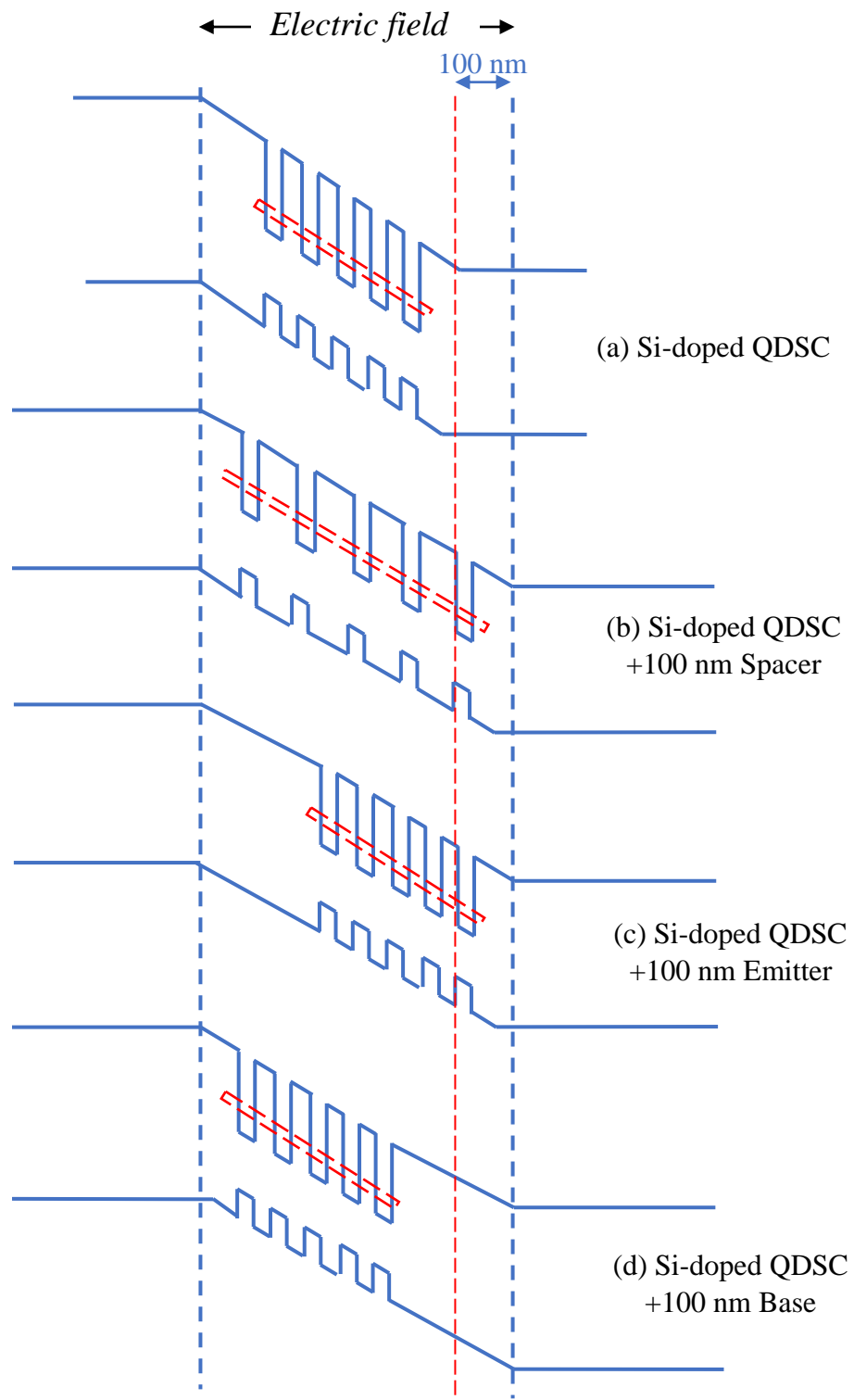


Figure 5.8 A Simplified schematic diagram of the energy band of (a) Si-doped, (b) Thick spacer, (c) Thick emitter and (d) Thick base QDSCs

Figure 5.8 illustrates the energy band diagram of the samples. Sample (a) is 100 nm shorter than samples (b)—(d) marked by the red dotted line which corresponds to the grown structures. Larger number of photons can be absorbed within the 100 nm layer, hence, produce a higher current output.

Sample (a), (c) and (d) have the same length of QD regions whereas (b) has a slightly wider spread of the QD region (shown as the red dotted boxes). Sample (c) and (d) differ from the location of the 100 nm layer which may cause different current output due to different carrier mobilities. Holes have lower mobilities compared to electrons so if the 100 nm layer is added to the emitter region, losses of holes could occur at the region. This was, however, not the case for this investigation, current outputs from both sample (c) and (d) are very similar. This can be explained by the internal electric field, if both samples' 100 nm layers are within the effect of the electric field, carriers are driven out of the region without the need to consider carrier mobilities. Therefore, this finding indirectly proves that the electric field effect covers the 100 nm layer for both samples.

Sample (b) has the most complex band structure and has been causing confusions during the data analysis. It should benefit from the electric field effect analogous to sample (c) and (d) i.e. carrier transport aided by the drift force. A thicker spacer layer, in theory, should also improve the QD matrix quality. But the outcome falls short of expectation. The author can only think of one possible explanation which question the quality of the GaAs material. Growing 20 layers of 5 nm-thick GaAs material result in *slightly* less quality compared to the growth of 1 layer of 100 nm-thick GaAs material (even though MBE is extremely accurate). Furthermore, the author has thought of a method to prove his deduction, which is to grow samples with less increments, for example, grow 2 layers of 50 nm-thick GaAs material above and below the QD matrix, or grow 10 layers of 10 nm-thick spacer layer correctly incorporated into 20 layers of QDs. The sample with more layers is expected to have an inferior performance i.e. 10 layers by 10 nm-thick is worse than 2 layers by 50 nm-thick.

## 5.5 Conclusion

The purpose of this study is to verify the cause of current density reduction by Si-doping and propose a method to solve this issue. Three novel device structures with thicker intrinsic layers are designed and characterised. Based on the  $J$ - $V$ , PL, and EQE measurements, assumptions about the origin of Si-doping-induced current loss were confirmed. In particular, the  $C$ - $V$  characteristics provide clear evidence of the lengthening of the shortened depletion width by Si doping after the insertion of additional intrinsic layer. The Si-doped QDSC with additional 100 nm intrinsic layer in emitter region has achieved 86 nm extension in depletion width and recovered the lost current density by 64%. Further analysis suggests thicker intrinsic layers may result in stronger recovery and a 300 nm intrinsic layer may be able to recover all the lost current without compromising voltage loss.

## 5.6 References

- [1] W. Shockley and H. J. Queisser, “Detailed balance limit of efficiency of p-n junction solar cells,” *J. Appl. Phys.*, vol. 32, no. 3, pp. 510–519, Mar. 1961.
- [2] A. Luque and A. Martí, “Increasing the Efficiency of Ideal Solar Cells by Photon Induced Transitions at Intermediate Levels,” *Phys. Rev. Lett.*, vol. 78, no. 26, pp. 5014–5017, Jun. 1997.
- [3] A. Marti, L. Cuadra, and A. Luque, “Quantum dot intermediate band solar cell,” *Conf. Rec. IEEE Photovolt. Spec. Conf.*, Anchorage AK USA, vol. 2000-Jan, pp. 940–943, 2000.
- [4] P. Frigeri and S. Franchi, “Carrier thermal escape and retrapping in self-assembled quantum dots,” *Phys. Rev. B - Condens. Matter Mater. Phys.*, vol. 60, no. 11, pp. 8276–8283, Sep. 1999.
- [5] E. Antolín, A. Marti, C. Farmer, P. Linares, E. Hernandez, A. Sanchez, T. Ben, S. Molina, C. Stanley, and A. Luque, “Reducing carrier escape in the InAs/GaAs quantum dot intermediate band solar cell,” *J. Appl. Phys.*, vol. 108, no. 6, p. 064513, Sep. 2010.
- [6] Y. Dai, C. G. Bailey, C. Kerestes, D. V. Forbes, and S. M. Hubbard, “Investigation of carrier escape mechanism in InAs/GaAs quantum dot solar cells,” *Conf. Rec. IEEE Photovolt. Spec. Conf.*, Austin TX USA, pp. 39–44, 2012.
- [7] D. G. Sellers, S. Polly, S. M. Hubbard, and M. F. Doty, “Analyzing carrier escape mechanisms in InAs/GaAs quantum dot p-i-n junction photovoltaic cells,” *Appl. Phys. Lett.*, vol. 104, no. 22, p. 223903, 2014.
- [8] S. Asahi, H. Teranishi, N. Kasamatsu, T. Kada, T. Kaizu, and T. Kita, “Suppression of thermal carrier escape and efficient photo-carrier generation by two-step photon absorption in InAs quantum dot intermediate-band solar cells using a dot-in-well structure,” *J. Appl. Phys.*, vol. 116, no. 6, p. 063510, 2014.

- [9] F. K. Tutu, P. Lam, J. Wu, N. Miyashita, Y. Okada, K. Lee, N. Ekins-Daukes, J. Wilson, and H. Liu, "InAs/GaAs quantum dot solar cell with an AlAs cap layer," *Appl. Phys. Lett.*, vol. 102, no. 16, p. 163907, 2013.
- [10] P. Lam, S. Hatch, J. Wu, M. Tang, V. Dorogan, Y. Mazur, G. Salamo, I. Ramiro, A. Seeds, and H. Liu, "Voltage recovery in charged InAs/GaAs quantum dot solar cells," *Nano Energy*, vol. 6, pp. 159–166, 2014.
- [11] D. Kim, M. Tang, J. Wu, S. Hatch, Y. Maidaniuk, V. Dorogan, Y. Mazur, G. Salamo, and H. Liu, "Si-Doped InAs/GaAs Quantum-Dot Solar Cell with AlAs Cap Layers," *IEEE J. Photovoltaics*, vol. 6, no. 4, pp. 906–911, 2016.
- [12] J. Nelson, *The Physics of Solar Cells*. Imperial College Press, London, 2003. ISBN-13 978-1-86094-3492
- [13] W. W. Gärtner, "Depletion-layer photoeffects in semiconductors," *Phys. Rev.*, vol. 116, no. 1, pp. 84–87, Oct. 1959
- [14] T. Taima, M. Chikamatsu, Y. Yoshida, K. Saito, and K. Yase, "Effects of intrinsic layer thickness on solar cell parameters of organic p-i-n heterojunction photovoltaic cells," *Appl. Phys. Lett.*, vol. 85, no. 26, pp. 6412–6414, 2004.
- [15] H. Y. Liu, I. Sellers, M. Gutierrez, K. Groom, W. Soong, M. Hopkinson, J. David, R. Beanland, T. Badcock, D. Mowbray, and M. Skolnick, "Influences of the spacer layer growth temperature on multilayer InAs/GaAs quantum dot structures," *J. Appl. Phys.*, vol. 96, no. 4, pp. 1988–1992, Aug. 2004.
- [16] P. Lam, J. Wu, S. Hatch, D. Kim, M. Tang, H. Liu, J. Wilson, and R. Allison, "Effect of rapid thermal annealing on InAs/GaAs quantum dot solar cells," *IET Optoelectron.*, vol. 9, no. 2, pp. 65–68, Apr. 2015.

## Chapter 6 1.7 eV Al<sub>0.22</sub>Ga<sub>0.78</sub>As solar cell on GaAs substrate

*This chapter aims to achieve the growth of the optimal IBSC bandgap configuration (1.95 eV, 1.24 eV and 0.71 eV) starting from the growth of Al<sub>x</sub>Ga<sub>1-x</sub>As host material at Al composition of 22 % (x=0.22). The benefits of deploying AlGaAs host material instead of GaAs include bandgap tunability (1.42 eV to 2.16 eV) and suppression of thermal carrier escapes. The temperature condition has been investigated by growing six samples at 550 °C, 570 °C, 590 °C, 610 °C, 630 °C and 650 °C. Photoluminescence, external quantum efficiency and current density versus voltage characteristics were measured to examine the performance. Photoluminescence and external quantum efficiency data show a bandgap at 750 nm wavelength which corresponds to 1.65 eV; hence, the actual Al composition is less than 22 %. JV results indicate a voltage loss for all samples which could be caused by an error during the fabrication process. Methods to address the problem have been proposed for future device processing.*

## 6.1 Introduction

In 1997, Luque and Marti proposed the concept of intermediate band solar cell (IBSC) and presented a list of ideal conditions to realise the IBSC [1]. One of the ideal conditions is the optimal bandgap configuration: 1.95 eV between CB and VB, 1.24 eV between VB and IB and 0.71 eV between IB and CB [2]. In this regard, the InAs QD/GaAs (1.1 eV/1.42 eV) material system is not the ideal system to match the optimal bandgap [3]. A fully optimised bandgap can theoretically achieve 63.2 % SC efficiency compared to the Shockley-Queisser limit of 33.1 % [4], [5]. Despite this mismatch with the optimal bandgap, the InAs/GaAs-based material system has long been employed for IBSC since the early stage, owing to its well-established growth technique [6].

However, the performance of the InAs/GaAs-based IBSCs is still unsatisfactory and unlikely to exceed the Shockley-Queisser limit in a foreseeable future. One of the reasons arises from the thermal carrier escape which causes a drastic reduction in voltage output [7]. Due to the characteristics of Stranski-Krastanov (SK) growth mode, a wetting layer (WL) is inevitably formed underneath the QDs, which undermines the benefit of zero-dimensional QD structure. The WL exhibits a two-dimensional quantum well structure which has continuous energy levels, and this band configuration promotes thermal carrier transition between the IB and CB [8]. As a result, electrons excited from VB to IB can be pumped into CB without absorbing another photon and, hence, effective bandgap is reduced along with voltage output [9]. This problem has been addressed by numerous solutions, for example, AlAs cap layers and negatively charged QDs [10], [11]. The essence of the approach is to create energy barriers at the interfaces so that the effective bandgap is recovered.

An alternative method to increase the effective bandgap is deploying wide bandgap host materials [12].  $\text{Al}_x\text{Ga}_{1-x}\text{As}$ , which has a bandgap tunability between 1.42 eV and 2.16 eV, is a flexible material to implement the host material. An Al composition of 25 % in AlGaAs material can increase the bandgap from 1.42 eV to 1.7 eV and raise the thermal activation energy by 200% (110 meV to 360 meV). As a result, thermal carrier escape can be

suppressed without a voltage loss [13]. Furthermore, an Al composition of 42% has a bandgap of 1.95 eV which matches the optimal bandgap model of IBSC. Hence,  $\text{Al}_x\text{Ga}_{1-x}\text{As}$  material has great potentials to realise the IBSC. Unfortunately, the growth of high Al compositions and fabrication of AlGaAs SCs is challenging [14]. The oxygen-induced deep level Al-O defects result in poor host material quality prior to the inclusion of QD arrays [15]. Consequently, a significant reduction in minority carrier diffusion length and carrier lifetime has been observed in SC devices.

In this project, we investigate the solar cell performance of  $\text{Al}_x\text{Ga}_{1-x}\text{As}$  with  $x=0.22$ . This amount of Al composition only raises the material bandgap to 1.7 eV. However, recent studies have reported that minimum amount of oxygen related defects can be achieved under this Al composition [16]. Furthermore, the results hinted that increasing the growth temperature ( $>580$  °C) can improve the material quality by mitigating the oxygen contamination. Based on this result, six samples were grown at 550 °C, 570 °C, 590 °C, 610 °C, 630 °C and 650 °C. Samples were subsequently fabricated into solar cell devices and their performance were characterised. Noted that this batch of samples does not contain any QDs initially, both the deep level defects and QD defects are reflected as point defects and, hence, it is difficult to distinguish each impact. Therefore, the inclusion of QDs is postponed to the next growth phase.

## 6.2 Experimental work

### 6.2.1 Growth

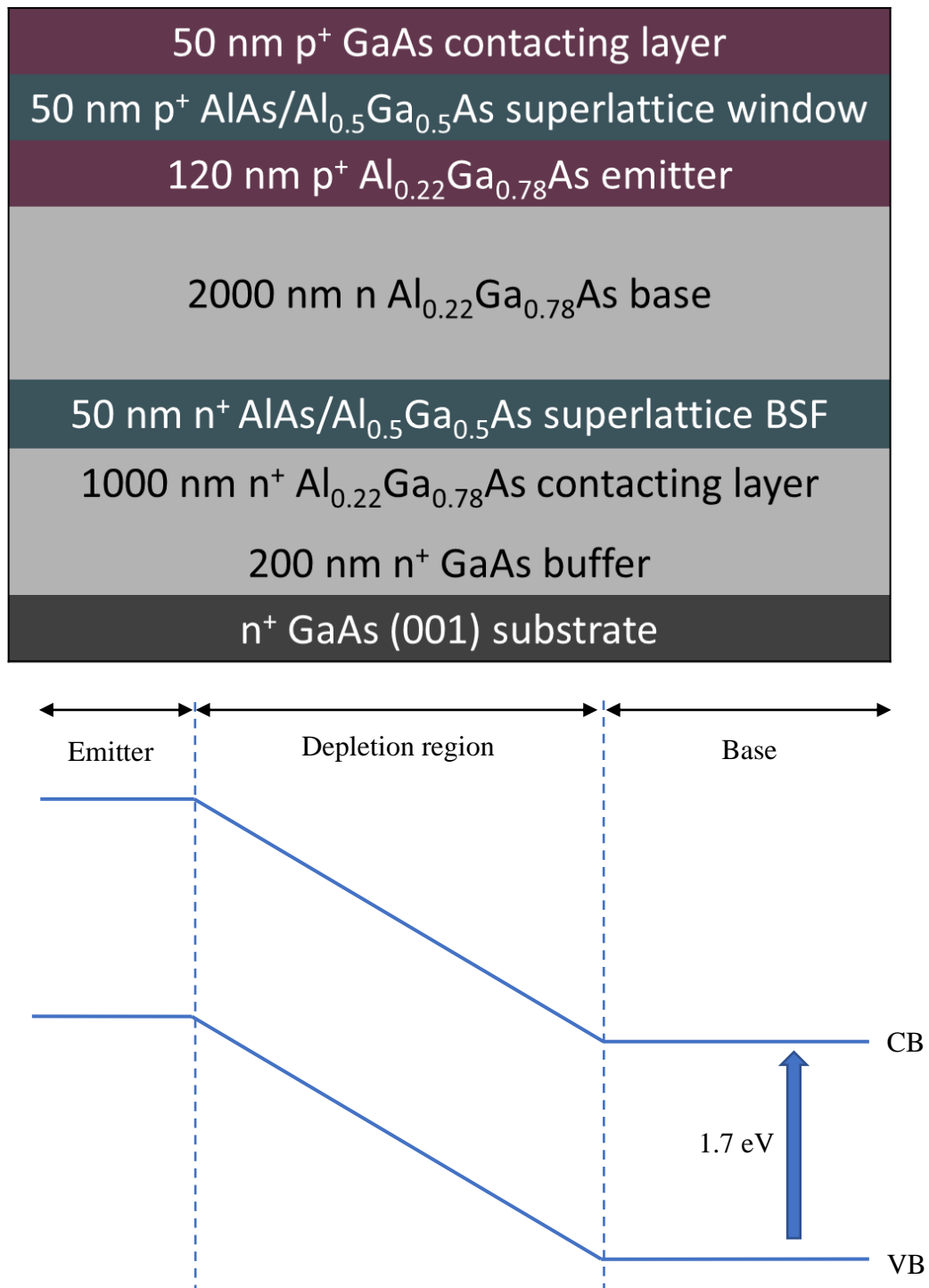


Figure 6.1 SC structure of  $\text{Al}_{0.22}\text{Ga}_{0.78}\text{As}$  (with no QDs) and the corresponding energy band diagram

Figure 6.1 shows schematic illustration of Al<sub>0.22</sub>Ga<sub>0.78</sub>As-based solar cell (SC) grown by MBE. To optimise the growth temperature, the SCs were grown at 550 °C, 570 °C, 590 °C, 610 °C, 630 °C and 650 °C. The growth temperature was monitored by a thermocouple and an external infrared pyrometer in order to estimate the real growth temperature.

The structure of the cells contains a 200 nm n<sup>+</sup>-GaAs buffer layer with Si doping level of 1.4×10<sup>18</sup> cm<sup>-3</sup>, a 1000 nm n<sup>+</sup>-Al<sub>0.22</sub>Ga<sub>0.78</sub>As contacting layer with Si doping level of 1.1×10<sup>18</sup> cm<sup>-3</sup>, a 50 nm n<sup>+</sup> AlAs/Al<sub>0.5</sub>Ga<sub>0.5</sub>As superlattice back surface field (BSF) with Si doping level of 1×10<sup>18</sup> cm<sup>-3</sup>, a 2000 nm n-Al<sub>0.22</sub>Ga<sub>0.78</sub>As base layer with Si doping level of 2×10<sup>17</sup> cm<sup>-3</sup>, a 120 nm p<sup>+</sup>-Al<sub>0.22</sub>Ga<sub>0.78</sub>As emitter layer with Be doping level of 1×10<sup>18</sup> cm<sup>-3</sup>, a 50 nm p<sup>+</sup>-AlAs/Al<sub>0.5</sub>Ga<sub>0.5</sub>As superlattice window layer with Be doping level of 4×10<sup>18</sup> cm<sup>-3</sup> and a 50 nm p<sup>+</sup>- GaAs contacting layer with Be doping level of 1×10<sup>19</sup> cm<sup>-3</sup>. Noted that the n-type contacting layer is 1000 nm-thick so that, during fabrication, the difficulty of mesa-etching is reduced. Moreover, a p-type GaAs, instead of AlGaAs, contacting layer was grown to prevent the underlying layers from oxidation.

### 6.2.2 Fabrication

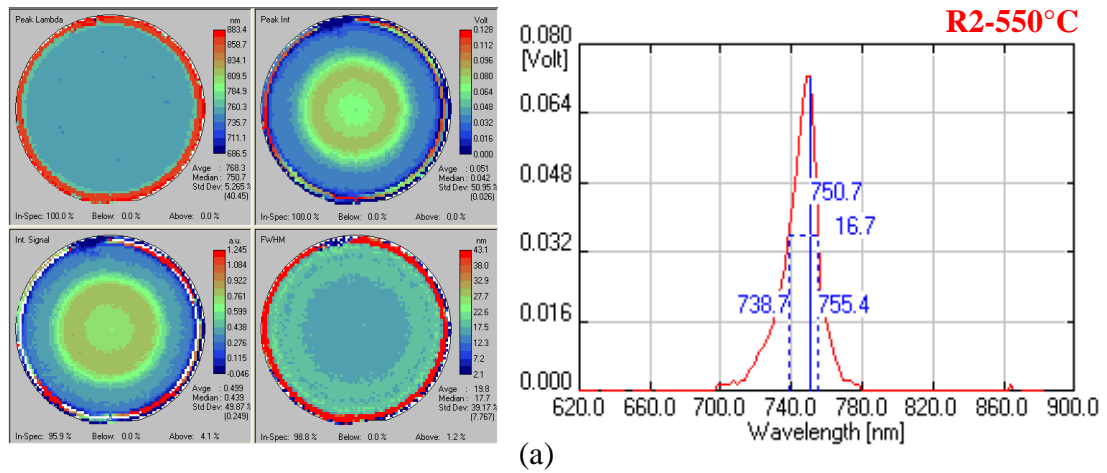
Post MBE-growth, samples were fabricated into SC devices under cleanroom environment. Prior to photolithography, samples were cleaved into quarter-wafers and cleaned with acetone and isopropanol solutions for 5 minutes, respectively. The first photolithography pattern isolates the sample into 3×3 mm solar cell mesas. The mesas were defined by wet etching using the H<sub>2</sub>SO<sub>4</sub>:H<sub>2</sub>O<sub>2</sub>:H<sub>2</sub>O (1:10:80) etchant solution. The depth of the mesa etching is about 2700 nm where the n-type contacting layer is exposed. The second and third photolithography pattern defines the n-type mesa contacts and p-type front SC grids, respectively. Before metallisations, samples were deoxidised using the NH<sub>4</sub>OH:H<sub>2</sub>O (1:19) solution for 60 seconds. N-type metal contact, which consists of a Ni/AuGe/Ni/Au (10/100/30/300 nm) scheme, is thermally evaporated onto the mesa region. P-type metal contact, which consists of a Ti/Pt/Au (20/50/400 nm) scheme, is magnetically sputtered onto the front grid region. To enhance the formation of ohmic contact, thermal annealing was performed at 400°C for 60 seconds. Noted that anti-reflection coatings or surface passivation are not applied to the samples.

### 6.2.3 Characterisation

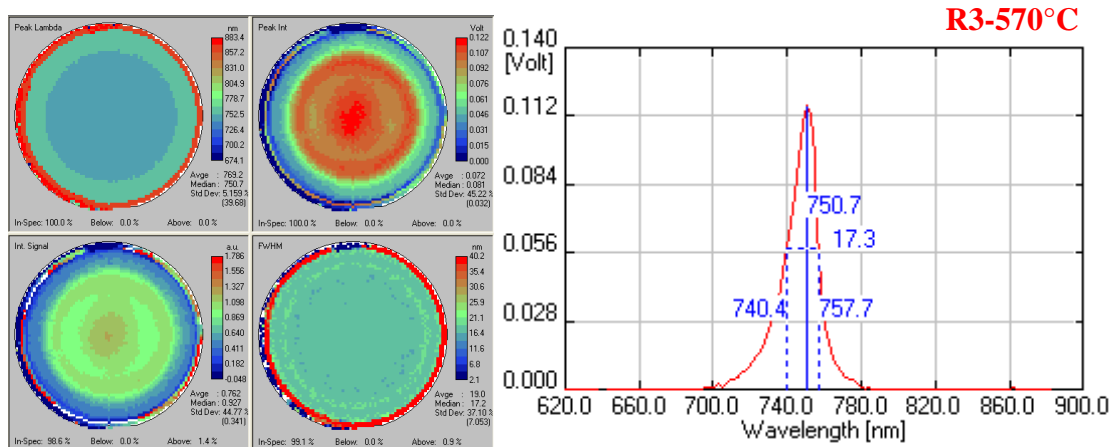
To examine the optical property, photoluminescence (PL) mapping was conducted immediately after MBE sample growth using a Nanometrics RPM2000 machine with an excitation wavelength of 635 nm. Post device-fabrication, current density-voltage ( $J$ - $V$ ) characteristics were measured by a calibrated solar simulator with a xenon lamp under one sun (AM 1.5G) illumination at room temperature. Data was collected by a sourcemeter and processed using a software to plot the  $J$ - $V$  graph. External quantum efficiency (EQE) measurements were carried out using the light beam from a halogen lamp, which are passed into a monochromator. The monochromatic beams were calibrated with a GaAs photodiode and the data was analysed using a software to plot the EQE spectrum.

## 6.3 Results and discussion

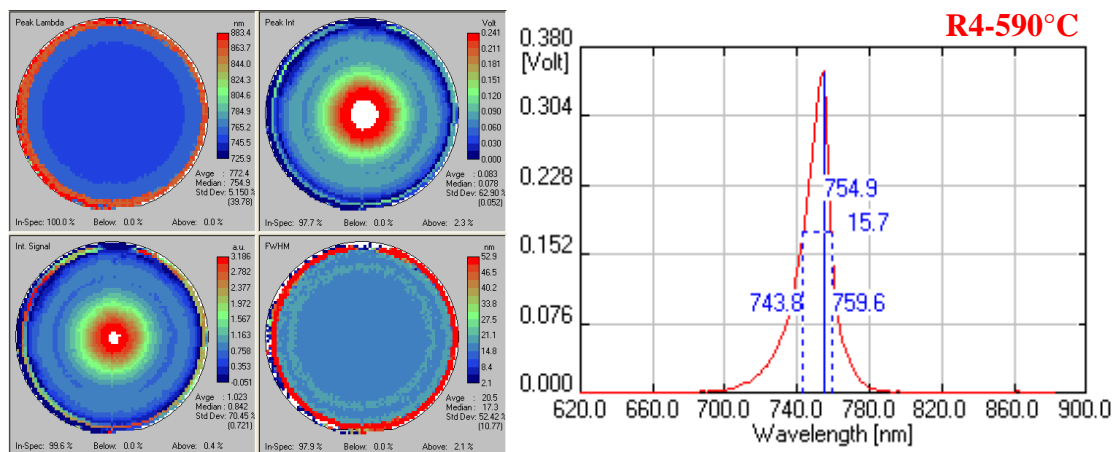
### 6.3.1 PL mapping



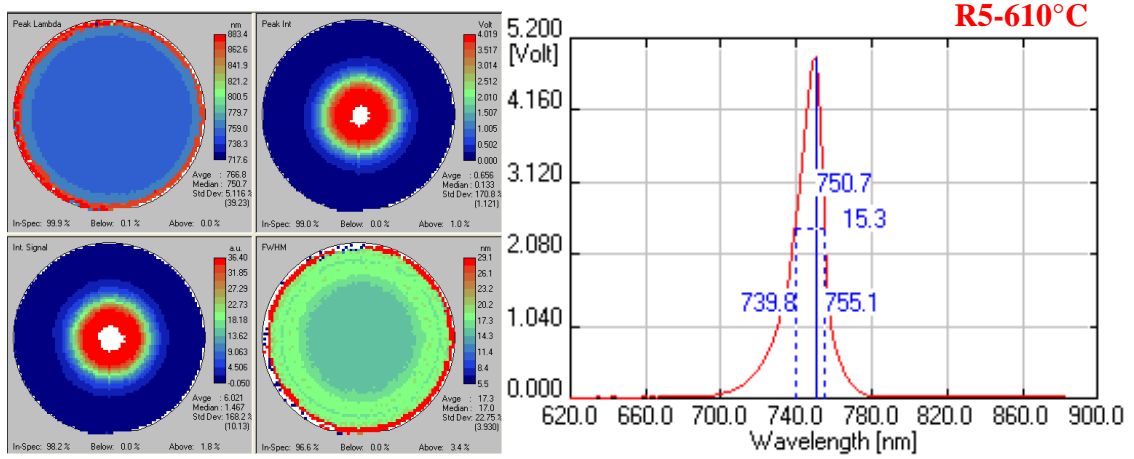
(a)



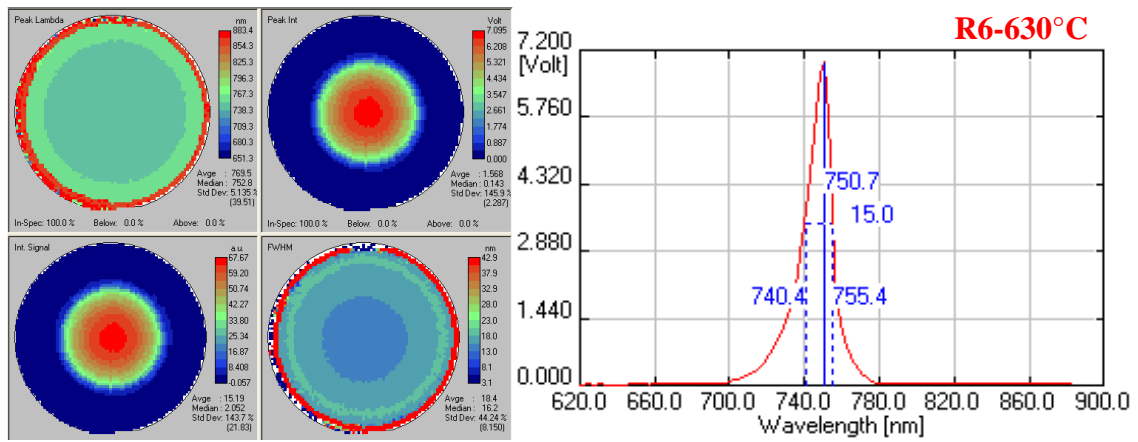
(b)



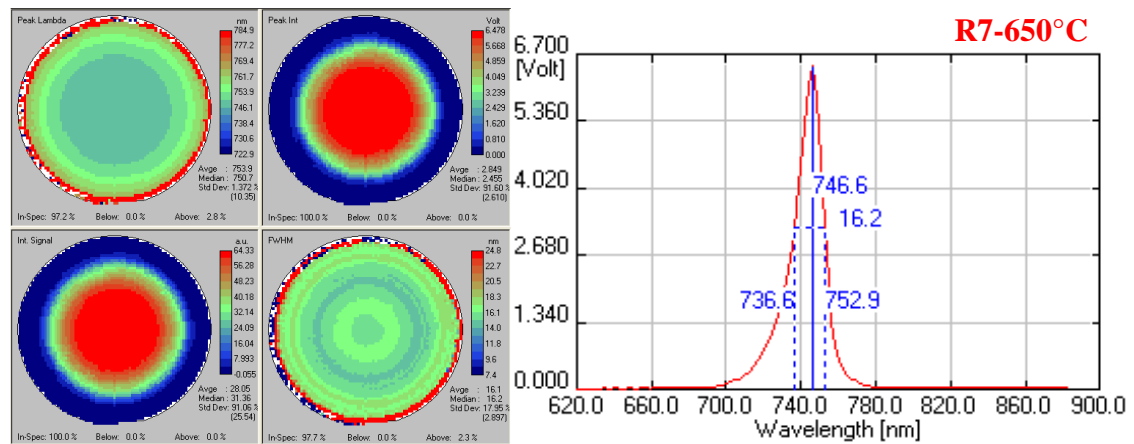
(c)



(d)



(e)



(f)

Figure 6.2 PL mapping of AlGaAs samples

Figure 6.2 presents the PL mapping of all samples (R2 to R7) with their respective growth temperature (550 °C to 650 °C). The left-hand-side figures illustrate four heat maps of sample's peak wavelength, peak intensity, signal intensity and full width at half maximum (FWHM). The right-hand-side figures depicts the PL plot at the centre of the sample where the material quality is at its optimum.

The peak wavelength heat maps indicate that all samples have a wavelength of 750 nm bandgap corresponding to a bandgap of 1.65 eV, which is 0.05 eV lower than our expected value. Hence, the Al composition is slightly less than 22%. The FWHM heat maps show the linewidth of the peak, and a low FWHM reflected as a sharp peak on the PL plot demonstrates the high purity of material.

The peak and signal intensity heat maps illustrate which region of the wafer emits the highest amount of photons—the uniformity and quality of material. Samples R2, R3 and R4 grown at <600 °C have scarce amount of photon emission, implying that when converted into voltages, the outputs are less than 0.35 V. This poor quality of materials grown at below 600 °C can be ascribed to a high density of deep-level defects induced by oxygen contamination, which trap the carriers and thus prevent them from recombination and collection. Therefore, these samples (R2 – R4) were not fabricated into SC devices. On the other hand, samples (R5, R6 and R7) grown at over 600 °C have peak intensities higher than 5 V which is one magnitude higher than R2 – R4 samples. This result suggests that 600 °C is a minimum temperature required to minimise the oxygen contamination and deep level defects, as well as to obtain the reasonable material quality. The peak intensity of R6 sample grown at 630 °C was 7 V, but a further increase in growth temperature has resulted the decrease of peak intensity (lower voltage output of 6.5 V). From the peak intensity heat maps of R5 – R7 samples, R7 has a larger surface area (1.5”) of peak intensity compared to that of R5 and R6 (1”). A data extrapolating method suggests that further increasing the growth temperature can enhance the material quality at the centre of the wafer. Moreover, sample R7 has a peak wavelength of 746 nm which signifies an increase in bandgap towards 1.7 eV. This may be because the Al composition begins to overtake Ga at this growth condition.

### 6.3.2 EQE

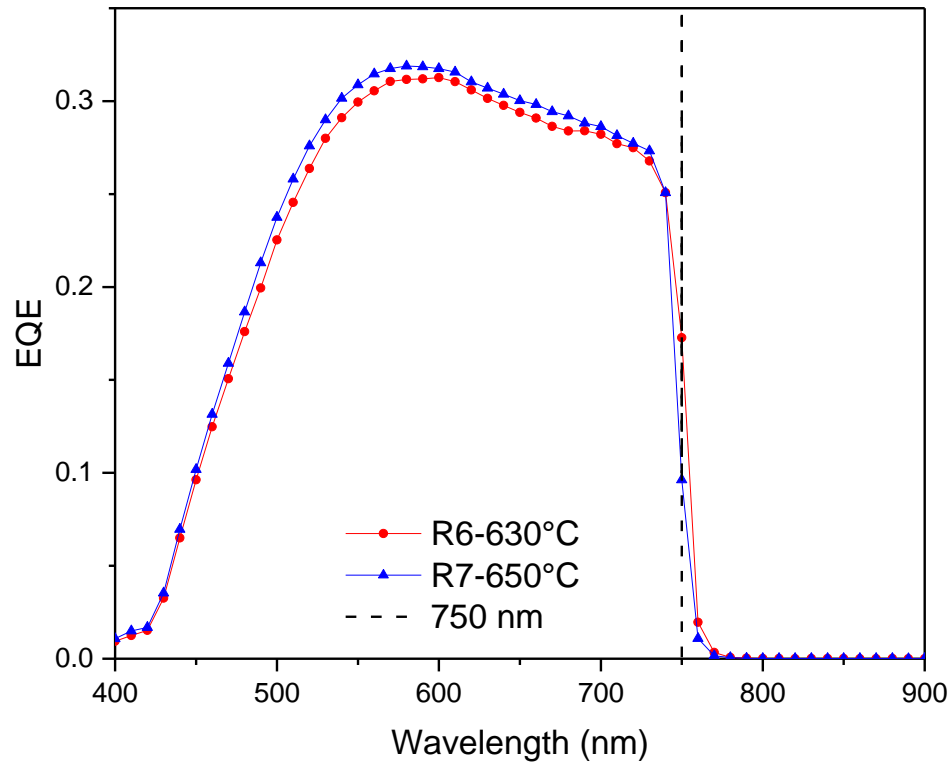


Figure 6.3 EQE spectrum of AlGaAs SCs

Figure 6.3 closely compares the EQE spectrum of sample R6 and R7, showing the absorption and extraction of the device at different wavelengths. Both samples experience a sharp EQE decline at the band edge of AlGaAs, 750 nm, denoted by the black dashed line. This is in agreement with the PL measurements showing that carrier recombination also occurs at the same wavelength. Moreover, sample R7 shows a slightly lower band edge than that of sample R6, indicating that R7 has a higher bandgap. This subtle difference further confirms the previous PL results from which the band edge wavelength of sample R7 and R6 was measured to be 746 nm and 750 nm, respectively. Sample R7 shows a higher EQE level than R6 between the intra-bandgap wavelengths (400 nm to 750 nm), suggesting that the current density is higher. The highest EQE level which occurred at 600 nm, followed by a diminishing trend, signifies high material quality at the active region followed by a deteriorating material quality towards the substrate. This implies that deep

level oxygen contamination is present, and this conclusion is further reflected by the low EQE value. The Al-O defects at the base region trap the carriers travelling through and, hence, prevent them from being extracted at the n-type metal contact. As a result, less current output is detected. Noticed that there is zero current contribution beyond the sub-bandgap due to no inclusion of QDs.

### 6.3.3 J-V

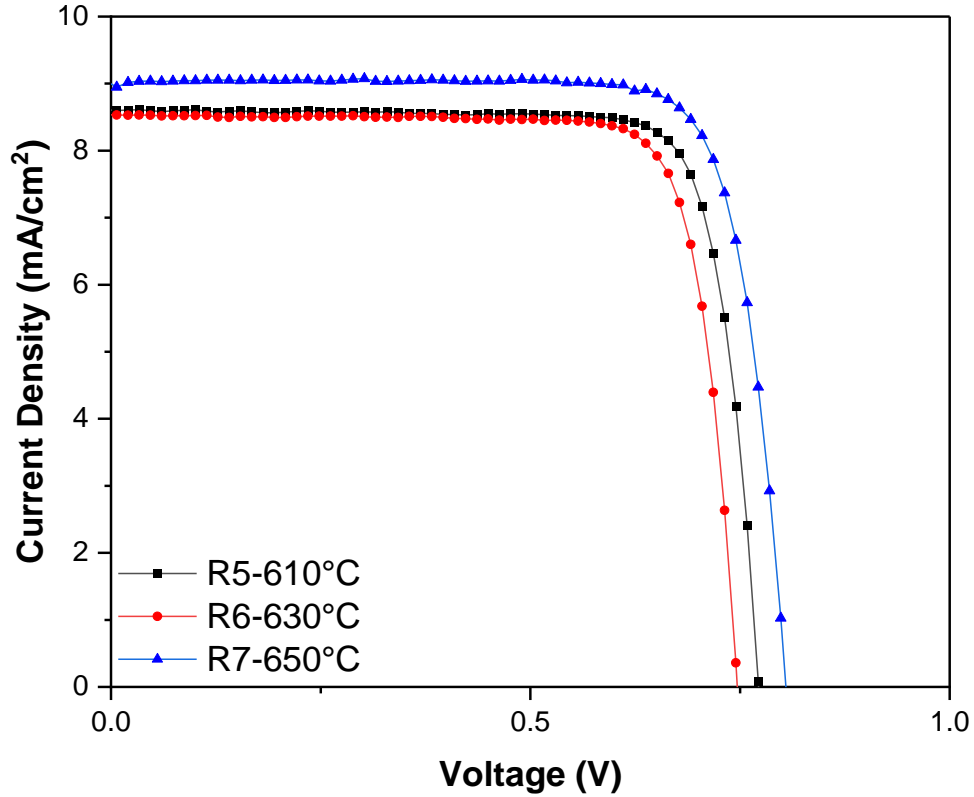


Figure 6.4 J-V graphs of AlGaAs SCs

Device	$J_{sc}$ (mA/cm <sup>2</sup> )	$V_{oc}$ (V)	FF (%)	$\eta$ (%)
R5-610°C	8.61	0.772	81.53	5.42
R6-630°C	8.53	0.747	81.24	5.18
R7-650°C	9.03	0.804	80.68	5.86

**Table 6.1 J-V characteristic parameters**

The  $JV$  graph and parameters of the fabricated devices are shown in Figure 6.4 and Table 5.1, respectively. Device R7 grown at the highest temperature (650 °C) achieved the best performance. It produced the most amount of current density and voltage output, thereby scoring the highest efficiency of 5.86%. On the contrary, device R5 and R6 obtained an  $\eta$  of 5.42 % and 5.18 %, respectively. Particularly, sample R6 of which the growth condition was expected to be an optimum achieved the lowest overall efficiency of 5.18 %. This finding indicates that the optimum growth condition estimated by the data extrapolation methods has not been reached. Therefore, a further investigation, namely an increase of growth temperature over 650 °C is required to find the optimised growth condition of Al composition (to 22%).

All devices have attained an average  $J_{sc}$  of 9 mA/cm<sup>2</sup> and  $V_{oc}$  of 0.8 V. Considering that Onno et al. have reported a highest  $J_{sc}$  of 7.85 mA/cm<sup>2</sup> with similar AlGaAs SC designs, the  $J_{sc}$  of 9 mA/cm<sup>2</sup> in this work is relatively high [16]. In terms of  $V_{oc}$ , however, an average of 0.8 V is below the expectation. The equation below states that the  $V_{oc}$  is dependent upon the carrier concentrations:

$$V_{oc} = \frac{kT}{q} \ln \left[ \frac{(N_A + \Delta n)\Delta n}{n_i^2} \right] \quad \text{Equation 6.1}$$

where  $kT/q$  is the thermal voltage,  $N_A$  is the doping density,  $\Delta n$  is the excess carrier concentration and  $n_i$  is the intrinsic carrier concentration.

According to this equation, a bandgap of 1.7 eV corresponds to a  $V_{oc}$  of 1.4 V. Onno et al. reported a highest  $V_{oc}$  of 1.212 V which is sufficiently high in practice. One of the causes for the voltage shortfall in our result can be explained from the equation 5.1. Namely, the deep level Al-O contaminants confine the carriers within the defective sites and, hence, reduce the number of excess carriers that have been photo-generated. Thus, the  $\Delta n$  of the equation is reduced, which leads to a lower  $V_{oc}$ . It is worth noting that although the PL measurement confirms the material bandgap is at the correct wavelength (750 nm), it does not assume the voltage output is in agreement when fabricated into SC devices. The impact

of carrier concentration loss is also an important factor to consider and it is dependent on the deep level defects within the material.

In addition, a mis-performance can result in a loss of  $V_{oc}$ , due to the complexity of top contacts fabrication. During the n-type metal contact lift-off process, dust particles from the metal deposit can attach to the mesa sidewalls if the process is not carried out thoroughly. The conductive metal particles provide alternative path for electrons to travel when metal contacts are connected. As a result, currents are leaked through and the voltages are shunt lower. As cited previously, the  $J_{sc}$  of samples R5, R6 and R7 are higher than the ones reported by Onno et al., but the  $V_{oc}$  are lower. Onno et al. fabricated the device with a different configuration—the n-type metal contacts deposited onto the backside of the substrate instead of the front side. Hence, the SC devices did not experience any shunting from mesa sidewalls. There are two methods to counter this problem, the first is to deposit an extra n-type metal contact onto the backside of the substrate so that the short-circuited top contacts are avoided from connection. However, this method is not recommended due to the extra cost of deposition material. The second approach is to perform another etching step i.e. immersing the devices into  $H_2SO_4:H_2O_2:H_2O$  (1:10:80) solution in order to clean the sidewalls. The issue with this approach is that the adhesion of the dust particles to the sidewalls are strong so that it is difficult to remove the particles and, thus, longer etching time is required to complete the process. However, the etching time should be controlled under 5 minutes otherwise the etched depth would reach the buffer or substrate layer.

## 6.4 Conclusion

The aim of the project is to implement the optimum bandgap configuration stated in the IBSC theory. The first approach is to find out the best growth condition for 1.7 eV AlGaAs material. Six samples with the same SC structure are grown at 550 °C, 570 °C, 590 °C, 610 °C, 630 °C, 650 °C and fabricated into SC devices. PL mapping data indicated that the minimum growth temperature to avoid Al-O contaminants is 610°C. Therefore, the samples grown at lower temperatures, showing poor material quality reflected by the radiative recombination rates, were omitted from fabrication. The results also suggested

that the optimal temperature is at 630 °C, but the assumption is dismissed post *JV* analysis. EQE spectra closely compared sample R6 and R7 to emphasise the subtle bandgap difference, providing a strong support for the PL results that at 650 °C, Al-composition increases and leads to a higher bandgap. Moreover, deep-level oxygen contamination was revealed by the deteriorating trend of EQE. The *JV* characteristics showed that sample R7 achieved the highest efficiency (5.86%); denying the assumption drawn from previous PL data that 630 °C is the optimal growth temperature. On the contrary, the statistics suggest that the optimum temperature is beyond 650 °C. Furthermore, an issue of low  $V_{oc}$  has been identified and the cause of the shortfall can be ascribed to deep level contamination and malpractice in lift-off. Methods to avoid the issue has been discussed for future guidance.

## 6.5 References

- [1] A. Luque and A. Martí, “Increasing the Efficiency of Ideal Solar Cells by Photon Induced Transitions at Intermediate Levels,” *Phys. Rev. Lett.*, vol.78, no.26, pp. 5014-5017, Jun. 1997.
- [2] A. Marti, L. Cuadra, and A. Luque, “Quantum dot intermediate band solar cell,” *Conf. Rec. IEEE Photovolt. Spec. Conf.*, Anchorage AK USA, vol. 2000-Jan, pp. 940–943, 2000.
- [3] A. Martí, N. Lopez, E. Antolin, E. Canovas, C. Stanley, C. Farmer, L. Cuadra, and A. Luque, “Novel semiconductor solar cell structures: The quantum dot intermediate band solar cell,” *Thin Solid Films*, vol. 511–512, pp. 638–644, 2006.
- [4] A. Martí, L. Cuadra, and A. Luque, “Design constraints of the quantum-dot intermediate band solar cell,” *Phys. E Low-Dimensional Syst. Nanostructures*, vol. 14, no. 1–2, pp. 150–157, 2002.
- [5] W. Shockley and H. J. Queisser, “Detailed balance limit of efficiency of p-n junction solar cells,” *J. Appl. Phys.*, vol. 32, no. 3, pp. 510–519, Mar. 1961.
- [6] T. Nozawa, H. Takagi, K. Watanabe, and Y. Arakawa, “Direct Observation of Two-Step Photon Absorption in an InAs/GaAs Single Quantum Dot for the Operation of Intermediate-Band Solar Cells,” *Nano Lett.*, vol. 15, no. 7, pp. 4483–4487, 2015.
- [7] E. Antolín, A. Marti, C. Farmer, P. Linares, E. Hernandez, A. Sanchez, T. Ben, S. Molina, C. Stanley, and A. Luque, “Reducing carrier escape in the InAs/GaAs quantum dot intermediate band solar cell,” *J. Appl. Phys.*, vol. 108, no. 6, p. 064513, Sep. 2010.
- [8] A. Luque, A. Marti, E. Antolin, and P. Garcia-Linares, “Intraband absorption for normal illumination in quantum dot intermediate band solar cells,” *Sol. Energy Mater. Sol. Cells*, vol. 94, no. 12, pp. 2032–2035, 2010.

- [9] A. Martí, E. Antonlin, C. Stanley, C. Farmer, N. Lopez, P. Diaz, E. Canovas, P. Linares, A. Luque, “Production of photocurrent due to intermediate-to-conduction-band transitions: A demonstration of a key operating principle of the intermediate-band solar cell,” *Phys. Rev. Lett.*, vol. 97, no. 24, pp. 1–4, 2006.
- [10] F. K. Tutu, P. Lam, J. Wu, N. Miyashita, Y. Okada, K. Lee, N. Ekins-Daukes, J. Wilson, and H. Liu, “InAs/GaAs quantum dot solar cell with an AlAs cap layer,” *Appl. Phys. Lett.*, vol. 102, no. 16, p. 163907, 2013.
- [11] P. Lam, S. Hatch, J. Wu, M. Tang, V. Dorogan, Y. Mazur, G. Salamo, I. Ramiro, A. Seeds, and H. Liu, “Voltage recovery in charged InAs/GaAs quantum dot solar cells,” *Nano Energy*, vol. 6, pp. 159–166, 2014.
- [12] Í. Ramiro, J. Villa, P. Lam, S. Hatch, J. Wu, E. Lopez, E. Antolin, H. Liu, and A. Luque, “Wide-Bandgap InAs/InGaP Quantum-Dot Intermediate Band Solar Cells,” *IEEE J. Photovoltaics*, vol. 5, no. 3, pp. 840–845, May 2015.
- [13] I. Ramiro, E. Antolin, M. Steer, P. Linares, E. Hernandez, I. Artacho, E. Lopez, T. Ben, J. Ripalda, S. Molina, F. Briones, C. Stanley, A. Marti, and A. Luque, “InAs/AlGaAs quantum dot intermediate band solar cells with enlarged sub-bandgaps,” in *Conference Record of the IEEE Photovoltaic Specialists Conference*, Austin TX USA, 2012, pp. 652–656.
- [14] T. Noda, T. Mano, M. Elborg, K. Mitsuishi, and K. Sakoda, “Fabrication of a GaAs/AlGaAs lattice-matched quantum dot solar cell,” *J. Nonlinear Opt. Phys. Mater.*, vol. 19, no. 4, pp. 681–686, 2010.
- [15] A. Onno, M. Tang, L. Oberbeck, J. Wu, and H. Liu, “Impact of the growth temperature on the performance of 1.70-eV  $\text{Al}_{0.22}\text{Ga}_{0.78}\text{As}$  solar cells grown by MBE,” *J. Cryst. Growth*, vol. 475, pp. 322–327, 2017.
- [16] A. Onno, M. Tang, M. Wang, Y. Maidaniuk, M. Benamara, Y. Mazur, G. Salamo, L. Oberbeck, J. Wu, and H. Liu, “MBE growth of 1.7eV  $\text{Al}_{0.2}\text{Ga}_{0.8}\text{As}$  and 1.42 eV GaAs solar cells on Si using dislocations filters: an alternative pathway toward III-

V/ Si solar cells architectures,” in *2017 IEEE 44th Photovoltaic Specialist Conference (PVSC)*, Washington DC USA, 2017, pp. 3370–3375.

## Chapter 7 Conclusion and future work

*This chapter summarises the findings of our research on quantum dot intermediate band solar cells (QD-IBSC). Moreover, the ongoing work presents novel discovery of QDSCs for space applications. In terms of future work, research directions are suggested with feasible design structures.*

## 7.1 Conclusion

The purpose of our research in quantum dot solar cells (QDSCs) is to realise the intermediate band solar cell (IBSC) [1]. The IBSC concept was proposed in 1997 with a theoretical maximum efficiency of 63.2 % [2]. The ideology behind the IBSC is to utilise the sub-bandgap photons which the Shockley and Queisser model has disregarded. It can be achieved by introducing an intermediate energy level within the bandgap which behaves as a stepping-stone to allow electrons with slightly insufficient energy to be excited into the conduction band [3]. As the QDs with nano-scale physical size exhibit discrete energy levels, they can be employed as IB material. However, for practical implementations, many challenges need to be addressed: thermal carrier escape, partial filling, high QD (layer or dot) density.

First investigation studies the possibility of background doping. The benefits of doping include partial filling of the IB and suppression of thermal carrier escape [4], [5]. The method is to locate the QD array from the intrinsic region to the base region where Si dopants are pre-existent. The outcome has shown improvements in voltage output (27 % marginal increase) and efficiency (22% marginal increase). Thus, we assume that the optimal position of QD array is outside the intrinsic region.

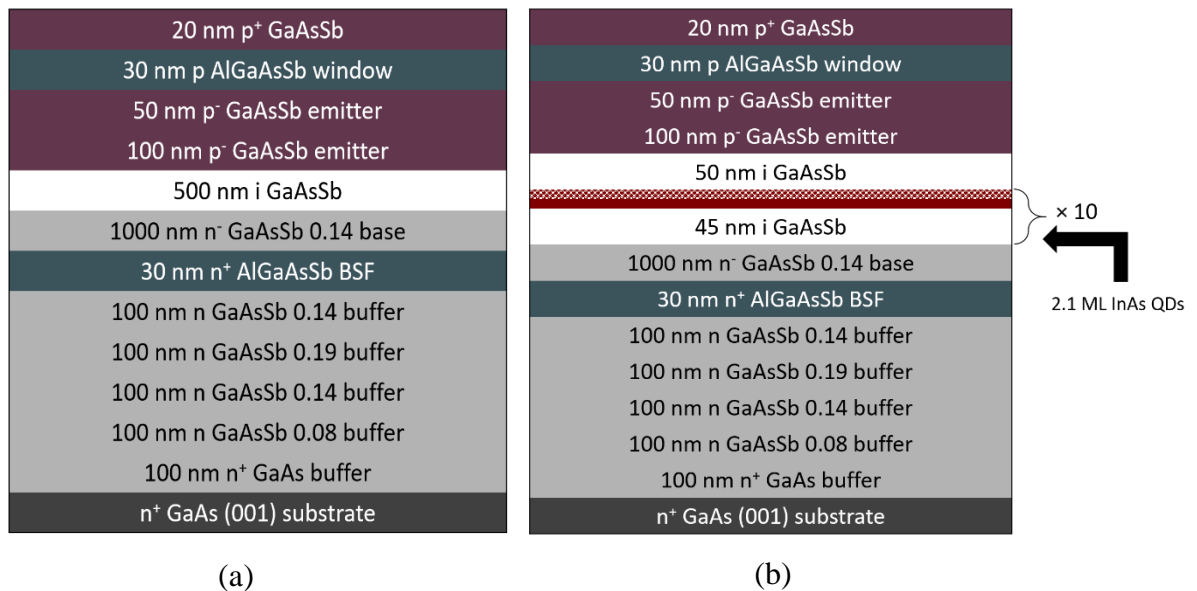
Second project investigates the cause of current loss post Si-doping. Si-doped QDs had a beneficial impact on voltage enhancement, but it came at a cost of current reduction. The origin of the current loss is ascribed to the reduction in depletion width and effective absorption area [5]. In order to recover the lost current, i.e. extend the depletion width, the thickness of the intrinsic region is increased by 100 nm. The results have shown a current output increase by 14% without any voltage loss. The capacitance-voltage measurements confirm that an insertion of additional 100 nm intrinsic layer increased the depletion width, while the Si-doping decreased the width. This finding also suggests that the addition intrinsic layer thickness should be further increased to 300 nm in order to fully recover the current loss caused by Si doping.

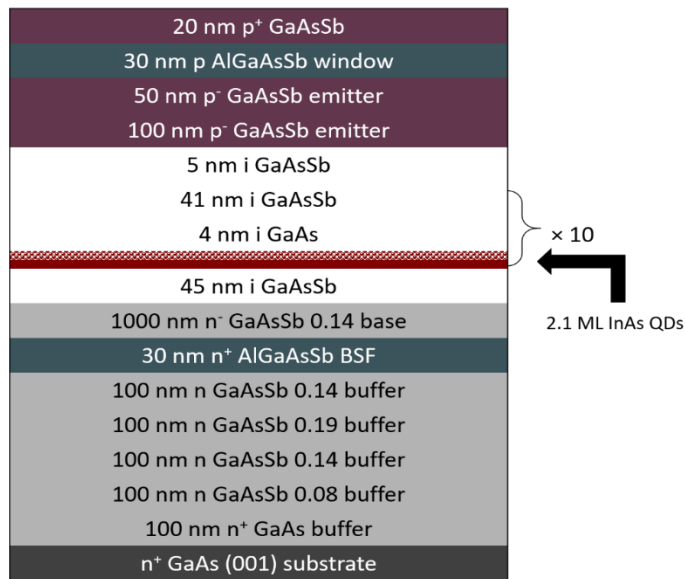
Third project aims to achieve the optimum bandgap configuration (1.95 eV VB—CB, 1.24 eV VB—IB and 0.71 eV IB—CB) so that maximum theoretical efficiency can be reached [6]. The use of AlGaAs material has a potential to provide the host material with the bandgap tunability between 1.42 eV to 2.16 eV. Moreover, a wider bandgap material has a thermal carrier escape suppression effect [7]. The growth condition of  $\text{Al}_{0.22}\text{Ga}_{0.78}\text{As}$  material is optimised by growing samples at six different temperatures. The results have shown a material improvement at growth temperature above 600°C, and further increasing the temperature leads to a greater increase in Al-composition. Therefore, we recommend higher growth temperature for higher Al-composition materials.

## 7.2 Ongoing work

Recent studies have shown that the QDSCs not only has the potential to implement the IBSC, but also have promising applications for space solar cells [8]. Under space environment, cosmic radiation is not sheltered by earth atmosphere; hence, bulk material SC would become defective due to the particle bombardment [9]. The QDs, on the other hand, are more immune to radiation i.e. “radiation hard” owing to its small physical size. Therefore, the QDSCs are regarded as a promising candidate for space operation of SCs. Moreover, the wavelength of InAs QDs at 1000 nm functions better under low intensity low temperature (LILT) environment such as on Mars, Jupiter and Saturn.

Our ongoing study investigates the feasibility of space QDSCs. Three GaAsSb based SCs were grown: without QDs, with InAs QDs, and with InAs QDs and thicker GaAs interlayer, as shown in Figure 7.1. The inclusion of Sb material can increase the QD density by reducing the size of the QDs, and, hence, GaAsSb QDs have a smaller physical size than GaAs QDs [10]. As a result, we anticipate that the GaAsSb QDSCs have stronger radiation immunities. In addition, the GaAsSb QDSC with thicker GaAs interlayer (Figure 7.1(c)) can enhance photon absorption, increasing the current output of the SC.

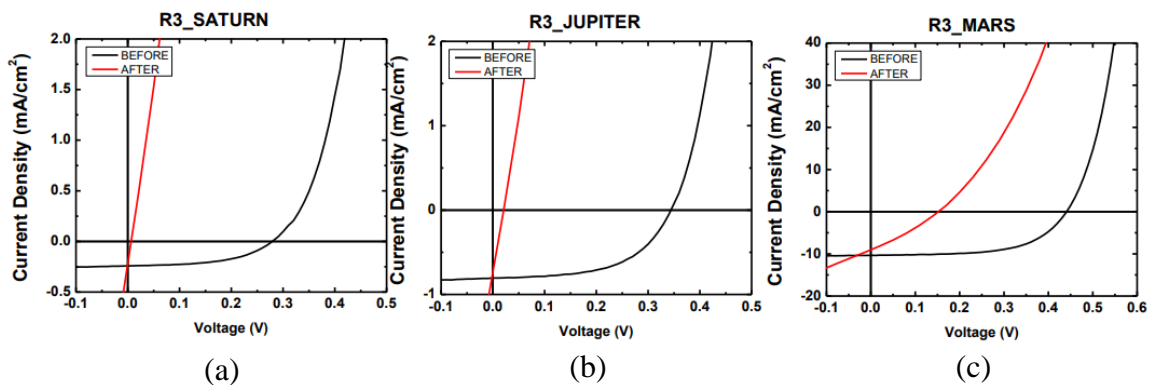




(c)

Figure 7.1 Schematics of the GaAsSb SCs

To examine the device performance under space conditions. The *JV* characterisations were measured under LILT environment: Saturn (100K, 0.01 suns), Jupiter (135 K, 0.037 suns) and Mars (263K, 0.43 suns). To mimic the exposure condition under particle bombardment, each device is then exposed to 1 MeV electron irradiation at a fluence of  $1 \times 10^{15}$  electron/cm<sup>2</sup>. The device performance is re-measured post-irradiation to evaluate the effect of particle bombardment.



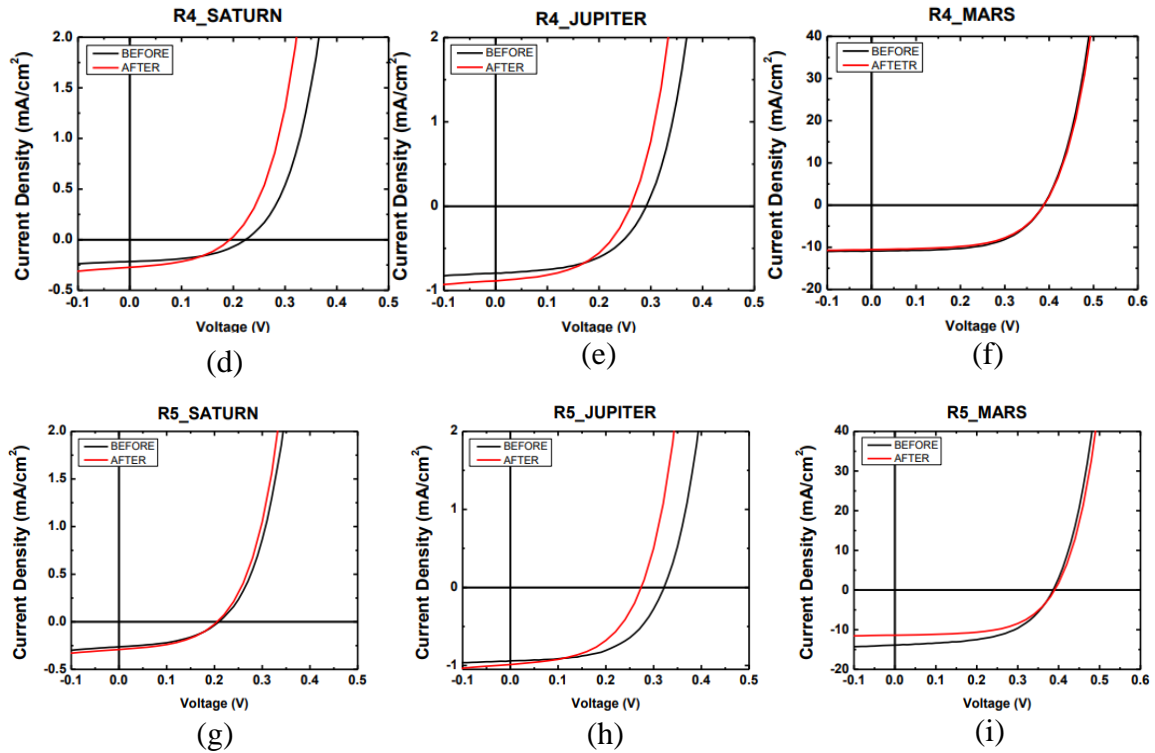


Figure 7.2 JV graphs of GaAsSb SCs before and after irradiation: (a)-(c) with no QDs, (d)-(f) with QDs and (g)-(i) QDs with GaAs interlayers

Figure 7.2 illustrates the *JV* curves of the GaAsSb samples under LILT condition before and after the 1 MeV electron irradiation. Figure 7.2 (a), (b) and (c) show the device performance of the GaAsSb sample without QDs (R3); (d), (e) and (f) show the GaAsSb QDSC (R4); (g), (h) and (i) show GaAsSb QDSC with GaAs interlayers (R5). It can be observed by vertical comparison that R3 device has scored the highest voltage output before irradiation. However, after the irradiation, the voltage output of the device has degraded to such extent that the device is considered mal-functioning. On the other side, the QDSCs (R4 and R5) have maintained their performances and achieved unexpectedly better current output under Saturn and Jupiter environment after irradiation. The QDSCs with GaAs interlayer (R5) has obtained higher current output compared to the R4 due to its additional intrinsic layer. However, under Mars environment, current output of R5 is lower after irradiation. This result suggest that the interlayer is also under the threat of particle bombardment.

In summary, we report that the QDSCs are more suitable than conventional bulk SCs for space applications. The InAs/GaAsSb QDSCs have demonstrated strong radiation immunity compared to a GaAsSb SC without QDs. The voltage degradation was observed in conventional GaAsSb SC after irradiation whereas an improvement in current density was detected in GaAsSb QDSC after irradiation. Moreover, the results from InAs/GaAsSb QDSC with GaAs interlayer sample signifies potential current deterioration caused by the particle bombardment in the GaAs layer. For future space SCs, QD based SCs are recommended over the bulk material SCs.

### 7.3 Future work

The QDSC research has reached a bottleneck in terms of implementing the IBSC. Although the theoretical proofs of IBSC mechanics e.g. partial filling, two-step photon absorption, high QD density have been demonstrated individually in QDSCs, the collective outcome has been unsatisfactory [11]–[13]. The core reason arises from the characteristics of Stranski-Krastanov (SK) growth which produce a dot-in-a well (DWELL) structure instead of a spherical QD [14]. A quantum well structured wetting layer (WL) is formed below the QDs and causes carriers to be excited through the continuous energy levels [15]. Moreover, the as-grown QDs have a hemispherical shape rather than the ideal spherical shape which also has an impact on the electron confinement [16]. A novel growth mode needs to be developed in order to form the QDs without WLs. Submonolayer (SML) QD growth is an alternative approach to the SK growth mode, it forms the QDs by depositing strained InAs within a single monolayer thickness [17]. Although the structure of the QDs has a square-like shape, it has similar electron confining properties akin to the QDs due to its thin thickness. Most importantly, no WL is formed under SML QD growth.

In recent years, QDSC research have shifted focus from IBSC implementation towards space applications which is potentially a more promising field for QDs. The well-established QD material—InAs, has bandgap tunability between the infra-red spectrum which is suitable on Mars where sunlight intensity is 0.43 suns. Furthermore, the temperature in space is lower than Earth, hence, the effect of thermal carrier escape is suppressed in QDSCs. Based on the ongoing investigation, QDSCs in attempt to implementing space SCs should focus on reducing the physical size of the QDs so that particle bombardment is less likely to damage the material quality. However, reducing the QD size increases the bandgap of the material which lead to a reduction in photon absorption and current output. Nevertheless, QDSCs have a great future in space solar cells. The focus of space QDSC is to find the suitable QD size or material for the suitable space/planet solar spectrum.

Finally, the author would like to propose an ambitious ideology which, he believes, has not been considered or realised in the past research. Previous studies have attempted to dope

the QDs with n-type dopant and p-type dopant *separately*, but never *simultaneously*. For example, SC structures with alternating dopant QD layers or alternating QDs as shown in Figure 7.3 (ranked by the level of intermixing).

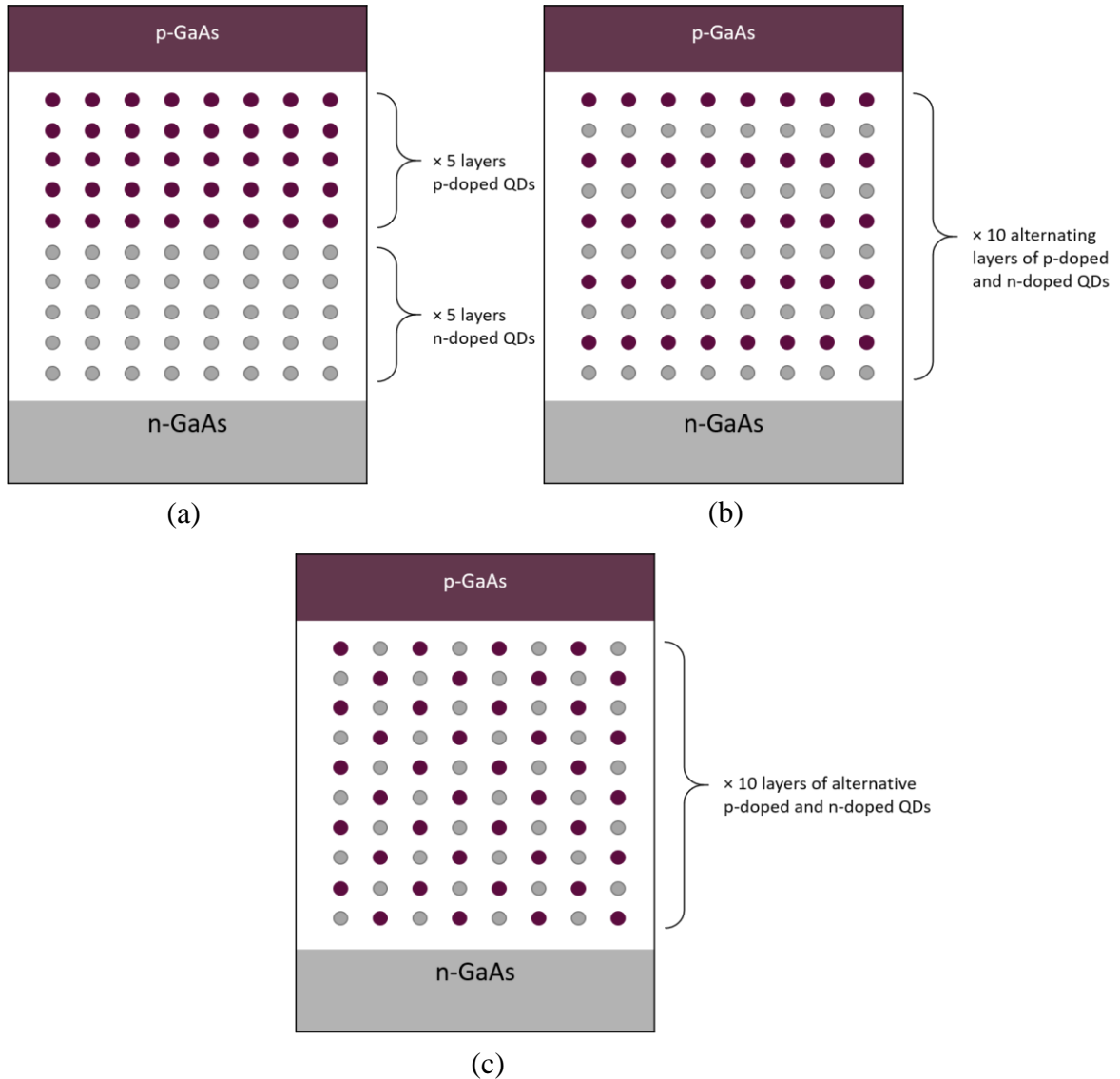


Figure 7.3 QDSD structures with (a)&(b) alternating QD layers and (c) alternating QDs

The effects of doping QDs with both dopants are undiscovered, however, there are some theoretical foundations that can support this suggestion. Doping QDs with n-type dopants reduces the current output by shortening the depletion width. One of the methods to mitigate this negative impact is to insert additional layers of intrinsic material as

demonstrated in previous chapter. Another method is to insert p-type dopant to the QDs that may neutralise the charge of the n-type dopant, and, thus, negate the current loss effect.

Growing nano-structured particles like QDs is already a task that require high-precision epitaxial growth skill, introducing dopants to the QDs demands even higher growth skill, needless to inform the difficulty of introducing two-types of different dopants. Since the success rate of finding valuable outcome before the material quality is hindered by dopant induced defects is low, three structures are proposed here. Figure 7.3 (a) has 5 layers of p-doped QDs followed by 5 layers of n-doped QDs which should be the most feasible design to implement. Figure 7.3 (c) is a courageous attempt that envisions a pn-junction QD structure which may potentially show the most prominent neutralising effect.

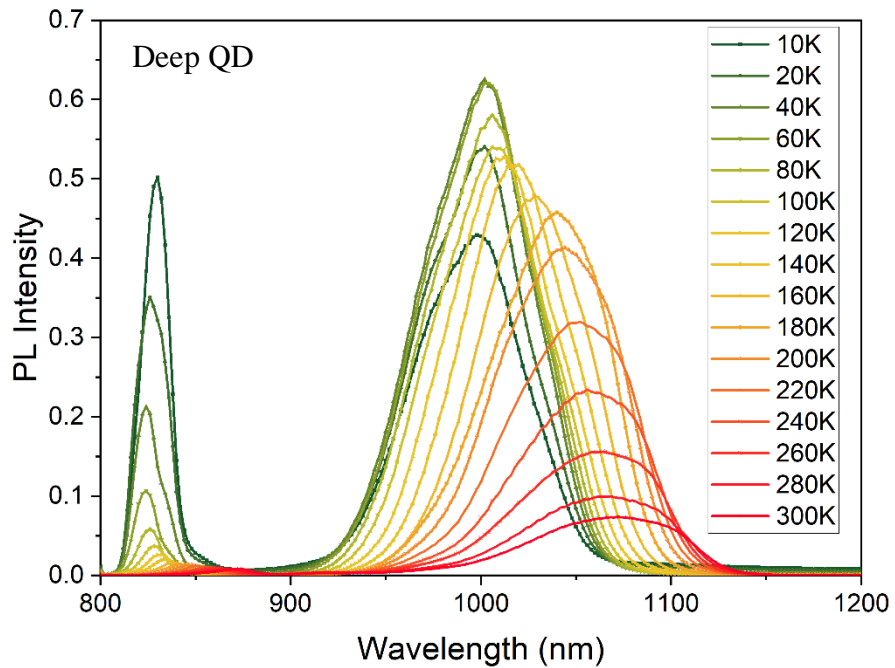
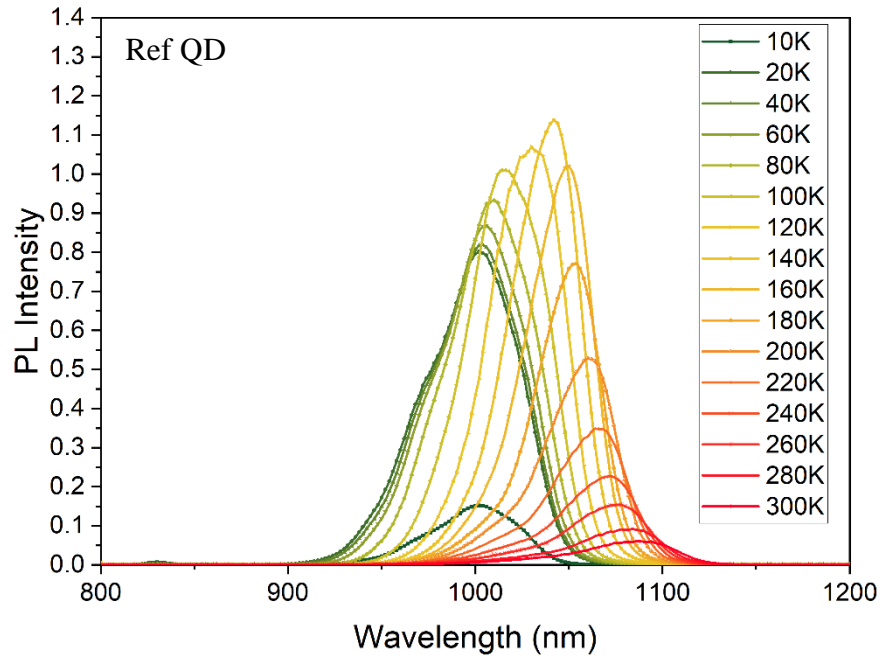
## 7.4 References

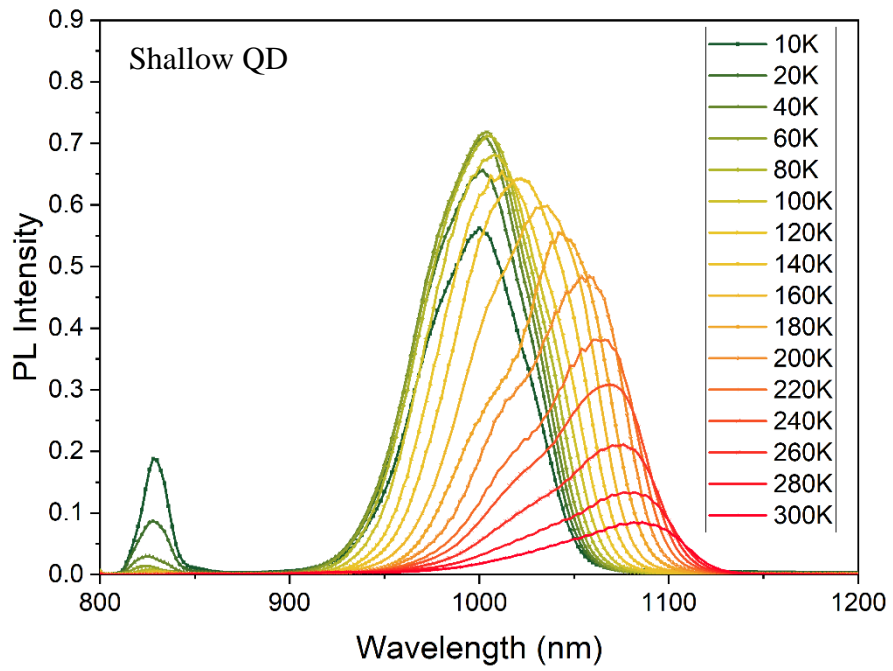
- [1] A. Martí, L. Cuadra, and A. Luque, “Quantum dot intermediate band solar cell,” *Conf. Rec. IEEE Photovolt. Spec. Conf.*, Anchorage AK USA, vol. 2000-Jan, pp. 940–943, 2000.
- [2] A. Luque and A. Martí, “Increasing the Efficiency of Ideal Solar Cells by Photon Induced Transitions at Intermediate Levels,” *Phys. Rev. Lett.*, vol. 78, no. 26, pp. 5014–5017, Jun. 1997.
- [3] A. Luque, A. Martí, and C. Stanley, “Understanding intermediate-band solar cells,” *Nat. Photonics*, vol. 6, no. 3, pp. 146–152, 2012.
- [4] P. Lam, S. Hatch, J. Wu, M. Tang, V. Dorogan, Y. Mazur, G. Salamo, I. Ramiro, A. Seeds, and H. Liu, “Voltage recovery in charged InAs/GaAs quantum dot solar cells,” *Nano Energy*, vol. 6, pp. 159–166, 2014.
- [5] D. Kim, M. Tang, J. Wu, S. Hatch, Y. Maidaniuk, V. Dorogan, Y. Mazur, G. Salamo, and H. Liu, “Si-Doped InAs/GaAs Quantum-Dot Solar Cell with AlAs Cap Layers,” *IEEE J. Photovoltaics*, vol. 6, no. 4, pp. 906–911, 2016.
- [6] A. Martí, L. Cuadra, and A. Luque, “Design constraints of the quantum-dot intermediate band solar cell,” *Phys. E Low-Dimensional Syst. Nanostructures*, vol. 14, no. 1–2, pp. 150–157, 2002.
- [7] Í. Ramiro, J. Villa, P. Lam, S. Hatch, J. Wu, E. Lopez, E. Antolin, H. Liu, and A. Luque, “Wide-Bandgap InAs/InGaP Quantum-Dot Intermediate Band Solar Cells,” *IEEE J. Photovoltaics*, vol. 5, no. 3, pp. 840–845, May 2015.
- [8] S. M. Hubbard, “Nanostructured photovoltaics for space power,” *J. Nanophotonics*, vol. 3, no. 1, p. 031880, 2009.
- [9] C. D. Cress, S. M. Hubbard, B. J. Landi, R. P. Raffaele, and D. M. Wilt, “Quantum dot solar cell tolerance to alpha-particle irradiation,” *Appl. Phys. Lett.*, vol. 91, no. 18, pp. 10–13, 2007.

- [10] N. Faleev, K. Y. Ban, S. Bremner, D. J. Smith, and C. Honsberg, "Investigation of the main correlations between structural and physical properties of InAs quantum dots, embedded between strain-relief GaAsSb layers," *Conf. Rec. IEEE Photovolt. Spec. Conf.*, Seattle WA USA, pp. 000474–000479, 2011.
- [11] K. A. Sablon, J. W. Little, V. Mitin, A. Sergeev, N. Vagidov, and K. Reinhardt, "Strong enhancement of solar cell efficiency due to quantum dots with built-in charge," *Nano Lett.*, vol. 11, no. 6, pp. 2311–2317, 2011.
- [12] T. Nozawa, H. Takagi, K. Watanabe, and Y. Arakawa, "Direct Observation of Two-Step Photon Absorption in an InAs/GaAs Single Quantum Dot for the Operation of Intermediate-Band Solar Cells," *Nano Lett.*, vol. 15, no. 7, pp. 4483–4487, 2015.
- [13] T. Sugaya, O. Numakami, R. Oshima, S. Furue, H. Komaki, T. Amano, K. Matsubara, Y. Okano, and S. Niki, "Ultra-high stacks of InGaAs/GaAs quantum dots for high efficiency solar cells," *Energy Environ. Sci.*, vol. 5, no. 3, pp. 6233–6237, 2012.
- [14] A. Luque and A. Martí, "The intermediate band solar cell: Progress toward the realization of an attractive concept," *Adv. Mater.*, vol. 22, no. 2, pp. 160–174, Jan. 2010.
- [15] E. Antolín, A. Martí, C. Farmer, P. Linares, E. Hernandez, A. Sanchez, T. Ben, S. Molina, C. Stanley, and A. Luque, "Reducing carrier escape in the InAs/GaAs quantum dot intermediate band solar cell," *J. Appl. Phys.*, vol. 108, no. 6, p. 064513, Sep. 2010.
- [16] A. Martí, N. Lopez, E. Antolin, E. Canovas, C. Stanley, C. Farmer, L. Cuadra, and A. Luque, "Novel semiconductor solar cell structures: The quantum dot intermediate band solar cell," *Thin Solid Films*, vol. 511–512, pp. 638–644, 2006.
- [17] P. Lam, J. Wu, M. Tang, Q. Jiang, S. Hatch, R. Beanland, J. Wilson, R. Allison, and H. Liu, "Submonolayer InGaAs/GaAs quantum dot solar cells," *Sol. Energy*

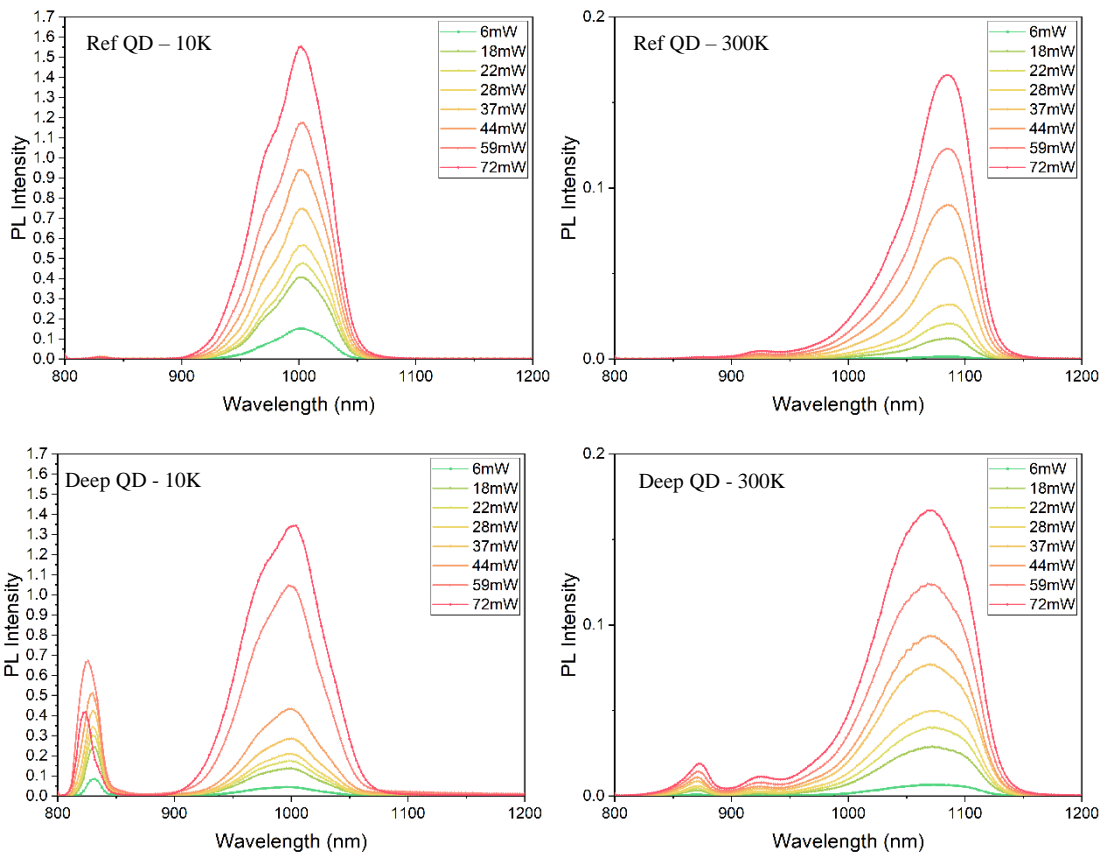
## Appendix

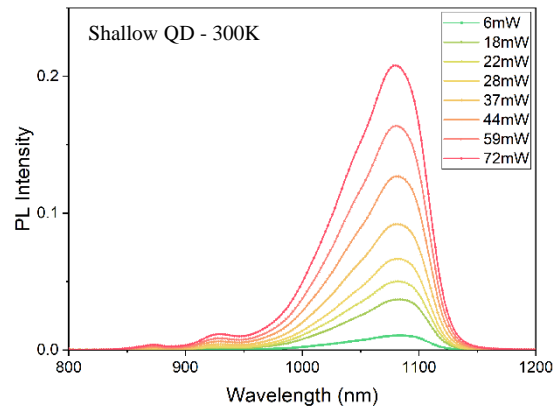
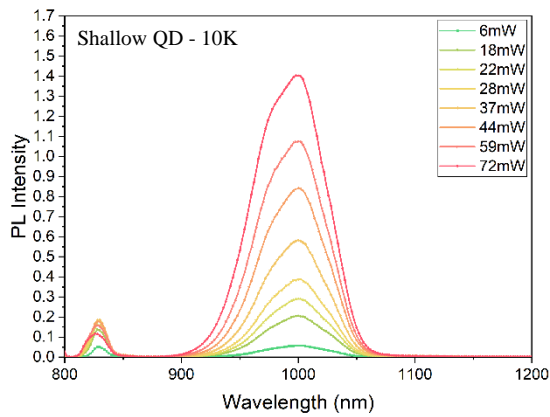
### UCL 305 Temperature-dependent photoluminescence



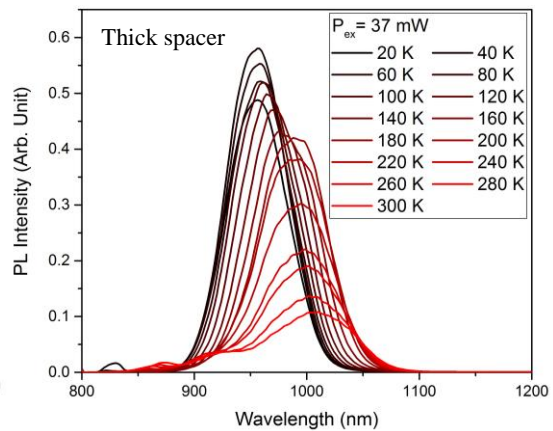
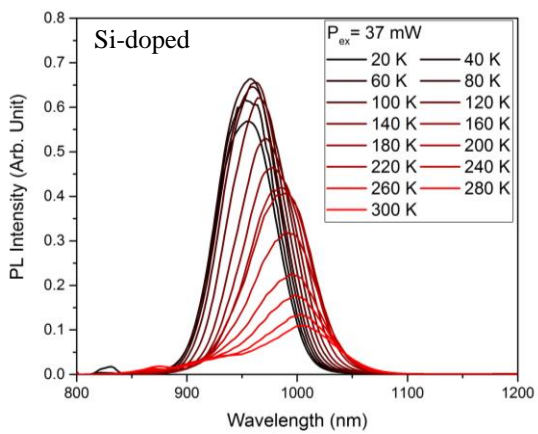
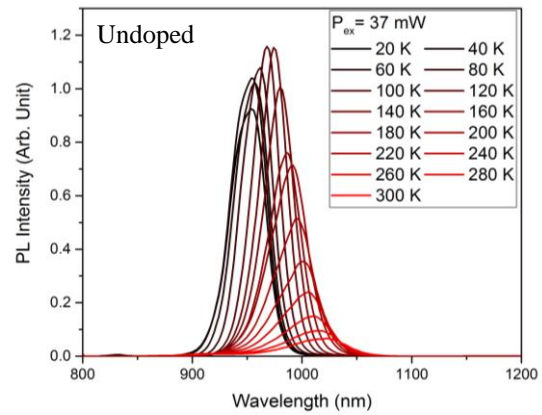
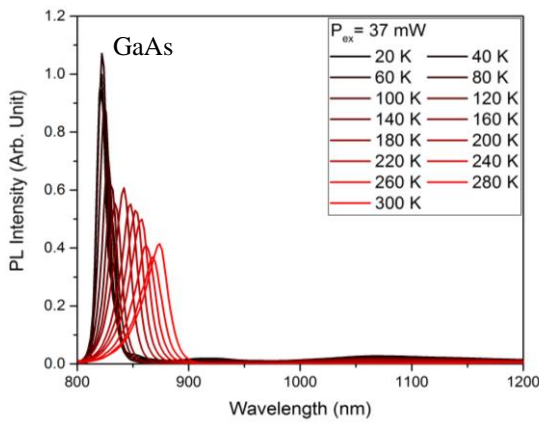


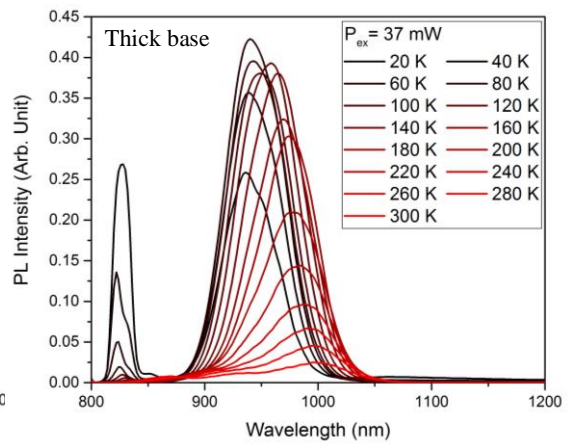
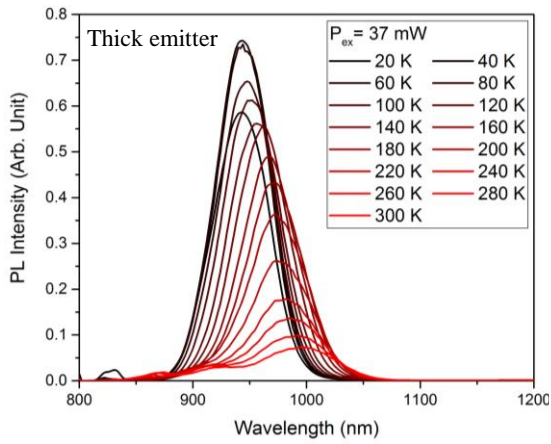
### UCL 305 Power-dependent photoluminescence





### UCL249 Temperature-dependent photoluminescence





### UCL249 Power-dependent photoluminescence

